AFRL-AFOSR-VA-TR-2022-0421

Numerical Investigation of Wake Effect for High-Lift Low-Pressure Turbine Blades

Gross, Andreas
New Mexico State University
1620 Standley Dr Academic RESH A RM 110
Las Cruces, NM,
US

07/25/2022
Final Technical Report

Air Force Research Laboratory
Air Force Office of Scientific Research
Arlington, Virginia 22203
Air Force Materiel Command

REPORT DOCUMENTATION PAGE

PLEASE DO NOT RETURN YOUR FORM TO THE ABOVE ORGANIZATION.

1. REPORT DATE	2. REPORT TYPE	3. DATES COVERED	
20220725	Final	START DATE 20190201	END DATE 20220731

4. TITLE AND SUBTITLE
Numerical Investigation of Wake Effect for High-Lift Low-Pressure Turbine Blades

5a. CONTRACT NUMBER	5b. GRANT NUMBER	5c. PROGRAM ELEMENT NUMBER
	FA9550-19-1-0080	61102F
5d. PROJECT NUMBER	**5e. TASK NUMBER**	**5f. WORK UNIT NUMBER**

6. AUTHOR(S)
Andreas Gross

7. PERFORMING ORGANIZATION NAME(S) AND ADDRESS(ES)
New Mexico State University
1620 Standley Dr Academic RESH A RM 110
Las Cruces, NM
US

8. PERFORMING ORGANIZATION REPORT NUMBER

9. SPONSORING/MONITORING AGENCY NAME(S) AND ADDRESS(ES)
Air Force Office of Scientific Research
875 N. Randolph St. Room 3112
Arlington, VA 22203

10. SPONSOR/MONITOR'S ACRONYM(S)
AFRL/AFOSR RTA1

11. SPONSOR/MONITOR'S REPORT NUMBER(S)
AFRL-AFOSR-VA-TR-2022-0421

12. DISTRIBUTION/AVAILABILITY STATEMENT
A Distribution Unlimited: PB Public Release

13. SUPPLEMENTARY NOTES

14. ABSTRACT
In low-pressure turbine linear cascade experiments, upstream stator vanes are often modeled by moving bar wake generators. The wake effect of a stator and a bar wake generator on the flow through a rotor with front-loaded high-lift blades were investigated and compared. Implicit large-eddy simulations were performed of the flow through a full turbine cascade with L2F airfoils (for both the stator vanes and rotor blades) as well as of the flow through a linear cascade with L2F blades and moving bar wake generator. The chord-based Reynolds number for the simulations was 50,000 and 100,000. The L2F generates pronounced endwall structures that clearly differentiate the resulting wake flow from that obtained with the barwake generator. Instantaneous flow visualizations reveal a periodic suppression of the rotor blade suction-side separation for both cases. For the bar wake generator, the wakes are wider and the wake effect is spread out over a larger portion of the wake shedding period. With upstream stator vanes, the rotor blade passage vortex and suction-side corner separation are suppressed. This suggests that for front-loaded high-lift airfoils, bar wake generators can accurately model the effect of the two-dimensional wake component. The stator near-wall structures appear to be chiefly responsible for the suppression of the passage vortex and corner separation. This effect is not captured by the bar wake generator

15. SUBJECT TERMS

16. SECURITY CLASSIFICATION OF:			17. LIMITATION OF ABSTRACT	18. NUMBER OF PAGES
a. REPORT	b. ABSTRACT	c. THIS PAGE		
U	U	U	UU	79

19a. NAME OF RESPONSIBLE PERSON	19b. PHONE NUMBER *(Include area code)*
GREGG ABATE	425-1779

From: Air Force Office of Scientific Research
To: Technical Reports
Subject: [URL Verdict: Neutral][Non-DoD Source] Deliverable Received: FA9550-19-1-0080
Date: Monday, July 4, 2022 11:25:02 AM

OMA Team,
A new Final Performance has been submitted for your attention. Award Number: FA9550-19-1-0080

Supporting Report: https://afosr.gov1.qualtrics.com/WRQualtricsSurveyEngine/File.php?F=F_2xVrUaJBaPinbG1

- Date Stamp: 11:22:34 , 7/4/2022
- Title: (HBCU) Numerical Investigation of Wake Effect for High-Lift Low-Pressure Turbine Blades
- DISTRIBUTION: Yes- Approved for Public Release (Distro A)
- Principal Investigator: Andreas Gross
  - PI Email: agross@nmsu.edu
- Program Officer: Gregg Abate
- Report Type: Final Performance
- Reporting Period
  - Start Date: 02/01/2019
  - End Date: 07/31/2022
- Award Number: FA9550-19-1-0080
- Report Due Date: 10/31/2022

ABSTRACT:
In low-pressure turbine linear cascade experiments, upstream stator vanes are often modeled by moving bar wake generators. The wake effect of a stator and a bar wake generator on the flow through a rotor with front-loaded high-lift blades were investigated and compared. Implicit large-eddy simulations were performed of the flow through a full turbine cascade with L2F airfoils (for both the stator vanes and rotor blades) as well as of the flow through a linear cascade with L2F blades and moving bar wake generator. The chord-based Reynolds number for the simulations was 50,000 and 100,000. The L2F generates pronounced endwall structures that clearly differentiate the resulting wake flow from that obtained with the bar-wake generator. Instantaneous flow visualizations reveal a periodic suppression of the rotor blade suction-side separation for both cases. For the bar wake generator, the wakes are wider and the wake effect is spread out over a larger portion of the wake shedding period. With upstream stator vanes, the rotor blade passage vortex and suction-side corner separation are suppressed. This suggests that for front-loaded high-lift airfoils, bar wake generators can accurately model the effect of the two-dimensional wake component. The stator near-wall structures appear to be chiefly responsible for the suppression of the passage vortex and corner separation. This effect is not captured by the bar wake generator.

Final Report

(HBCU) Numerical Investigation of Wake Effect for High-Lift Low-Pressure Turbine Blades

Air Force Office of Scientific Research
Grant number: FA9550-19-1-0080
Program manager: Dr. Gregg Abate

Andreas Gross
Mechanical and Aerospace Engineering Department
New Mexico State University

July 4, 2022

Abstract

In low-pressure turbine linear cascade experiments, upstream stator vanes are often modeled by moving bar wake generators. The wake effect of a stator and a bar wake generator on the flow through a rotor with front-loaded high-lift blades were investigated and compared. Implicit large-eddy simulations were performed of the flow through a full turbine cascade with L2F airfoils (for both the stator vanes and rotor blades) as well as of the flow through a linear cascade with L2F blades and moving bar wake generator. The chord-based Reynolds number for the simulations was 50,000 and 100,000. The L2F generates pronounced endwall structures that clearly differentiate the resulting wake flow from that obtained with the bar-wake generator. Instantaneous flow visualizations reveal a periodic suppression of the rotor blade suction-side separation for both cases. For the bar wake generator, the wakes are wider and the wake effect is spread out over a larger portion of the wake shedding period. With upstream stator vanes, the rotor blade passage vortex and suction-side corner separation are suppressed. This suggests that for front-loaded high-lift airfoils, bar wake generators can accurately model the effect of the two-dimensional wake component. The stator near-wall structures appear to be chiefly responsible for the suppression of the passage vortex and corner separation. This effect is not captured by the bar wake generator.

Contents

List of Figures

List of Tables

1 Introduction

In modern high-bypass jet engines, the fan produces up to 80% of the thrust. The fan is driven by the low-pressure turbine (LPT). Due to the high fan power requirements, the LPT is one of the larger engine components and it can contribute up to one third of the overall engine weight. This directs research at improving the overall efficiency of the LPT. Front-loaded high-lift blades, such as the L2F research blade developed by the Air Force Research Laboratory (AFRL) [1] at Wright-Patterson Air Force Base (WPAFB), promise improved loading but uncertainty remains with regard to the performance in real turbine environments. The anticipated higher loading of such profiles can reduce the overall blade count and thus reduce the LPT weight [2]. Marks et al. [3] and Lyall et al. [4] conducted experiments at low Reynolds numbers to investigate the losses due to laminar separation from the suction side of LPT blades. At Reynolds numbers below $300,000$, the losses attributed to laminar separation can be significant. For front-loaded airfoils such as the L2F, the adverse pressure gradient is deliberately reduced to ameliorate laminar separation from the suction side. However, such airfoils were found to suffer from increased endwall losses compared to mid or aft-loaded profiles [5, 6, 7].

Also in experiments at AFRL, Bear et al. [8] found that major endwall losses are attributed to both the suction-side corner separation and the passage vortex (PV). The turbulent endwall boundary layer impinges on the leading edge of the blade forming a horseshoe vortex (HV) [9] and the PV stems from the pressure-side leg. A secondary flow, which results from an imbalance of the centrifugal acceleration and pressure gradient near the endwall, "feeds" and strengthens the PV. The other leg of the HV, or the suction-side leg, is dissipated by the secondary flow. In turbulent junction flows, the HV exhibit a bimodal behavior that is characterized by a more or less random switching between a zero-flow state with weak HV and a back-flow state with strong HV that is located closer to the leading edge [10]. Wang et al. [11] performed smoke line visualizations for a linear turbine cascade at a Reynolds number of 10,000 that clearly revealed a bimodal behavior of the HV. A dimensionless frequency of $fC_{ax}/v_{in} = 0.6$ was reported, where C_{ax} is the axial chord and v_{in} is the inlet velocity. A correlation of the bimodal behavior with upstream turbulent boundary layer events was observed by Robison et al. [12] in large-eddy simulations (LES) of a canonical junction flow. Measurements by Veley et al. [13, 14] and Babcock et al. [15] as well as simulations by Gross et al. [16, 17] revealed an intermittent loss of coherence of the PV, that appeared related to the bimodal behavior. This suggests that the bimodal behavior of the HV has an impact on the overall efficiency of the LPT since the PV is a contributor to the total losses.

Langsten et al. [18, 19] and Sieverding [20] provided review papers on the endwall structures. Visualizations and descriptions of the full three-dimensional (3-D) flow field topology were provided by Sieverding [20], Goldstein and Spores [21], Sharma and Butler [22], Kang and Hirsch [23], and Wang et al.[11], among others. The effect of the endwall boundary layer thickness on the total pressure losses was investigated by Hodson and Dominy [24]. As the endwall boundary layer thickness increases, the PV moves farther away from the suction surface and the total pressure losses grow near the endwall but remain unchanged near mid-span.

As a result of the relative motion in turbine stages, the upstream stator wakes are periodically impinging on the downstream rotor blades. This raises the question how the endwall flow in tubine stages is affected by the passing wakes which, similar to active flow control approaches, can also be interpreted as unsteady disturbances. The wakes can roughly be characterized by a velocity deficit (negative jet) and turbulence. Experiments in rotating turbine facilities are complicated, expensive and difficult to instrument [25]. The generation of unsteady wakes in linear cascade wind tunnel experiments presents many challenges. Typically, two-dimensional (2-D) wakes without significant secondary flow are generated with moving bar wake generators. Experiments by Schulte and Hodson [26] and Kaszeta et al. [27] revealed bypass-transition of the suction-side boundary layer due to the passing wakes. Stieger and Hodson [28, 29] performed laser Doppler anemometry measurements in a linear cascade with passing wakes. The wakes can be regarded as a periodic freestream perturbation in the form of a momentum deficit or "negative jet". The suction surface flow accelerates upstream and decelerates downstream of the wakes. The deceleration destabilizes the flow and accelerates the roll-up of the separated boundary layer into spanwise vortices and transition of the suction-side boundary layer. Compared to the no-wake environment, the suction-side boundary layer is more resistant to separation and the losses due to laminar separation are reduced. Once a wake has passed, a region of attached "calmed" laminar flow is left behind. Depending on the wake passing frequency, the suction-side boundary layer may have enough time to separate before the next wake strikes. Flow visualizations by Stieger and Hodson showed that the wakes are accelerated and become Λ-shaped as they pass through the passage [28, 29]. Laminar separation was almost completely suppressed by the passing wakes in bar wake generator experiments by Nessler et al. [30, 31, 32] for a linear cascade with L1A blades at a Reynolds number of 25,000. The wakes reduced the total pressure losses by as much as 54%. Direct numerical simulations (DNS) and LES of a T106 cascade with periodic passing wakes by Wu and Durbin [33] and Michelassi et al. [34, 35] revealed that the wakes align with the principal axis of the main flow and that the resulting wake stretching generates streamwise vortices. Experiments by Volino [36] showed a complete suppression of laminar separation for high wake-passing frequencies and an intermittent suppression of flow separation for low wake-passing frequencies. Unsteady Reynolds-averaged Navier Stokes (URANS) calculations with k-ω and γ-Re$_\theta$ transition model of a linear cascade with T106 blades for an exit Reynolds number of $200,000$ and for different flow coefficients and wake-passing frequencies indicated that the wakes cause a periodic reduction of the strength of the PV and trailing-edge wake vortex which is also known as "shed vortex" (SV) [37]. Bar wake generator experiments at Ohio State University [38] focused on the addition of synchronized flow control by pulsed vortex generator jets in between the passing wakes to reduce the total pressure losses by as much as 75%. Cui et al. [39] performed LES of the flow through a T106A cascade and found that transition in the presence of high freestream turbulence is dominated by Klebanoff streaks rather than Kelvin-Helmholtz instability. Similarly, LES by Nagabhushana Rao et al. [40] showed that the presence of wakes further increases the dominance of Klebanoff streaks and laminar separation was suppressed. Experiments by Schmitz et al. [25] considered a single stage rotating rig with transonic LPT blades. Observed inconsistencies of the endwall data led to the conclusion that a need exists for models that accurately capture the secondary flow effects and the endwall losses. Experiments in an annular cascade with bar wake generator by Sinkwitz et al. [41] revealed that the wakes weakened the PV and SV. Large-eddy simulations by Cui et al. [42] revealed that with turbulent endwall boundary layer and passing wakes (with secondary flow structures) the total pressure losses were increased substantially over a reference case with

laminar endwall boundary layer and no wakes. The complexity of moving bar generator experiments motivated researchers to explore alternatives for generating unsteady wake effects in linear cascade experiments. For example, the periodic unsteadiness device proposed by Fletcher et al. [43, 44, 45] introduces unsteady wakes without moving parts.

The majority of the earlier LPT wake effect research is for moving bar wake generators. By default, such devices will model the 2-D wake component but cannot capture the endwall structures of the upstream stator vanes. For most of the earlier research, the focus is on the effect of the unsteady wakes on the suction-side 2-D laminar separation which dominates the loss generation for rear-loaded moderate-lift airfoils. For front-loaded high-lift airfoils such as the L2F, the endwall losses contribute considerably to the total pressure losses and the wake effect on the endwall structures is of interest. This motivated ILES of the flow through a linear LPT cascade with L2F airfoils at a Reynolds number based on inlet velocity and axial chord length of 50,000 and 100,000. These Reynolds numbers are at the low end of what is seen on engines during cruise. To allow for a differentiation between the effect of the 2-D turbulent wake and the 3-D endwall flow structures, both a full stage simulation and a simulation for a linear cascade with bar wake generator were carried out. The time-averaged and instantaneous flow fields obtained from both simulations were compared with each other with particular focus on the rotor suction-side separation and endwall structures. The aim of the research was to make a contribution to the understanding of the wake effect on the endwall flow structures and endwall losses.

2 Methodology

2.1 Numerical Method

The compressible Navier-Stokes equations were solved with a finite-volume code by Gross and Fasel [46]. The convective terms were discretized with a ninth-order-accurate weighted essentially non-oscillatory scheme. A fourth-order accurate discretization was employed for the viscous terms. The equations were integrated in time with the second-order-accurate implicit trapezoidal rule. Since no explicit subgrid stress model was employed, the simulations can be referred to as implicit large-eddy simulations (ILES). For ILES, the numerical scheme removes the proper amount of energy at the smallest grid scales. The dynamic viscosity, μ, was obtained from Sutherland's law.

2.2 Non-dimensionalization

All quantities were made dimensionless with the axial chord length, C_{ax}, and the inlet velocity, density, temperature, and dynamic viscosity. The Reynolds number based on relative rotor inlet velocity and axial chord length was 50,000 and 100,000. The reference Mach number for the simulations was $M_{ref} = 0.1$ and low enough to satisfy the incompressible flow assumption. Based on the isentropic flow relationships, for a Mach number of 0.1, the stagnation density is 0.5% above the freestream density. Compared to the changes in the other flow quantities, for the chosen reference Mach number, the changes in density are insignificant. The Prandtl number was $Pr = 0.72$ and the inlet temperature was 300 K.

2.3 Velocities for 50% Reaction Turbine Stage

The L2F airfoil [1] was chosen for both the rotor blade and the stator vane. The L2F design inlet and outlet angle are $\alpha_{in} = 35\ deg$ and $\alpha_{out} = -60\ deg$, respectively, and the blade pitch is $S = 1.221$. The Reynolds number is based on the inlet velocity. The normalized absolute stator and relative rotor inlet velocity magnitude is $V_1 = 1$. The axial and pitchwise velocity at the stator inlet are

$$u_1 = \cos 35deg = 0.8191520 \tag{2.1}$$

and

$$v_1 = \sin 35deg = 0.573576. \tag{2.2}$$

Based on mass conservation, an estimate for the stator exit velocity can be obtained,

$$V_2 = \frac{\cos 35deg}{\cos 60deg} V_1 = 1.63830\,. \tag{2.3}$$

The axial and pitchwise components of the stator exit velocity are $u_2 = V_2 \cos 60deg = 0.819152$ and $v_2 = V_2 \sin 60deg = 1.41881$. Because of the symmetries involved in repeating stages, the velocity triangles for the rotor blade and stator vane are identical (Fig. 2.1). Repeating stages with identical airfoils are also referred to as 50% reaction stages and this terminology is also used here. Because a repeating stage is being considered, the relative pitchwise velocity at the rotor inlet,

$$v_2' = v_2 - v_{rel}, \tag{2.4}$$

has to match the absolute pitchwise velocity at the stator inlet, v_1. Dashes are here used to indicate velocity components in the moving reference frame. From this, the blade speed is obtained as

$$v_{rel} = v_2 - v_1 = 0.845237. \tag{2.5}$$

The time taken for the blade to travel one pitch length (wake passing period) is

$$T = \frac{S}{v_{rel}} = 1.44457\,. \tag{2.6}$$

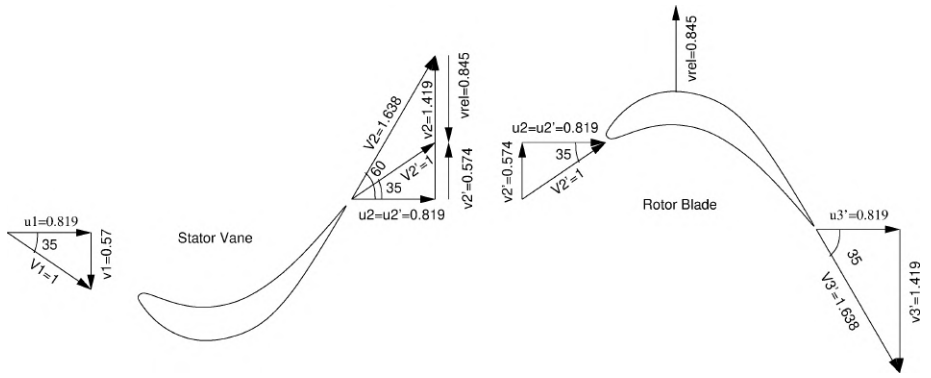

[h]

Figure 2.1: Velocity vectors and flow angles for 50% reaction stage.

2.4 Velocities for Linear Cascade with Bar Wake Generator

For the bar wake generator cases, the inflow velocity magnitude and direction matches the stator outlet conditions ($V_2 = 1.638$ and $\alpha_{out} = -60deg$) (Fig. 2.2).

2.5 Differences between Re=50,000 and Re=100,000 Cases

For the Re=50,000 simulations, the upstream vanes and bar wake generators were moving and the downstream rotor blades were fixed. For the Re=50,000 bar wake generator simulation, the endwall moves relative to the fresstream. This resulted in a cross-flow velocity component near the endwall that led to a faster growth of the endwall boundary layer compared to the 50% reaction stage simulation. To fix this problem, for the Re=100,000 cases, the upstream vanes and bar wake generators were fixed and the downstream rotor blades were moving.

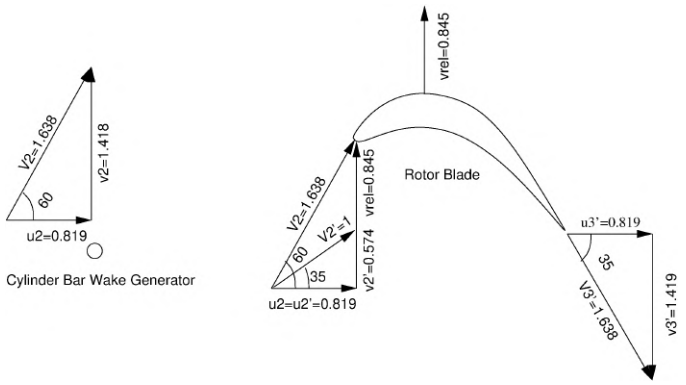

Figure 2.2: Velocity vectors and flow angles for linear cascade with bar wake generator.

2.6 Computational Grids for Re=50,000

Three computational grids were generated for $Re = 50,000$. The first grid is for a 50% reaction stage with two L2F airfoils with an axial separation (stator trailing edge to rotor leading edge) of 0.3. The second and third grids are for an L2F airfoil with two different upstream cylinder bar wake generator. The cylinders have diameters of $D = 0.04$ and 0.12 and the axial distance of the cylinder center to the leading edge of the blade is 0.6. The Reynolds number based on cylinder diameter is 2,000 for $D = 0.04$ and 6,000 for $D = 0.12$.

A Poisson grid generator [47] was employed to generate two-dimensional (2-D) grids with nine and eight blocks (Tab. 2.1 & Figs. 2.3, 2.4). The x-coordinate points in the axial direction and the y-coordinate points in the pitchwise direction. The z-coordinate is normal to the endwall. Grid line stretching was used at the block 8 outflow boundary to dissipate flow structures. Cells were clustered near the stator vane, rotor blade, and cylinder to resolve the boundary layers. Near the sliding mesh interface, the grids were modified to be perfectly equidistant in the axial and pitchwise direction. Blocks 9 and 3 were added at the inflow boundary for accommodating the approach endwall boundary layer. For the 50% reaction stage grid, block 9 is equidistant in the axial and pitchwise direction and has an axial extent of roughly 2 axial chord lengths. Block 3 for the simulation with bar wake generator has an axial extent of only 0.9 as the endwall boundary layer was found to grow faster than for the 50% reaction stage.

The two-dimensional (2-D) grids were extruded over a distance of one axial chord length. Towards that end, a grid line distribution that provides grid line clustering near the endwall to resolve the endwall flow structures and boundary layer was employed. The grid line distribution blends towards an equidistant spacing away from the wall,

$$z_0 = 0 \tag{2.7}$$

$$z_1 = \Delta z \tag{2.8}$$

$$z_k = z_{k-1} + \left[0.1\left(\frac{k-kx}{2-kx}\right)^c + 1\right](z_{k-1} - z_{k-2}) \qquad \text{for } k \geq 2\,. \tag{2.9}$$

Here, k is the spanwise grid line index and $kx = 256$ is the number of grid lines in the spanwise direction. The wall-normal grid line spacing at the endwall was $\Delta z = 10^{-4}$. The total number of cells was 43,200,512 for the 50% reaction stage and 22,996,560 for the bar wake generator cases.

Block	Number of Cells		
	50% reaction stage	Bar wake generator $D = 0.04$	Bar wake generator $D = 0.12$
1	512×48	512×48	512×48
2	512×48	138×96	138×96
3	34×176	159×176	159×176
4	208×128	41×148	41×148
5	18×176	60×176	60×176
6	18×176	18×176	18×176
7	208×128	208×128	208×128
8	24×176	24×176	24×176
9	283×176	-	-

Table 2.1: Number of cells per block for $Re = 50,000$.

The near-wall grid resolution in wall units for the approach BL is provided in Fig. 2.5. For $Re = 50,000$, the near-wall grid resolution in wall units for the approach boundary layer is $\Delta x^+ \approx 16$, $\Delta y^+ \approx 16$, and $\Delta z^+ \approx 0.1$ upstream of the stator and $\Delta x^+ \approx 16$, $\Delta y^+ \approx 20$, and $\Delta z^+ \approx 0.15$ upstream of the bar wake generators and thus close to those employed by Nicoud and Ducros [48] for their LES test problem (28, 8.8, and 2.1, respectively). Contours of the near-wall grid line spacing in wall units for the endwall of blocks 1 and 7 are provided in Figure 2.6. Above the blade, the streamwise, pitchwise, and wall-normal grid line spacing in wall units are roughly 25, 25, and 0.3 which is acceptable for wall-resolved LES. The present grid resolution in wall units is comparable to that of an earlier LES of a linear LPT cascade for a Reynolds number of $100,000$ [49]. For this earlier LES, a detailed validation with wind tunnel data was carried out in lieu of a grid convergence study. The good agreement of these earlier LES results with the experimental data supports the choice of the grid resolution for the present simulations.

The number of cells in the boundary layer ($z \leq \delta$) and viscous sublayer ($z^+ \leq 10$) for the approach boundary layer of the 50% reaction stage simulation (block 9) is plotted in Figure 2.7. Because the wall-normal grid line distribution is constant, as the boundary layer grows in the streamwise direction, the number of cells across the boundary layer is increasing. At the passage inflow, the number of cells across the laminar sublayer is ≈20 and the number of cells across the boundary layer is ≈90, which is sufficient for LES of LPT flows [50].

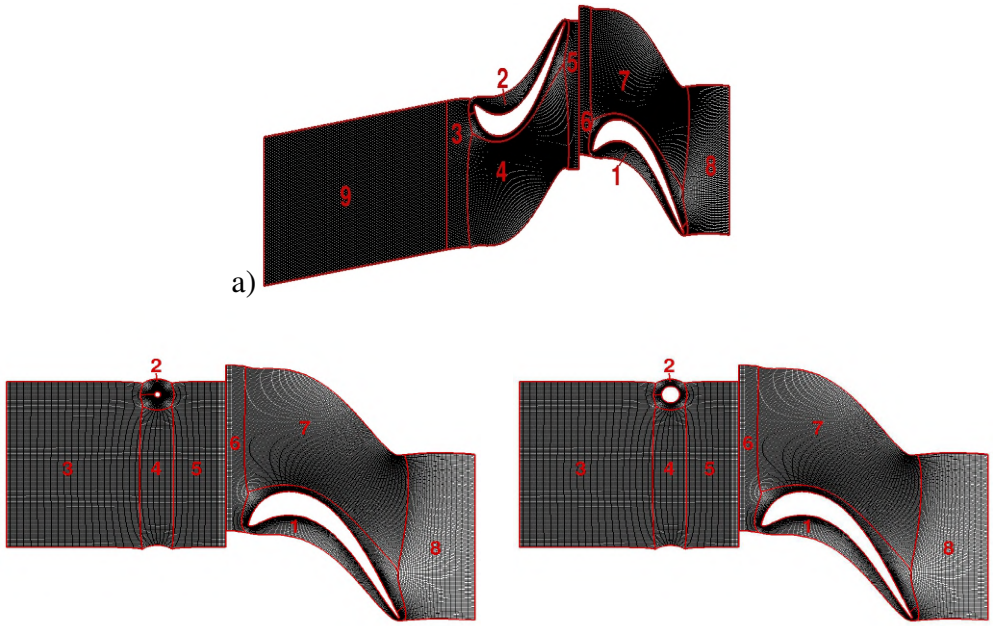

Figure 2.3: Computational grids for a) 50% reaction stage and cascade with b) small and c) large bar wake generator ($Re = 50,000$).

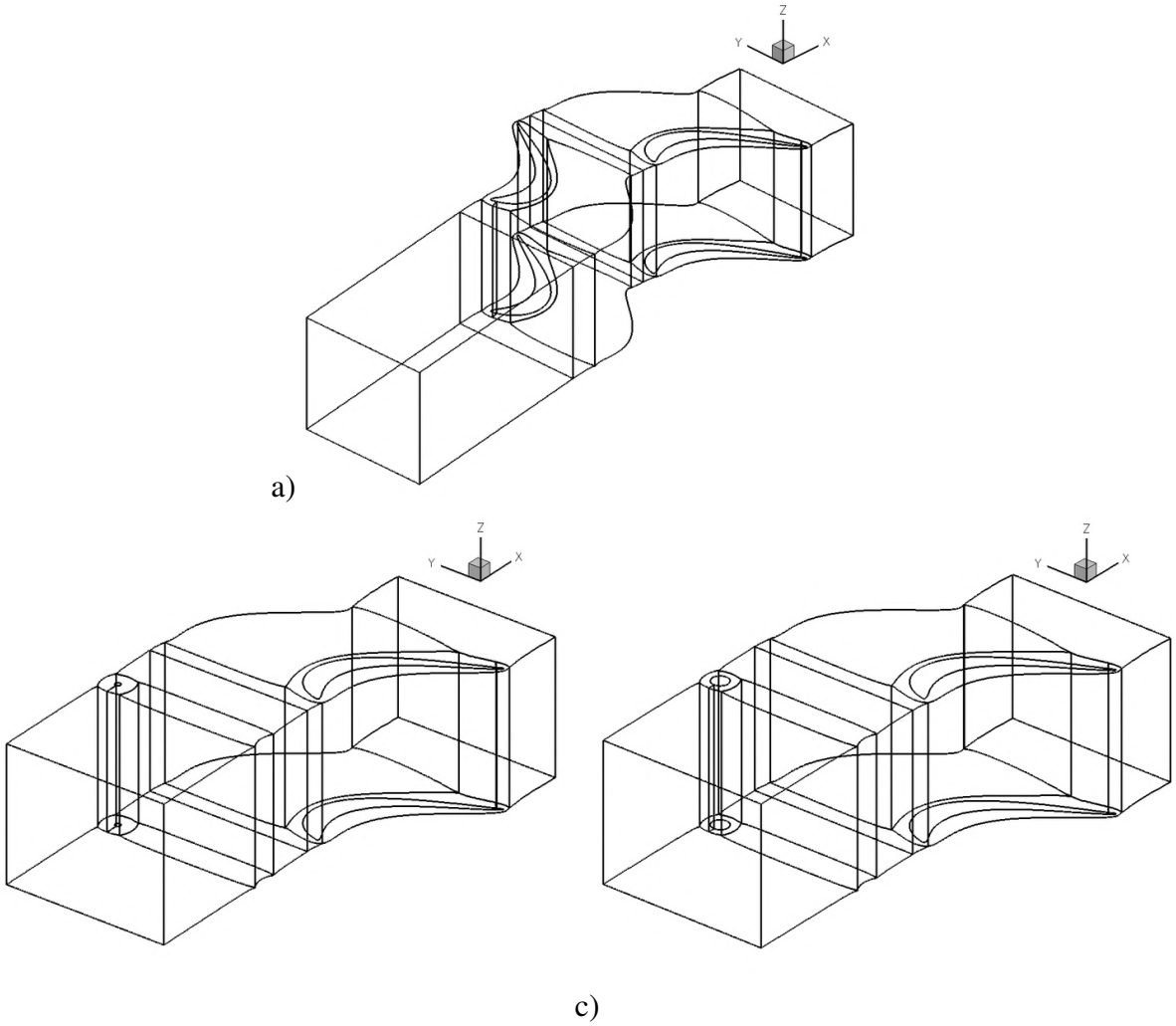

Figure 2.4: Boundaries of 3-D grids and coordinate systems for a) 50% reaction stage and cascade with b) small and c) large bar wake generator ($Re = 50,000$).

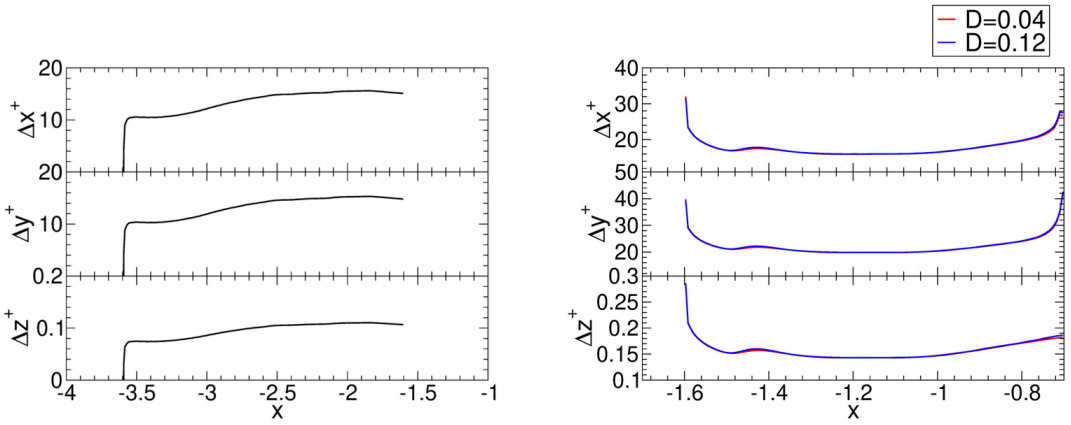

Figure 2.5: Approach flow boundary layer near-wall resolution in wall units for upstream L2F (left) and bar wake generators (right) ($Re = 50,000$).

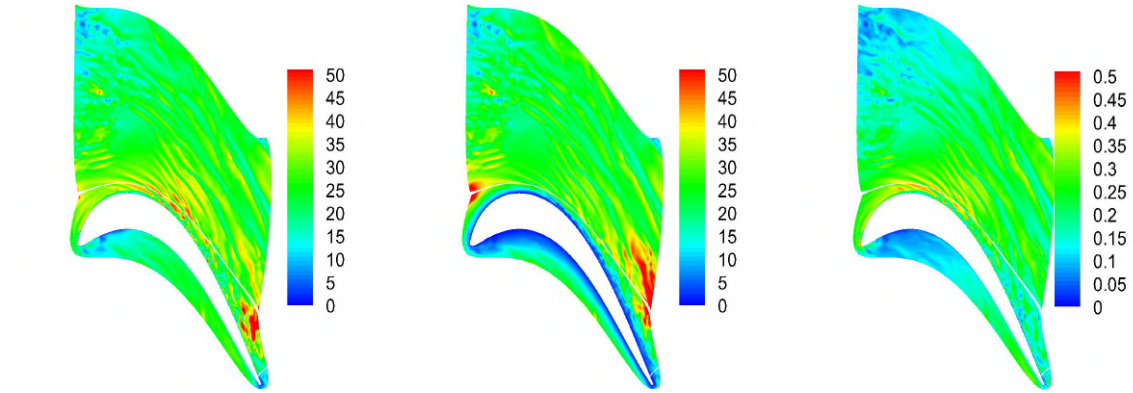

Figure 2.6: Near-wall grid resolutions in wall units. ($Re = 50,000$)

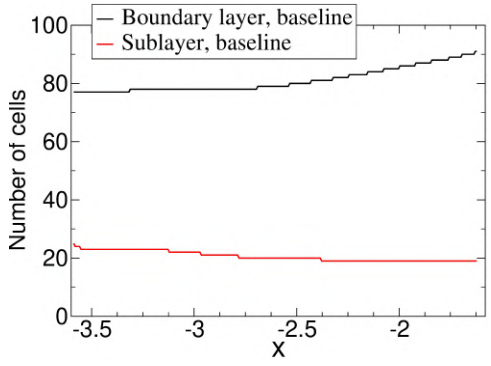

Figure 2.7: Number of cells within boundary layer ($z \leq \delta$) and viscous sublayer ($z^+ \leq 10$)

2.7 Computational Grids for Re=100,000

Only two computational grids were generated for $Re = 100,000$. The 2-D and 3-D grids are presented in Figs. 2.8 and 2.9, respectively. The number of cells per block is provided in Tab. 2.2. For the bar wake generator case, the cylinder diameter is $D = 0.04$ and the Reynolds number based on cylinder diameter is 4,000. Block 9 for the 50% reaction stage has an axial extent of 4.1 and a pitchwise extent that is only one quarter of the blade pitch. This was done deliberately to save grid points. Different from the $Re = 50,000$ bar wake generator simulations, for the $Re = 100,000$ bar wake generator simulation an additional inflow block with an axial extent of 2.5 was added.

The spanwise grid extent of one for the $Re = 50,000$ simulations was found to result in an acceleration of the freestream which was explained by the boundary layer displacement effect. To reduce this effect, for the Re=100,000 cases the 2-D grids were extruded in the spanwise direction over a distance of two axial chord lengths which is close to the spanwise dimensions of related AFRL wind tunnel experiments [8]. The number of grid lines in the spanwise direction for the Re=100,000 simulations was $kx = 384$. The total number of cells was 64,800,768 for the case with upstream L2F and 31,655,424 for the case with upstream bar wake generator. The near-wall resolution in wall units for the approach endwall boundary layer was $\Delta x^+ \approx 28$, $\Delta y^+ \approx 26$, and $\Delta z^+ \approx 0.2$ for the 50% reaction stage simulation and $\Delta x^+ \approx 44$, $\Delta y^+ \approx 40$, and $\Delta z^+ \approx 0.3$ for the bar wake generator simulation 2.10. The maximum streamwise, pitchwise, and wall-normal grid line spacing in wall units for the stator passage are roughly 40, 40, and 0.5 (Fig. 2.11). Although these numbers are slightly higher than for the lower Reynolds number simulations, they are still acceptable for LES [48].

Block	Number of Cells	
	Upstream L2F	Bar Wake Generator
1	512 × 48	512 × 48
2	512 × 48	138 × 88
3	34 × 176	61 × 176
4	208 × 128	41 × 148
5	18 × 176	16 × 176
6	18 × 176	16 × 176
7	208 × 128	208 × 128
8	24 × 176	24 × 176
9	546 × 42	354 × 44

Table 2.2: Number of cells per block for $Re = 100,000$.

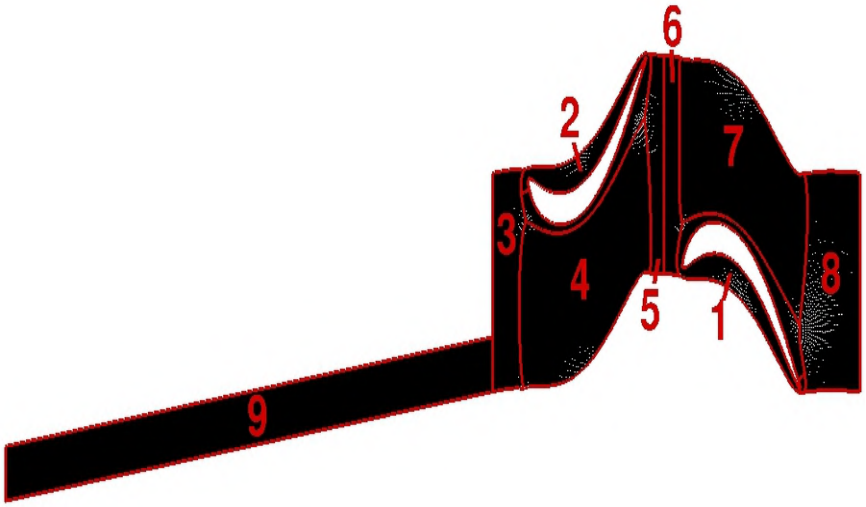

a)

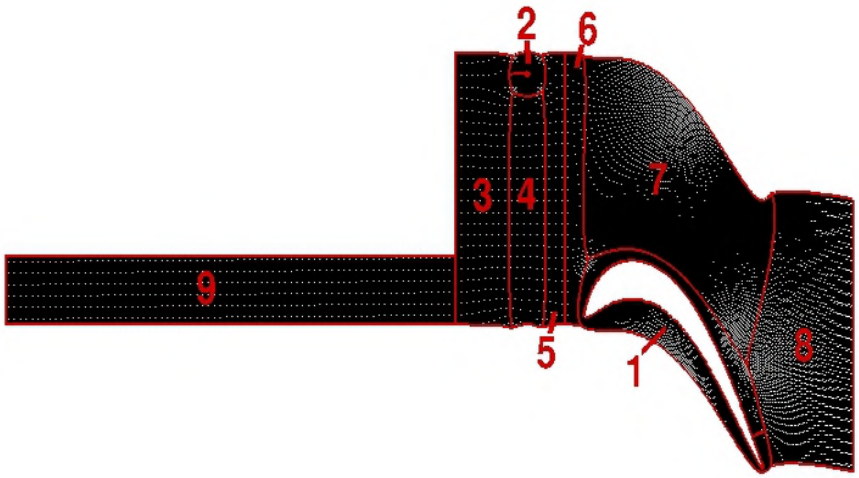

b)

Figure 2.8: Computational grids for a) 50% reaction stage and b) cascade with bar wake generator ($Re = 100,000$).

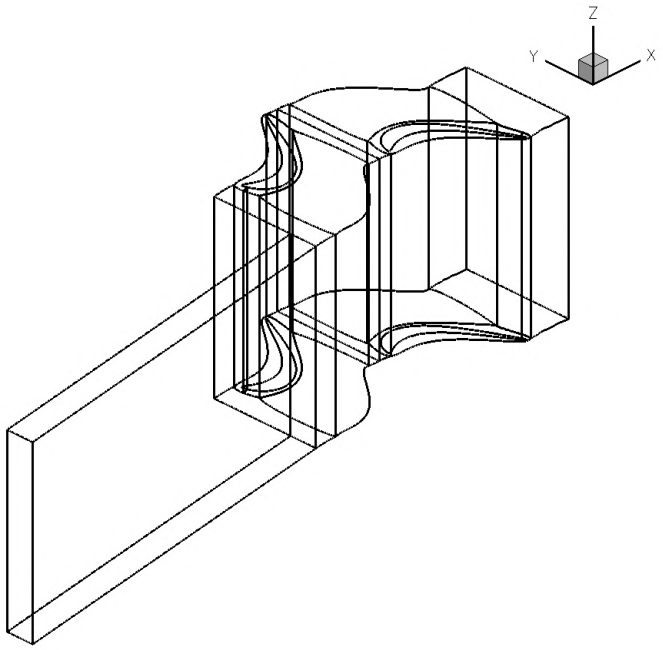

a)

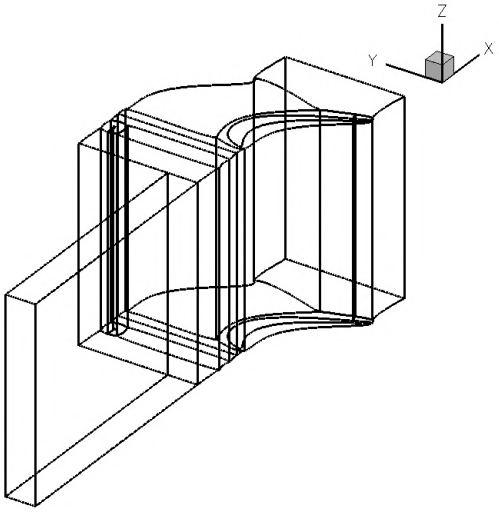

b)

Figure 2.9: Boundaries of 3-D grids and coordinate systems for a) 50% reaction stage and b) cascade with bar wake generator ($Re = 100,000$).

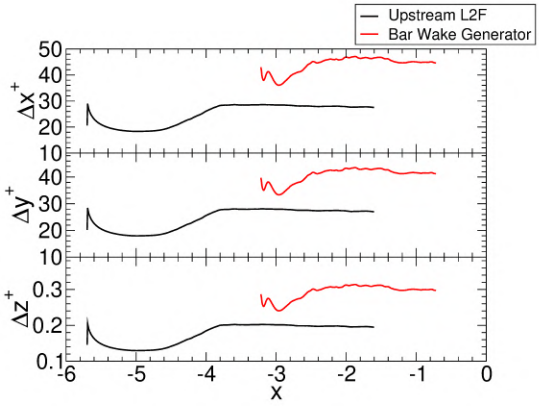

Figure 2.10: Approach flow boundary layer near-wall resolution in wall units ($Re = 100,000$).

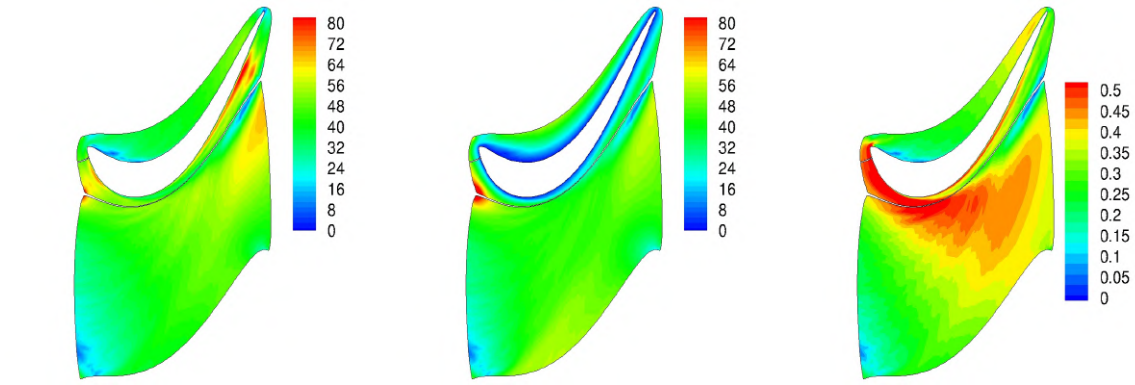

Figure 2.11: Near-wall grid resolutions in wall units ($Re = 100,000$).

2.8 Boundary Conditions

All walls were considered as adiabatic. Flow periodicity was enforced in the pitchwise direction. Non-reflecting boundary conditions [51] were applied at the inflow and outflow boundaries. Symmetry conditions (slip wall) were enforced at the open spanwise boundary.

2.9 Computational Timestep and Time Intervals

The computational time step for all LPT simulations was $\Delta t = 0.00481522$ (300 timesteps per wake passing period). The number of periods for the phase averaging, N_{av}, and the time intervals, Δt_{av}, for the time averaging are provided in Table 2.3.

Case	Number of Periods	Time Interval
Re=50,000		
L2F	8	11.56
Small Cylinder, D=0.04	9	13.01
Large Cylinder, D=0.12	7	10.11
Re=100,000		
L2F	10	14.5
Cylinder, D=0.04	10	14.5

Table 2.3: Number of periods for phase-averaging and time intervals for time averaging.

2.10 Sliding Mesh

A sliding mesh technique [52] was employed at interfaces where relative motion occurs. This method is based on the assumption that both grid and data are periodic in the pitchwise direction. This situation is characteristic of turbomachinery stages where stator vanes and rotor blades are spaced at a constant pitch (azimuthal interval). Close to the interface, the grid is assumed to be perfectly equidistant and rectangular such that the flow field in the pitchwise direction can be expressed as a function of the pitchwise cell index, i. The total number of cells at the interface in the pitchwise direction, counted from 0, is ix. The shift is accomplished using Fourier transforms which are by nature periodic. The forward Fourier transforms are

$$\hat{u}_{c,j} = \sum_{i=0}^{ix} u_i \cos \frac{2\pi ij}{ix+1} \tag{2.10}$$

$$\hat{u}_{s,j} = \sum_{i=0}^{ix} -u_i \sin \frac{2\pi ij}{ix+1}\,, \tag{2.11}$$

where $1 < j < (ix+1)/2$ is the Fourier mode number. Fourier mode $j = 0$ is computed from,

$$\hat{u}_{c,0} = \sum_{i=0}^{ix} u_i\,. \tag{2.12}$$

The backward transformation is

$$u_i = \frac{1}{ix+1}\left\{\hat{u}_{c,0} + 2\sum_{j=1}^{(jx+1)/2}\left[\hat{u}_{c,j}\cos\frac{2\pi(i+s)j}{ix+1} - \hat{u}_{s,j}\sin\frac{2\pi(i+s)j}{ix+1}\right]\right\}, \tag{2.13}$$

where $s = v_{rel}t/S \times ix$ is the relative pitchwise shift along the interface, v_{rel} is the velocity of the relative motion, S is the blade pitch, and t is time.

2.11 Synthetic Eddy Method

The divergence-free isotropic synthetic eddy model (SEM, Jarrin et al. [53], Poletto et al. [54]) was employed for initiating (or seeding) the turbulent endwall boundary layer. Because this model is driven by a random number generator, it does not favor certain frequencies (or wavelengths). Mankbadi et al. [55] compared the SEM with the digital filtering method (Klein et al. [56]) and found that both models require an adjustment length of roughly six boundary layer thicknesses.

For the present simulations, a box with volume V_b was initialized with a random distribution of $N = 5,000$ eddies. The box had the dimensions of the inflow boundary layer thickness, δ, and blade pitch, and a streamwise extent of

$$2\sigma_{max} = 2\max_N(\sigma_k)\,. \tag{2.14}$$

For the SEM, the size of each eddy, k,

$$\sigma_k = \max(\min[\ell, 0.41\delta], \Delta_{max}) \tag{2.15}$$

is defined based on the turbulent length scale at the wall-normal location of the eddy,

$$\ell = \frac{k^{\frac{3}{2}}}{\varepsilon}\,, \tag{2.16}$$

with turbulence kinetic energy (TKE), k, and dissipation rate, ε. The grid length scale,

$$\Delta_{max} = \max(\Delta x, \Delta y, \Delta z)\,, \tag{2.17}$$

is taken as the maximum of the cell dimensions, Δx, Δy, and Δz, at the location of the eddies. Boundary layer profiles obtained from a precursor Reynolds-averaged Navier–Stokes (RANS) calculations with k-ω model (Figure 2.12) served as basis for the SEM and provided the mean quantities, $\overline{\mathbf{u}}(y)$, $k(y)$, $\varepsilon(y)$, and δ, where y is the wall distance.

In the ILES, the eddies induce velocities at the inflow boundary of the computational domain. The velocity fluctuations are computed as the sum over all N eddies,

$$\mathbf{v}' = \sqrt{\frac{1}{N}}\sum_N \frac{\mathbf{r}_k \times \mathbf{e}_k}{\mathbf{r}_k^3} f(\sigma_k, \mathbf{r}_k) \times \sqrt{\frac{2}{3}k}\,, \tag{2.18}$$

and added to the mean flow profile, $\overline{\mathbf{u}}(y)$. Here,

$$\mathbf{r}_k = \frac{\mathbf{x} - \mathbf{x}_k}{\sigma_k} \tag{2.19}$$

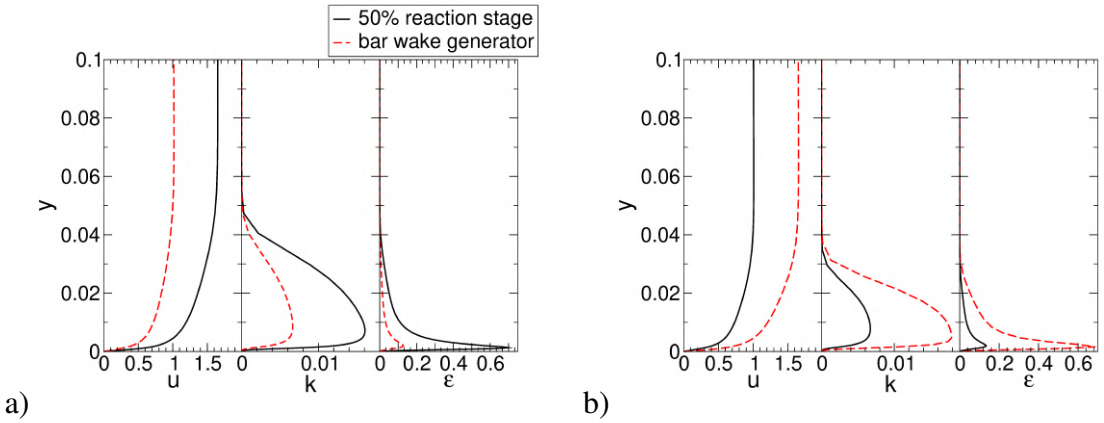

Figure 2.12: RANS profiles for a) $Re = 50,000$ and b) $Re = 100,000$.

is the location vector from an eddy to a point on the inflow boundary normalized by the eddy size. The TKE, k, is taken at the wall-normal location of the individual eddies. The orientation vectors for each eddy, k, are randomized with either plus or minus one,

$$\mathbf{e}_k = \begin{bmatrix} \text{random}(\pm 1) \\ \text{random}(\pm 1) \\ \text{random}(\pm 1) \end{bmatrix}. \tag{2.20}$$

The shape function is given by

$$f(\sigma_k, \mathbf{r}_k) = \begin{cases} \sqrt{\frac{16 V_b}{15\pi\sigma_k^3}} \sin^2(\pi|\mathbf{r}_k|)|\mathbf{r}_k| & |\mathbf{r}_k| < 1 \\ 0 & \text{otherwise} \end{cases} \tag{2.21}$$

The pressure and temperature are obtained from the approach flow stagnation values assuming an isentropic state change. After each timestep, the vortices are convected in the streamwise direction by the freestream velocity. Vortices that leave the box are regenerated at random locations and with random orientations on the inflow plane of the box.

3 Results for Re=50,000

3.1 Approach Flow Analysis

Iso-surfaces of the Q-criterion by Hunt [57] flooded by the streamwise velocity for the approach flow endwall boundary layer are provided in Figs. 3.1 and 3.2. For all cases, the boundary layer grows in the streamwise direction and is fully turbulent on impact with the stator vane or cylinder leading edge. Near-wall streaky structures resulting from crossflow instability can be observed for the bar wake generator cases.

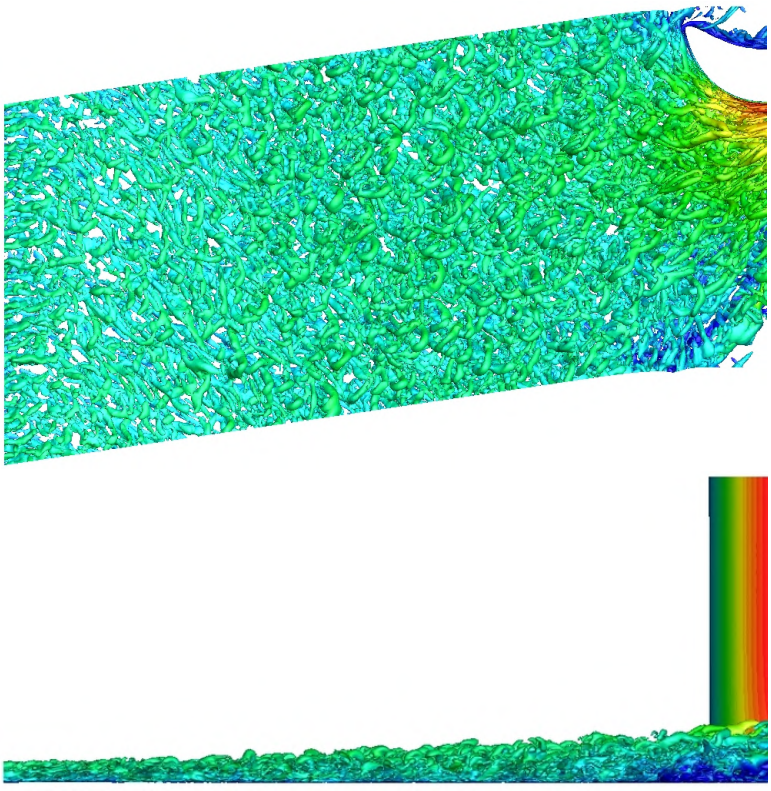

Figure 3.1: Instantaneous iso-surfaces of $Q = 10$ colored by streamwise velocity for 50% reaction stage.

Velocity profiles $1/2C_x$ upstream of the stator vane and bar wake generator leading edge are provided in Fig. 3.3. The subscripts 35 and 60 refer to velocity components relative to the 35 and 60 deg incidence angle. For the 50% reaction stage case, v_{35} is zero and u_{35} is almost 1 in the freestream. For the bar wake generator cases, because the endwall is moving relative to the freestream, u_{35} and v_{35} are non-zero at the endwall which is typical for actual turbines. In the

inertial frame, v'_{60} has a small non-zero region just above the endwall and u'_{60} approaches 1.6 in the freestream. In Fig. 3.4 the profiles $1/2C_x$ upstream of the stator vane and bar wake generator leading edge are plotted in wall units. Included are the relationships for the laminar sublayer, $u^+ = y^+$, and for the law of the wall, $u^+ = 5 + \ln y^+/0.41$. At this location, a fully turbulent profile is obtained for the 50% reaction stage. For the cases with bar wake generator, the log-layer is not well developed. The displacement thickness, δ^*, momentum thickness, ϑ, and shape factor, H, for the approach flow are plotted in Fig. 3.5. For the bar wake generator cases, the boundary layer grows more quickly, likely as a result of the strong crossflow. The shape factor for all cases is approaching 1.5 which is a typical value for low-Reynolds number turbulent boundary layer flows as shown by Purtell et al [58].

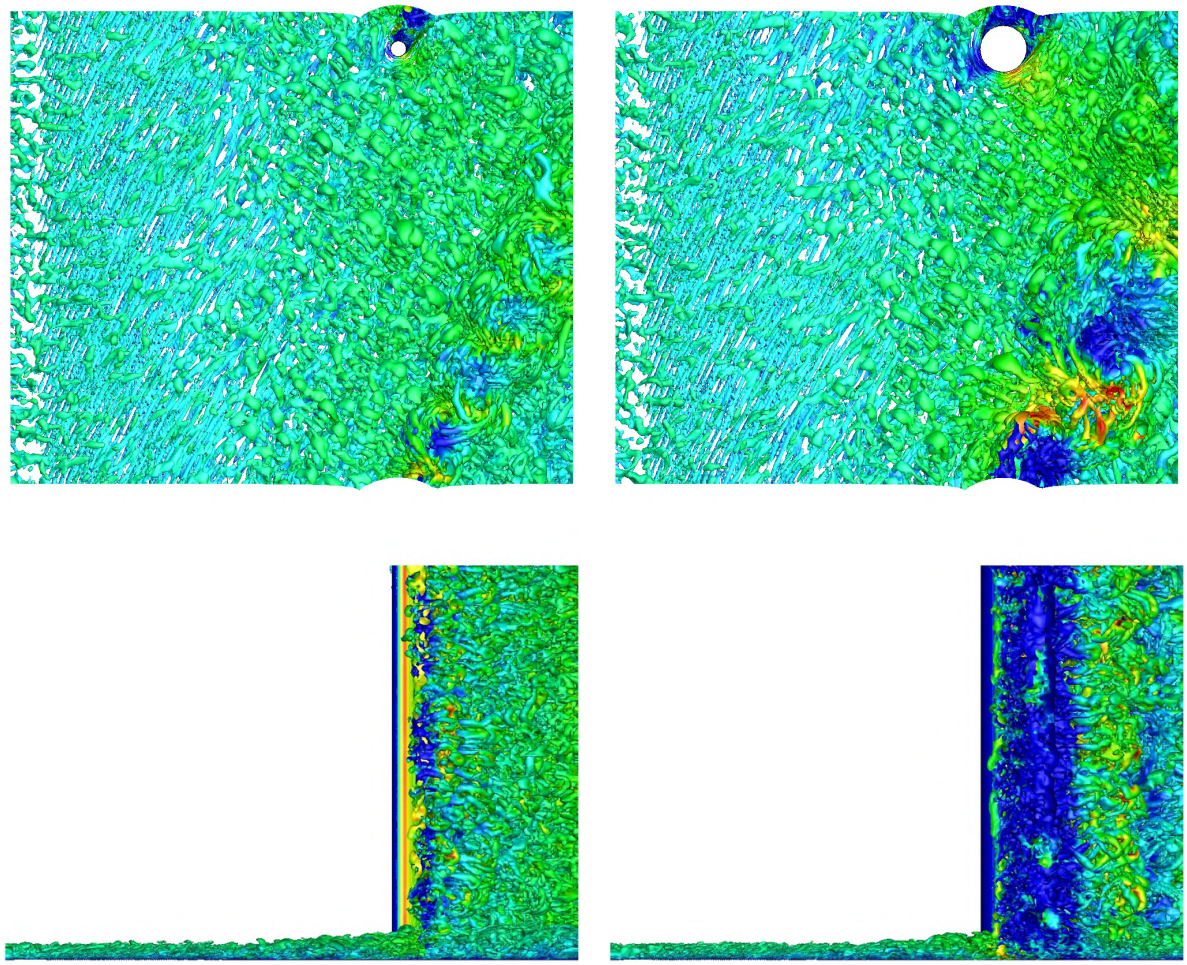

Figure 3.2: Instantaneous iso-surfaces of $Q = 10$ colored by streamwise velocity for small bar wake generator (left) and large bar wake generator (right).

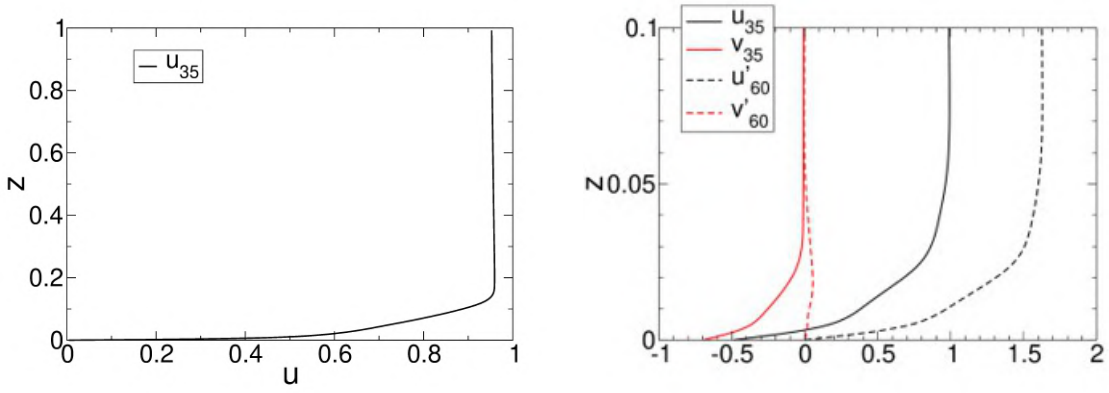

Figure 3.3: Time-averaged velocity profiles $1/2C_x$ upstream of stator vane (left) and bar wake generators (right).

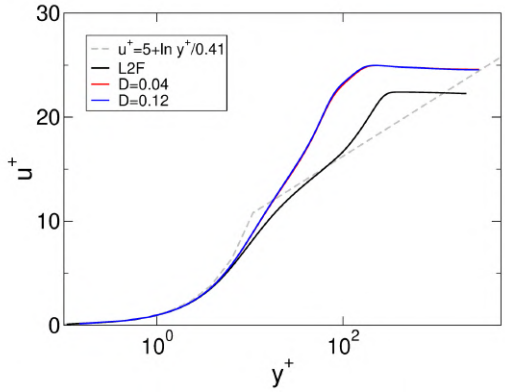

Figure 3.4: Velocity profiles in wall units $1/2C_x$ upstream of stator vane and bar wake generators (time-averaged flow).

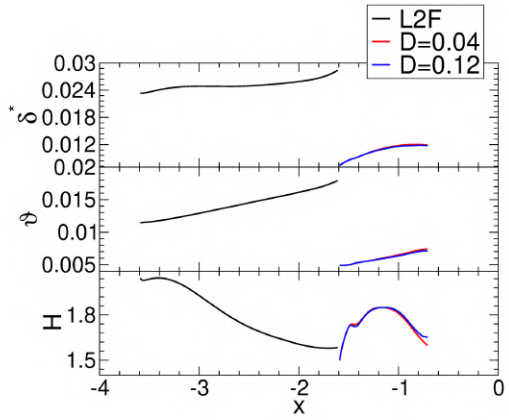

Figure 3.5: Approach flow displacement thickness, momentum thickness, and shape factor for all cases.

3.2 Wake Analysis

Iso-surfaces of the vortex identification criterion Q flooded by the wall-normal distance for the phased-averaged flow fields are displayed in Figs. 3.6, 3.7, and 3.8. The iso-surfaces are flooded by the distance to the endwall. This allows for a differentiation of the near-wall structures from flow features farther away from the endwall. The upstream L2F and the cylinder shed unsteady wakes as they travel in the pitchwise (transverse) direction. The iso-surfaces suggest that the wake width for the upstream L2F and smaller bar wake generator are similar shortly upstream of the downstream rotor blades. As the wakes pass through the downstream passage they stretch to form a Λ shape. This can be explained by the faster flow in the center of the passage compared to the slower flow near the blades. The wake appears much wider for the larger diameter case. For the 50% reaction stage simulation, in agreement with Romero and Gross [59], a transient longitudinal flow structure is seen intermittently near the trailing edge of the pressure side.

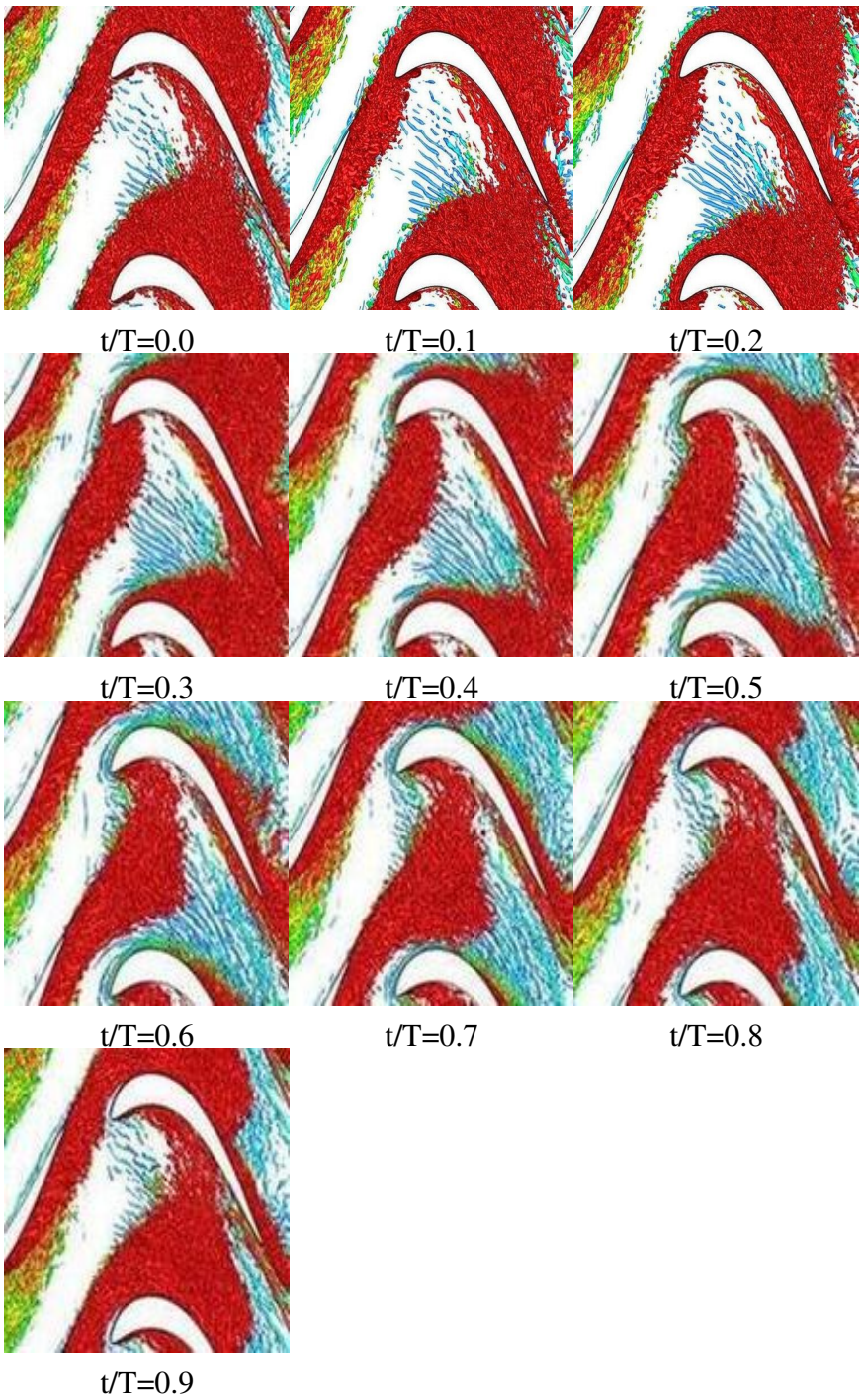

Figure 3.6: Iso-surfaces of $Q = 25$ flooded by wall distance ($z > 0.02$ is red) for 50% reaction stage (phase-averaged flow).

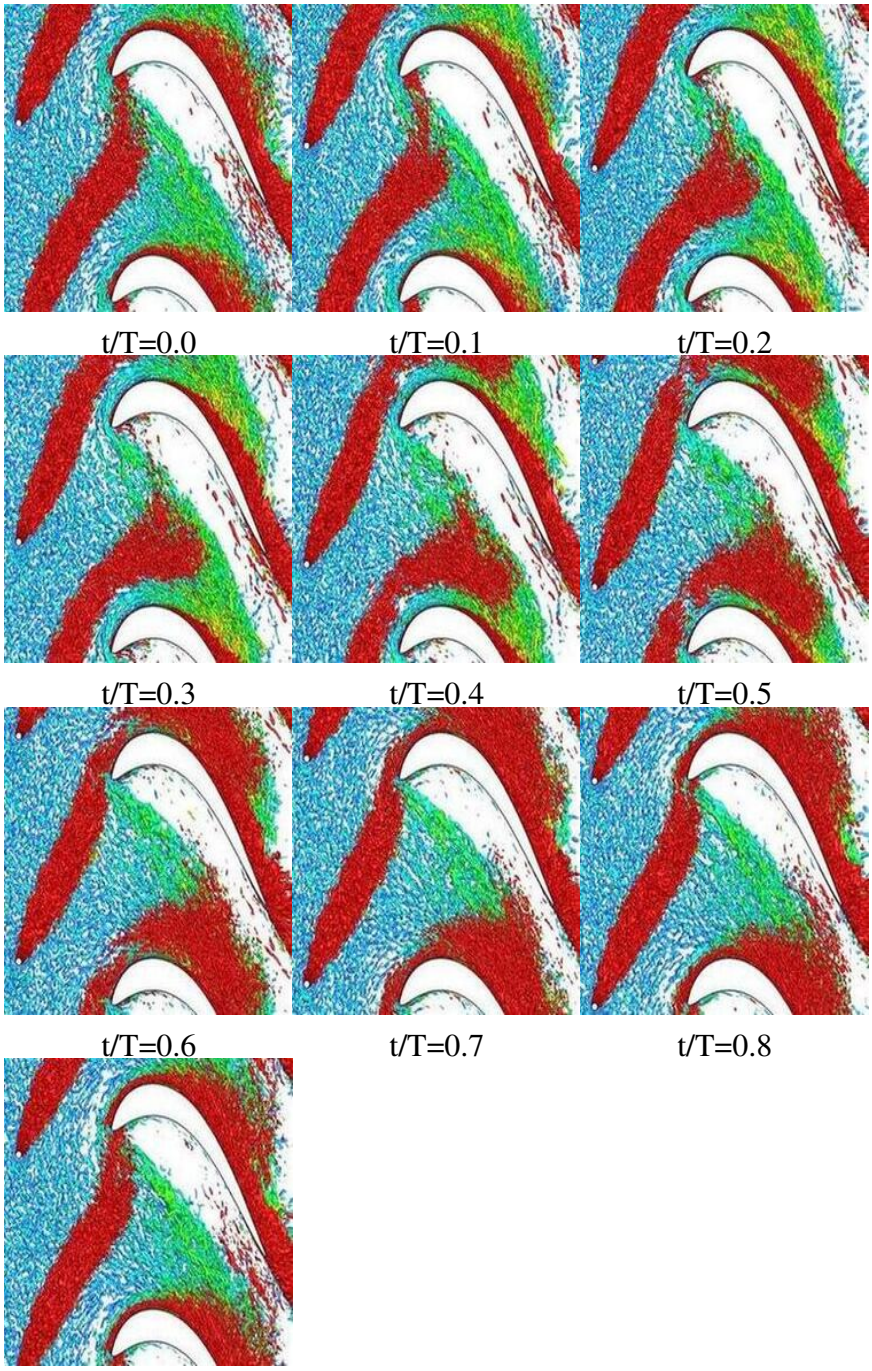

Figure 3.7: Iso-surfaces of $Q = 25$ flooded by wall distance ($z > 0.02$ is red) for small bar wake generator (phase-averaged flow).

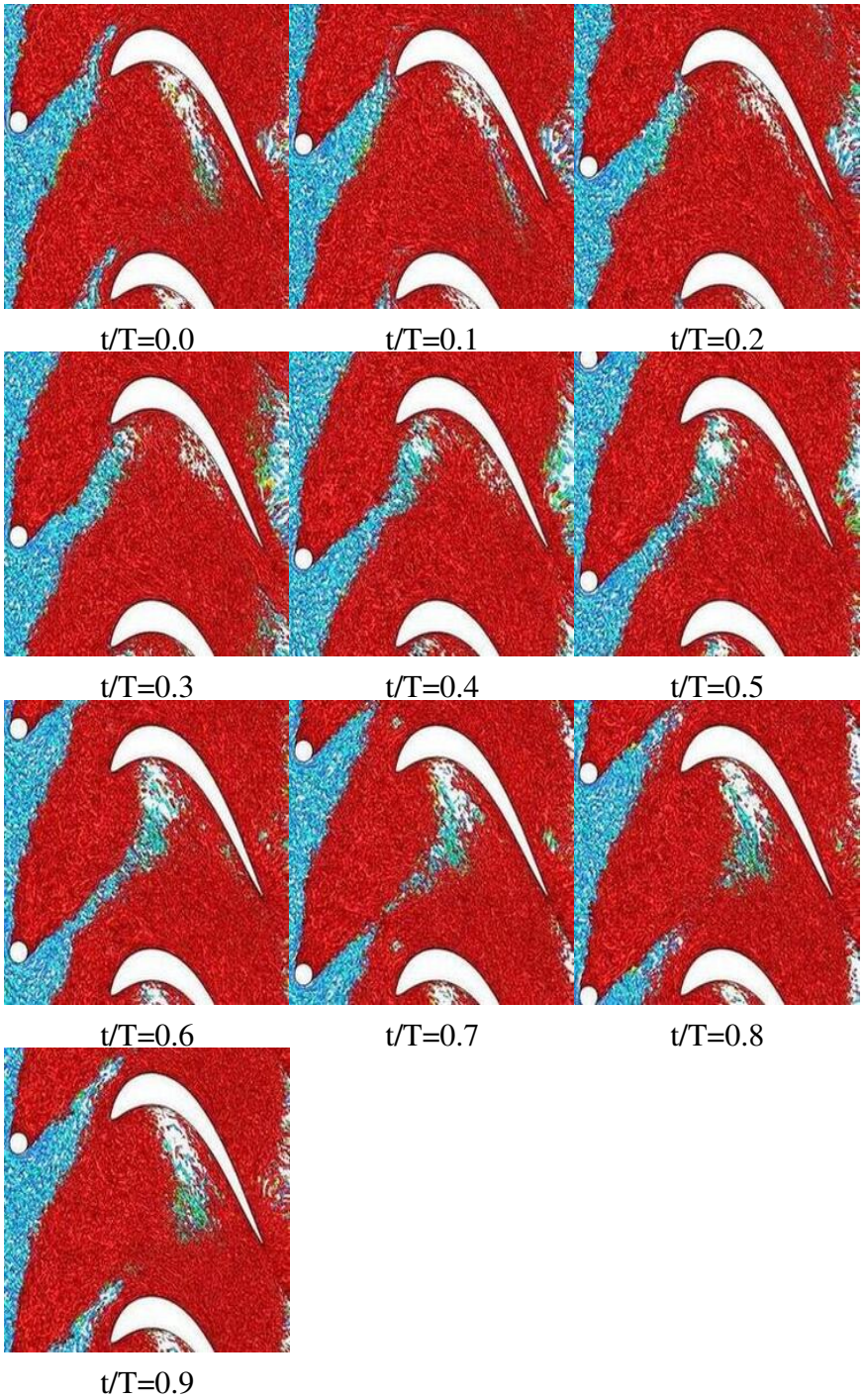

Figure 3.8: Iso-surfaces of $Q = 25$ flooded by wall distance ($z > 0.02$ is red) for large bar wake generator (phase-averaged flow).

[H] a) b)

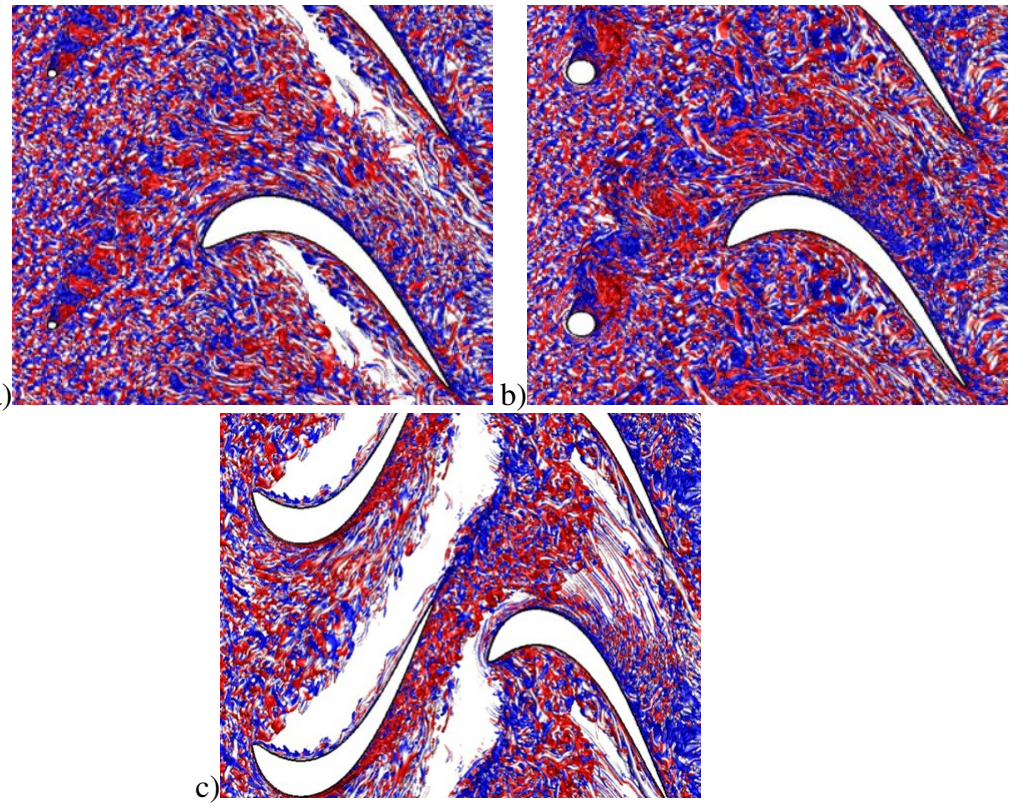

c)

Figure 3.9: Instantaneous iso-surfaces of $Q = 25$ colored by wall normal vorticity for a) small, b) large bar wake generator, and c) 50% reaction stage.

Instantaneous iso-surfaces of Q flooded by the wall-normal vorticity, ω_z, are presented in Fig. 3.9 for each case. The bar wake generator cases exhibit a von Kármán vortex street which equates to an unsteady wake disturbance with fixed frequency. For the smaller diameter cylinder, the vortices are spaced more closely. No distinct spanwise coherent structures are visible for the 50% reaction stage simulation.

The streamwise velocity and vorticity at the stator inflow plane were computed as $u_{in} = u\cos(35deg) + v\sin(35deg)$ and $\omega_{in} = \omega_x\cos(35deg) + \omega_y\sin(35deg)$, respectively. Iso-contours of both quantities for the time-averaged flow field for the upstream face of block 6 ($x = -0.149$) are provided in Fig. 3.10. These visualizations allow for a comparison of the wake shape and velocity deficit. The upstream L2F creates a considerably stronger wake than the small cylinder. The wake for the former is both wider and has a stronger velocity deficit. When compared to the large diameter cylinder, the 50% reaction stage still produces a larger velocity deficit but the wake width is similar. For the bar wake generators, the endwall boundary layer is thicker, likely as a result of the moving wall as explained earlier. The contours of ω_{in} reveal strong secondary flow structures for the reaction stage that can be related to the PV and SV. For the bar wake generators, the wakes are more 2-D and no pronounced endwall structures can be discerned. To further quantify the difference between the wakes, the streamwise velocity was averaged in the z-direction over the spanwise interval $0.198 < z < 0.791$ (see Fig. 3.11). The peak velocity deficit is almost 0.8 for the upstream L2F and about 0.25 and 0.45 for the small and large cylinders, respectively. The wake half width is roughly 0.2 for the upstream L2F and the small cylinder and about 0.3 for the large

cylinder.

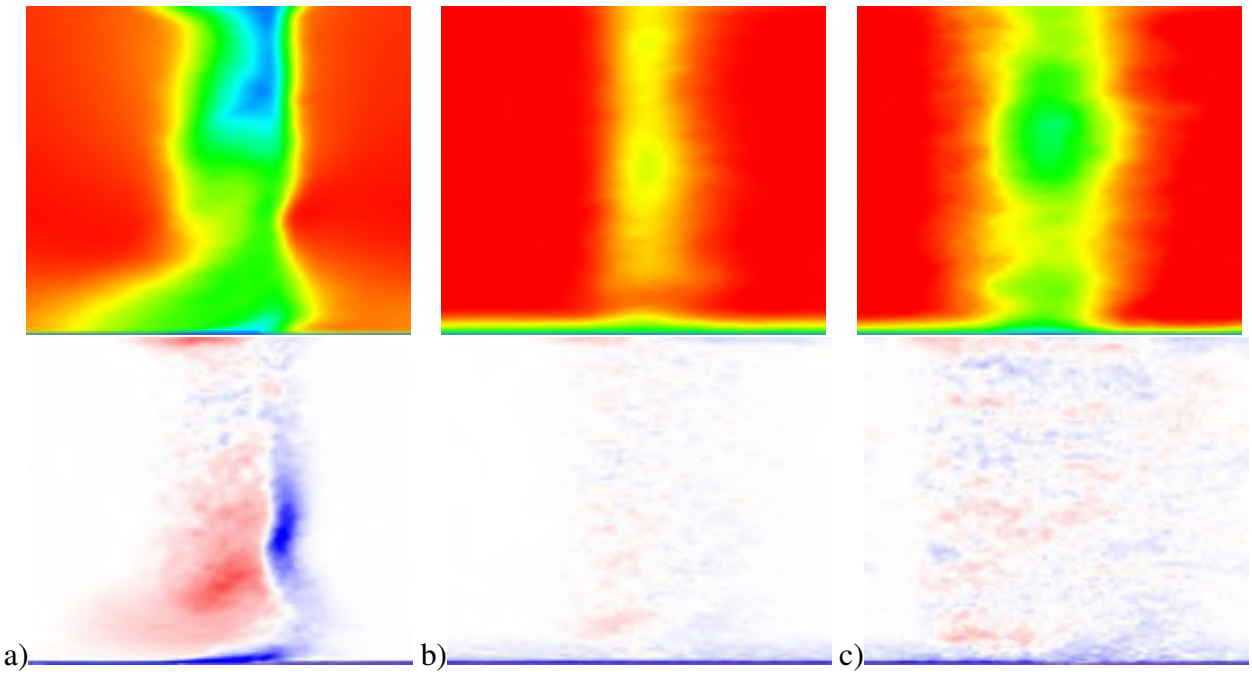

Figure 3.10: Iso-contours of streamwise velocity, $0 < u_{in} < 1$, (top) and streamwise vorticity, $-20 < \omega_{in} < 20$, (bottom) for a) 50% reaction stage and b) small and c) large bar wake generator (time-averaged flow).

The integral wake momentum deficit was calculated as

$$\vartheta = \int_S \frac{u}{U}(1 - \frac{u}{U})dy \tag{3.1}$$

for the data averaged over $0.65 < z < 1$ where S is the blade pitch. In addition, ϑ was also computed by integration over the entire inflow area,

$$\vartheta = \frac{1}{z}\int_A \frac{u}{U}(1 - \frac{u}{U})dA, \tag{3.2}$$

where $z = 1$ is the spanwise extent of the computational domain. The results for each case are provided in Tab. 3.1. The large cylinder has a similar 2-D and 3-D wake momentum deficit as the 50% reaction stage. Also for the large cylinder case, the momentum deficits are roughly two times larger than for the small cylinder case.

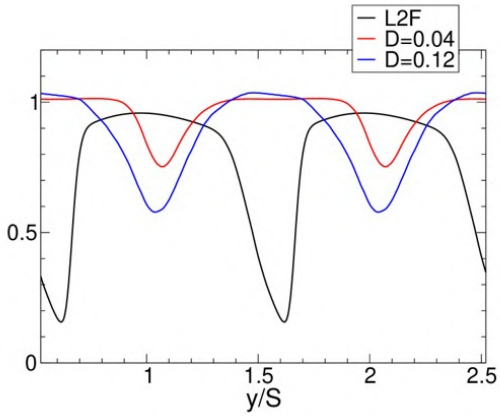

Figure 3.11: Wake profiles of u_{in} for $x = -0.149$ averaged over $0.198 < z < 0.791$.

	2-D $0.65 < z < 1$	3-D $0 < z < 1$
L2F	0.1158	0.1101
$D = 0.04$	0.0410	0.0341
$D = 0.12$	0.0809	0.0790

Table 3.1: Two- and three-dimensional wake momentum deficit.

3.3 Mean Flow Analysis

Iso-contours of the axial skin-friction coefficient, $-0.01 < c_{f,x} < 0.01$, with skin-friction lines and iso-surfaces of Q flooded by the streamwise vorticity, w_x, are displayed in Fig. 3.12. The flow visualizations show no evidence of the PV in the time-average. Longitudinal near-wall vortices can be observed near the pressure side. As shown by Gross et al. [17] they may be a product of cross-flow instability. Iso-surfaces of Q and skin-friction lines for the suction surface of the stator vane and rotor blade are provided in Fig. 3.13. The skin-friction lines for the upstream vane reveal a laminar separation bubble and corner separation. The visualizations for the downstream blade manifest a complete suppression of the laminar corner separation. The unsteady nature of the suction side BL separation was further investigated. Towards that end the axial skin-friction coefficient averaged over $0.60 < z < 1$ was plotted versus time (Fig. 3.14). The passing wakes intermittently transition the laminar suction side boundary layer and suppress flow separation in agreement with the literature [26]. High skin-friction turbulent patches are followed by laminar or "calmed" regions. This mechanism is exploited for the design of ultra-high-lift airfoils [60].

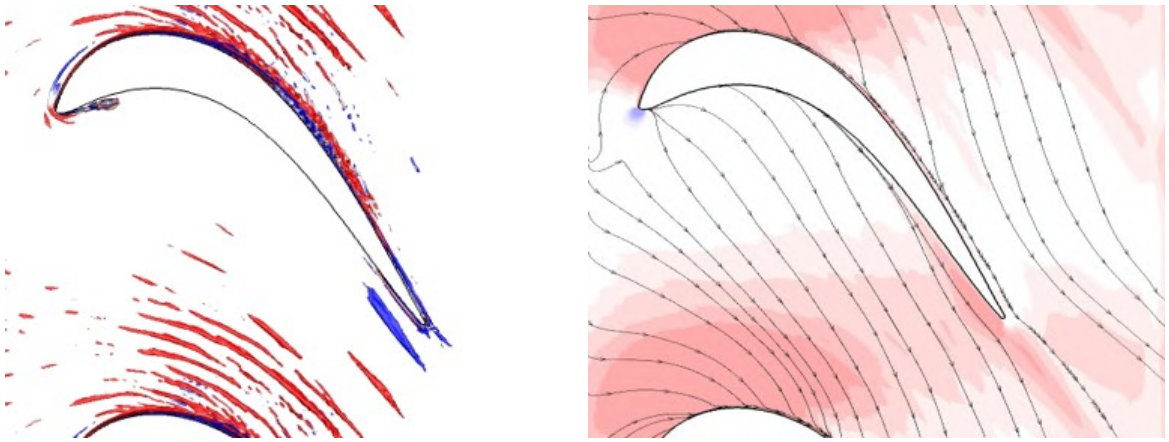

Figure 3.12: Iso-surfaces of $Q = 25$ flooded by $-5 < w_x < 5$ (left) and skin-friction lines and iso-contours of $-0.01 < c_{f,x} < 0.01$ (right) for stator vane (downstream L2F) of 50% reaction stage (time-averaged flow).

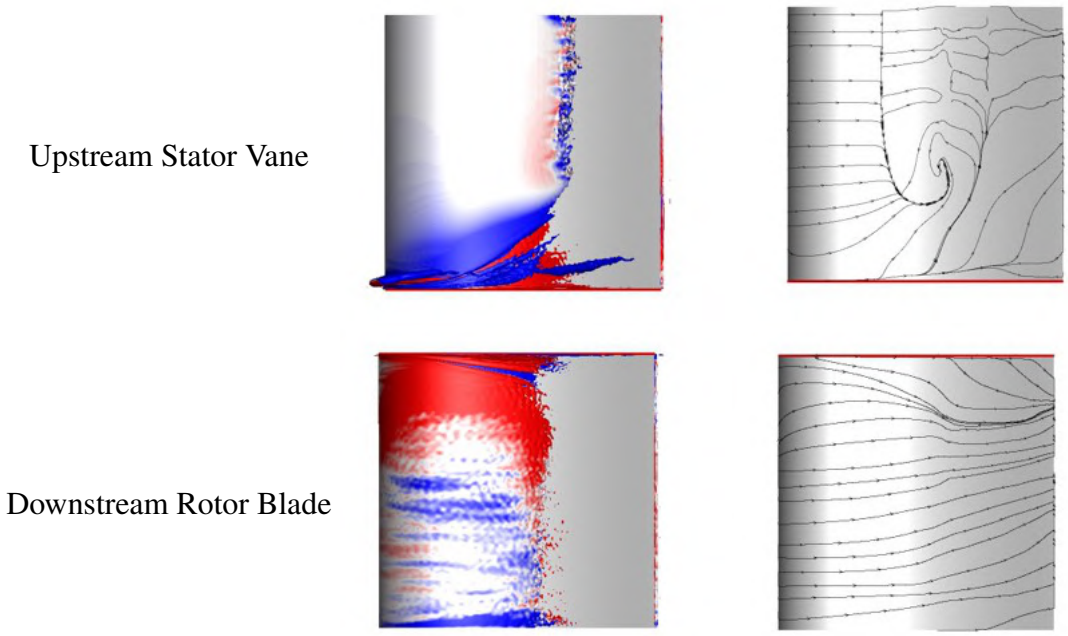

Figure 3.13: Iso-surfaces of $Q = 25$ flooded by $-5 < w_x < 5$ (left) and skin-friction lines (right) for 50% reaction stage. Endwall marked by red line (time-averaged flow).

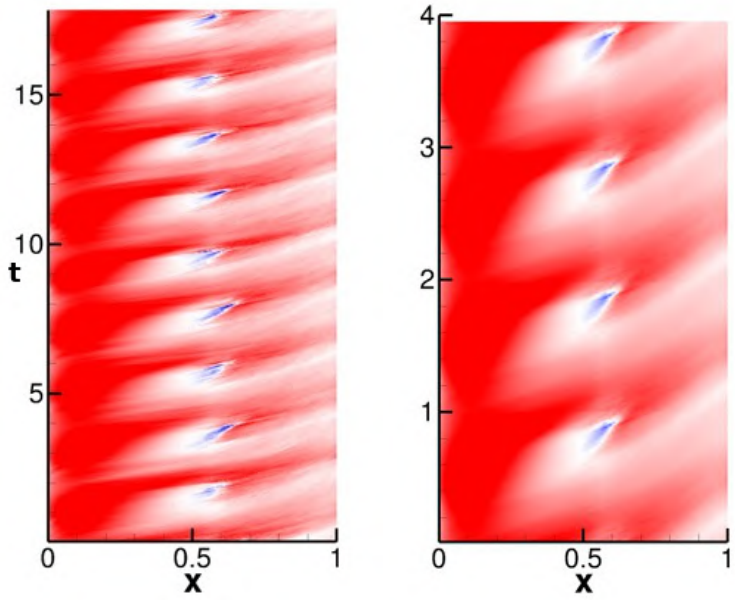

Figure 3.14: Iso-contours of $-0.01 < c_{f,x} < 0.01$ for suction surface of downstream blade averaged over $0.60 < z < 1$ for instantaneous flow (left) and phase-averaged flow (right) for 50% reaction stage.

Skin-friction lines were also generated for the pressure surfaces (Fig. 3.15). The skin-friction lines indicate a leading edge corner separation for the upstream airfoil and a 2-D laminar separation slightly downstream from the leading edge for the downstream airfoil. The flow angle contours in Fig. 3.16, reveal that the wakes cause an intermittent reduction of the mean angle of attack which may explain the pressure side flow separation. Separation from the upstream stator vane is also reduced when it passes by the rotor blade, likely as a result of an interference effect.

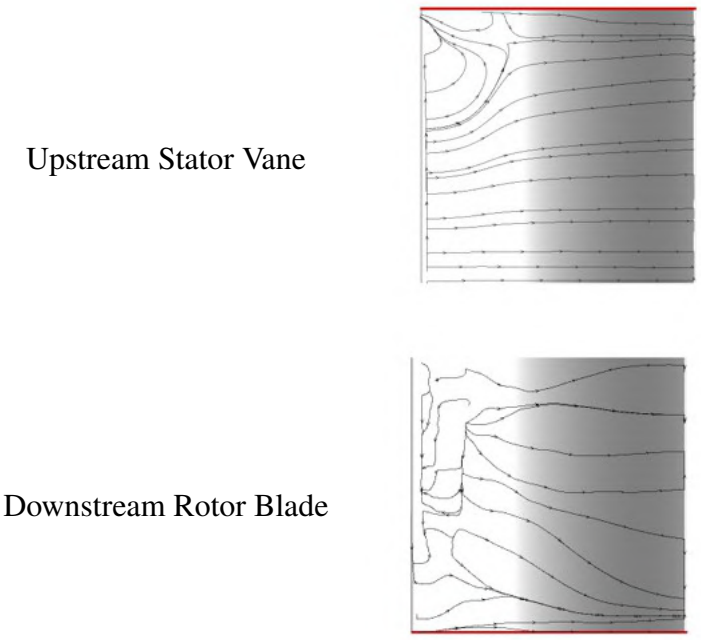

Figure 3.15: Skin-friction lines on pressure surfaces for 50% reaction stage. Endwall marked by red line (time-averaged flow).

Iso-contours of the axial skin-friction coefficient with skin-friction lines as well as iso-surfaces of Q flooded by the axial vorticity for the bar wake generator cases are displayed in Fig. 3.17. Unlike for the 50% reaction stage, a PV is visible for the small bar wake generator. The PV leads to a deflection of the endwall skin-friction lines. For the large bar wake generator, the PV is missing.

Iso-surfaces of Q flooded by the axial vorticity for the suction surface and skin-friction lines for the suction and pressure surface are provided in Fig. 3.18 for both bar wake generators. The laminar separation from the suction surface is entirely suppressed for both cylinders. For the larger cylinder, the suction side corner separation is weakened considerably and an incipient separation from the pressure side near the leading edge is visible. Similar iso-contours to those provided for the 50% reaction stage in Fig. 3.14, were also created for both bar wake generators and are shown in Fig. 3.18. The smaller bar wake generator facilitates an intermittent suppression of laminar separation from the suction surface. The larger bar wake generator suppresses laminar separation over the entire wake passing period. Iso-contours of the flow angle in Fig. 3.20 provide no evidence for a noticeable pressure side separation as a result of the wake velocity deficit.

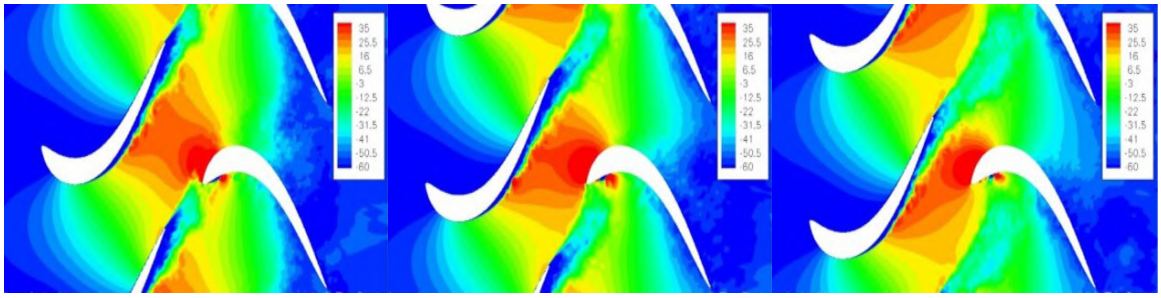

t/T=1/5 t/T=2/5 t/T=3/5

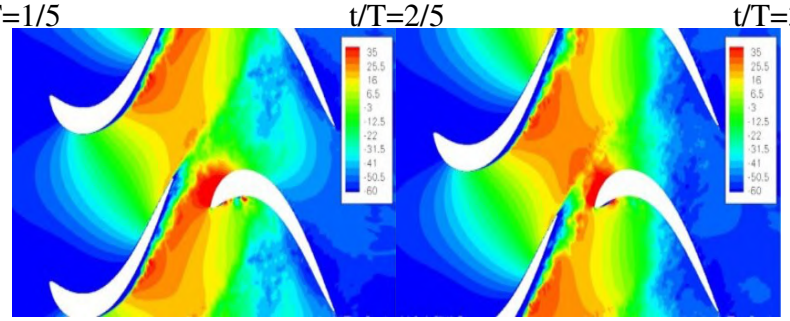

t/T=4/5 t/T=5/5

Figure 3.16: Iso-contours of flow angle at $z = 1$ for 50% reaction stage (phase-averaged flow).

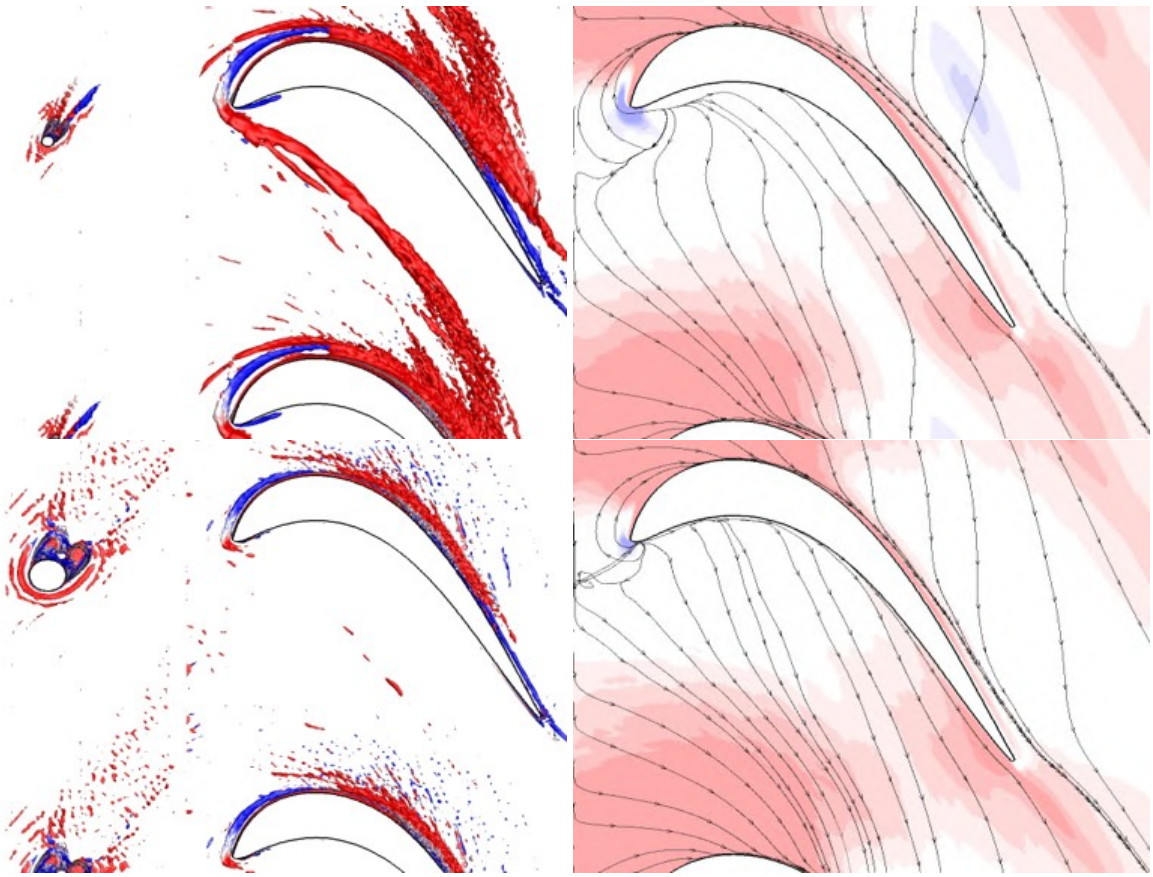

Figure 3.17: Iso-surfaces of $Q = 25$ flooded by $-5 < w_x < 5$ (left) and skin-friction lines and iso-contours of $-0.01 < c_{f,x} < 0.01$ (right) for small bar wake generator (top) and large bar wake generator (bottom) (time-averaged flow).

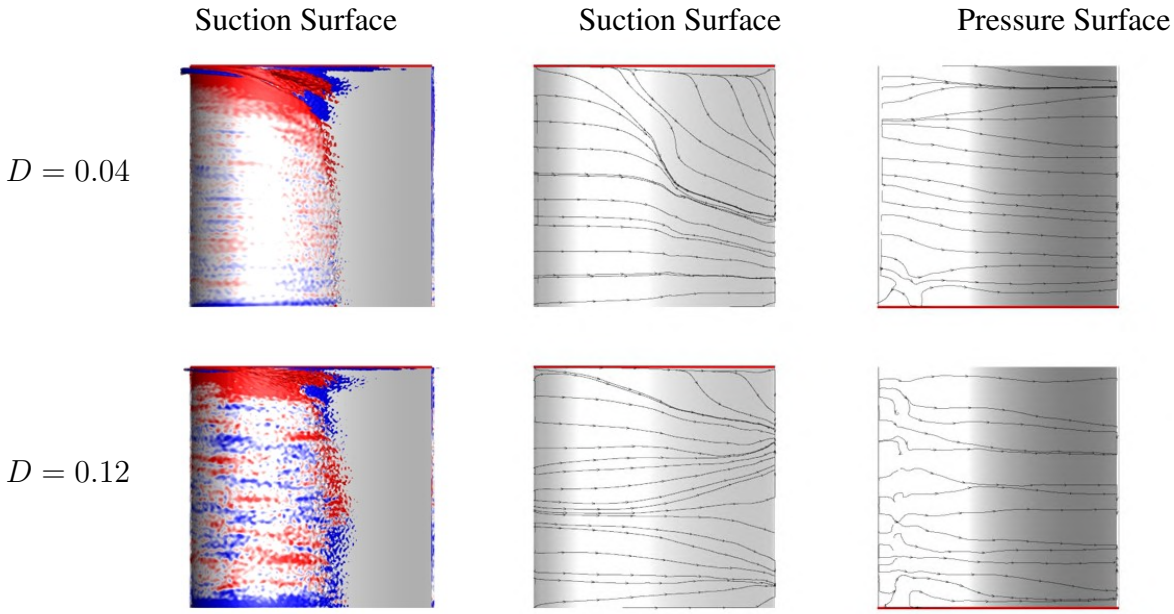

Figure 3.18: Iso-surfaces of $Q = 25$ flooded by $-5 < w_x < 5$ (left) and skin-friction lines for bar wake generators. Endwall marked by red line (time-averaged flow).

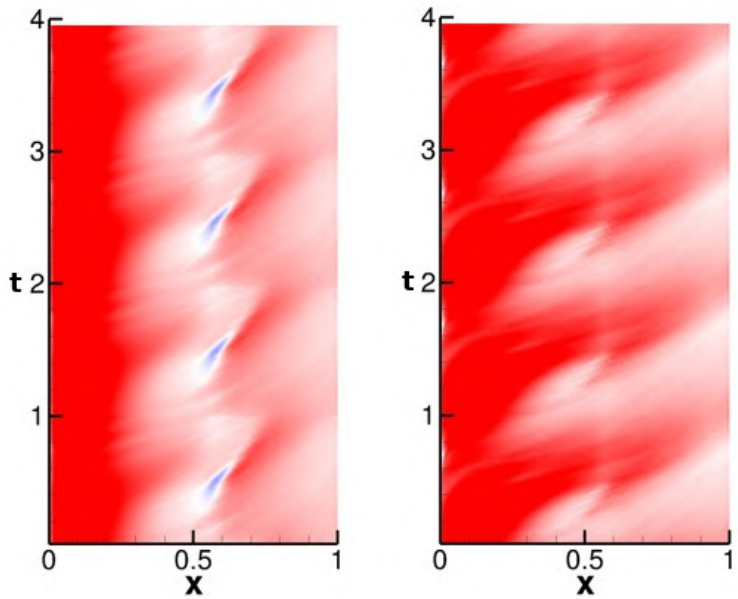

$D = 0.04$ $D = 0.12$

Figure 3.19: Iso-contours of $-0.01 < c_{f,x} < 0.01$ for suction surface of downstream blade averaged over $0.60 < z < 1$ (phase-averages).

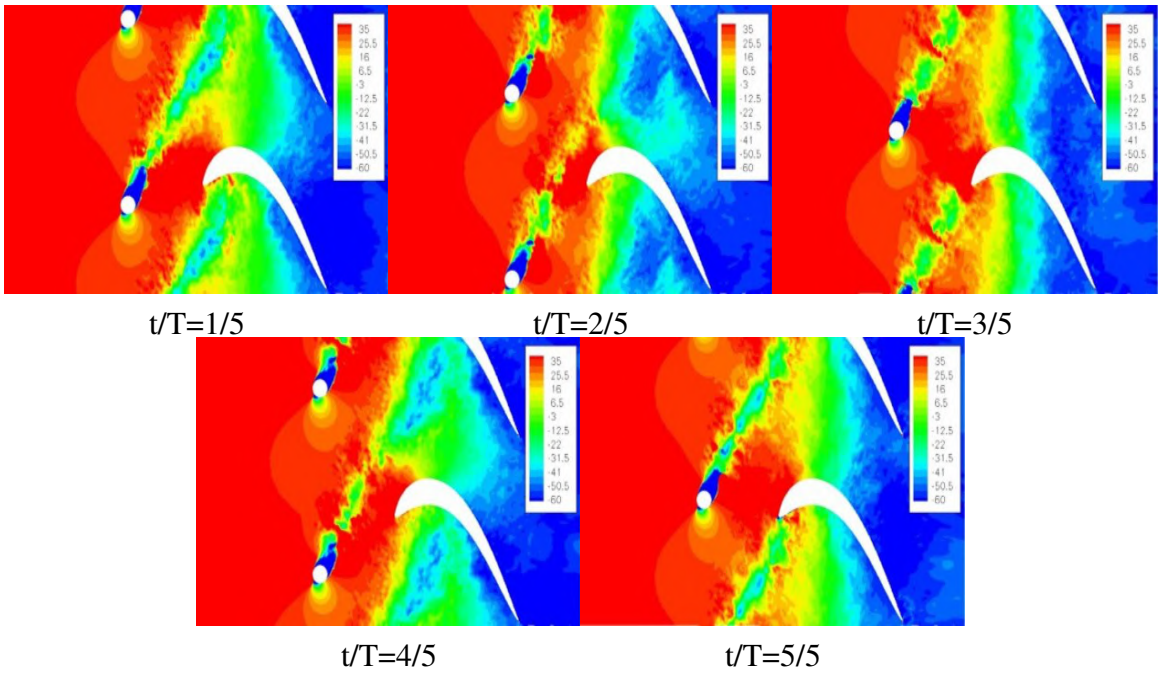

Figure 3.20: Iso-contours of flow angle at $z = 1$ for large bar wake generator (phase-averaged flow).

The mass-averaged total pressure loss coefficient was computed as

$$Y_{tot} = c''_{p,0,in} - c''_{p,0,out}. \tag{3.3}$$

Here, the mass-averaged total pressure coefficient is defined as

$$c''_{p,0} = \frac{1}{\dot{m}} \int_H \int_S \rho \nu_n c_{p,0} dy dz \tag{3.4}$$

with total pressure loss coefficient,

$$c_{p,0} = \frac{p_0 - p_{0,in}}{q_{in}}. \tag{3.5}$$

Table 3.2 provides the mass-averaged total pressure loss coefficients as well as a summary of the observed wake effects. For all three cases, suppression of 2-D separation leads to a dramatic reduction of the total pressure losses. This is important because an isolation of the loss mechanisms is desirable.

	Laminar Separation Suction Surface	Passage Vortex	Laminar Separation Pressure Surface	Y_{tot}
Reference (Upstream L2F)	x	x		0.223
Upstream L2F			x	0.105
Small Cylinder, $D = 0.04$		x		0.155
Large Cylinder, $D = 0.12$			x	0.0303

Table 3.2: Observed wake effect on downstream L2F and total pressure loss coefficient.

3.4 Proper Orthogonal Decomposition of Phase-Averaged Flow

The proper orthogonal decomposition (POD) [61, 62] was utilized as a filter to remove high-frequency "noise" and thus improve the quality of the phase-averaged data. Towards that end, the phase-averaged flow field was reconstructed from the leading POD modes. For all cases only the downstream stationary blocks 1, 6, 7, and 8 were processed. The eigenvalues, λ_i, and time coefficients, a_i, for the 50% reaction stage are provided in Fig. 3.21. The mode magnitude is identical to twice the kinetic energy content. Many of the modes appear in pairs that capture traveling waves. Table 3.3 displays which modes were retained and their relative energy content for the flow field reconstructions for the 50% reaction stage.

Reconstructions of the phase-averaged flow field using 5, 10, and 15 POD modes are shown in Fig. 3.22. For all reconstructions, the endwall structures are revealed with much greater clarity compared to the visualizations for the raw phase-averaged data (see Fig. 3.6). When less modes

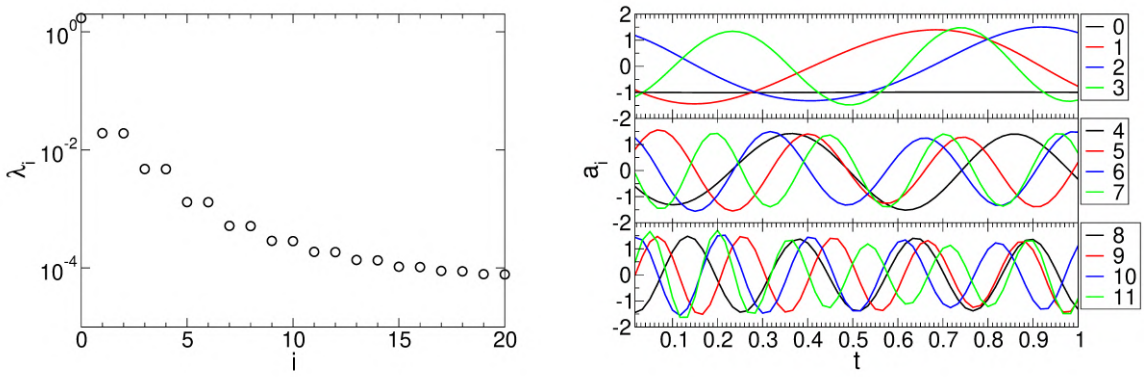

Figure 3.21: POD eigenvalues and time-coefficients for 50% reaction stage.

Modes retained	% total energy	% kinetic energy (0 mode omitted)
5	99.61%	87.47%
10	99.83%	94.65%
15	99.89%	96.36%

Table 3.3: Modes retained for reconstruction and their respective cumulative energy content for 50% reaction stage.

are used for the reconstruction, the endwall structures become more distinct and the wake becomes less pronounced. For instance, for the 5 mode reconstruction the HV region is visible and a small transient separation from the pressure side can be observed near the leading edge. For all reconstructions, crossflow vortices are observed in the passage. Since the reconstruction with 15 modes reveals endwall structures but retains some portion of the wake, this reconstruction was used to further investigate the unsteady wake effect. Iso-surfaces of Q flooded by the endwall distance for the 15 mode reconstruction with more temporal resolution are provided in Fig. 3.23. Towards the end of the period at $t/T = 14/15$, part of the wake develops into a longitudinal structure that moves towards the pressure surface. The structure appears most coherent at $t/T = 4/15$. As time progresses, this structure is then convected downstream.

Iso-surfaces of Q flooded by the axial vorticity in Fig. 3.24 reveal a strengthening and movement of the shed vortex (see $t/T = 15/15$) towards the wall. The shed vortex is "shadowed" by another vortex closer to the wall. In the sequence provided in Fig. 3.25, the two vortices are seen to combine into a longitudinal trailing edge structure.

Iso-surfaces of Q flooded by the axial vorticity are also provided for the suction and pressure surface in Fig. 3.26. The corner separation is "robust" and not affected much by the PV. The PV sense of rotation opposes the secondary flow which leads to a dissipation of the PV. The flow visualizations in Fig. 3.26 also illustrate the laminar separation from the pressure surface.

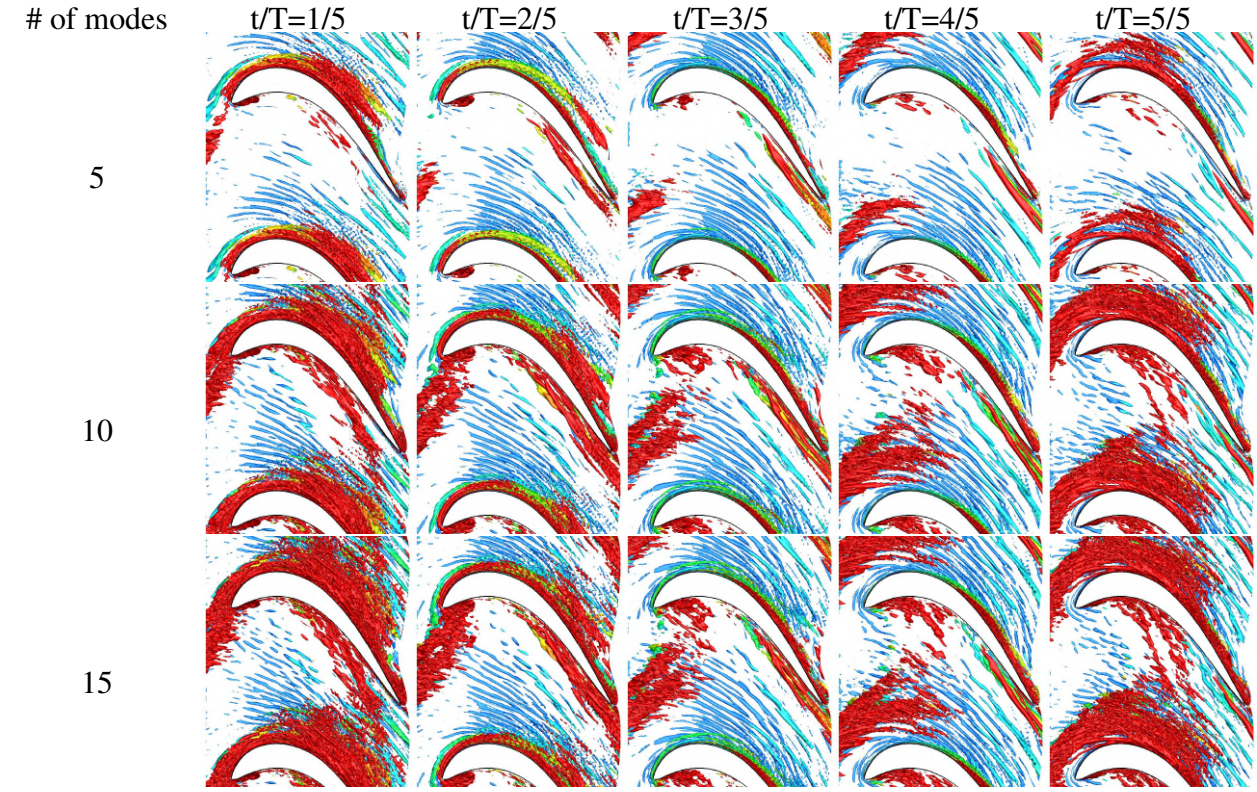

Figure 3.22: Reconstructions of phase-averaged flow for 50% reaction stage. Iso-surfaces of $Q = 25$ flooded by wall distance ($z > 0.02$ is red).

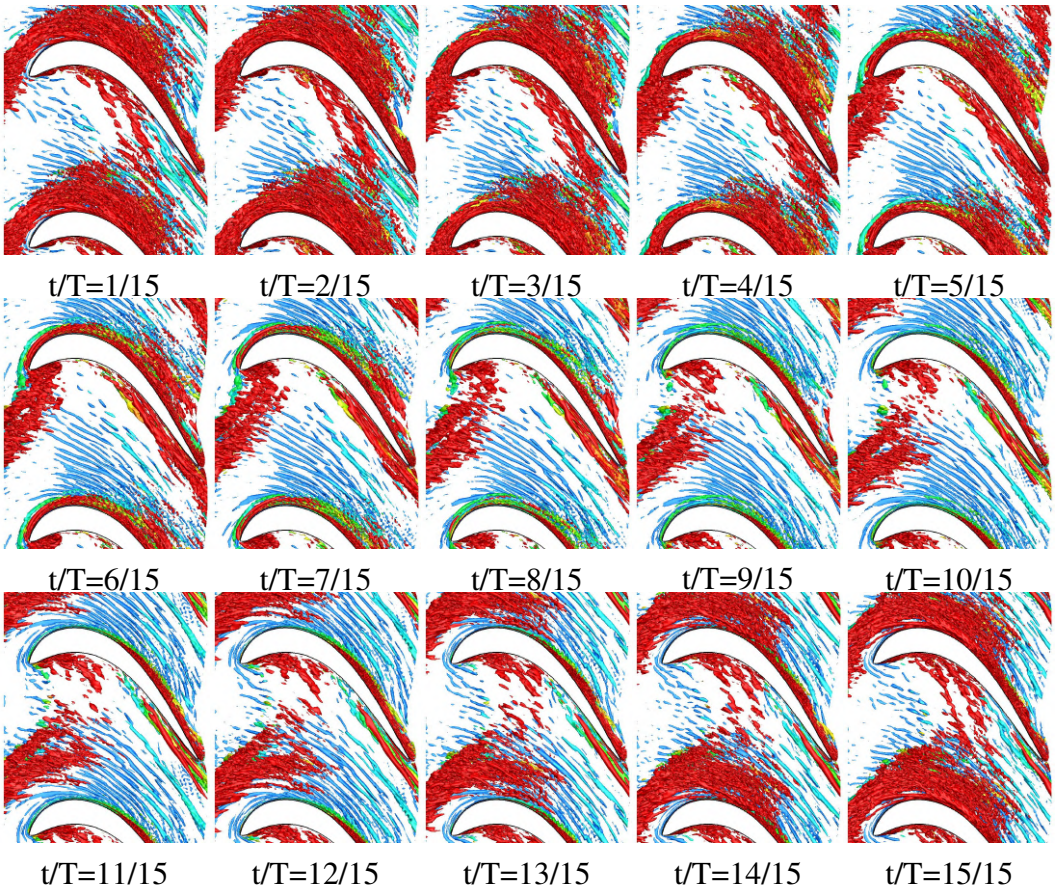

Figure 3.23: Iso-surfaces of $Q = 25$ flooded by wall distance ($z > 0.02$ is red) for 50% reaction stage (phase-averaged flow). POD reconstructions with 15 modes.

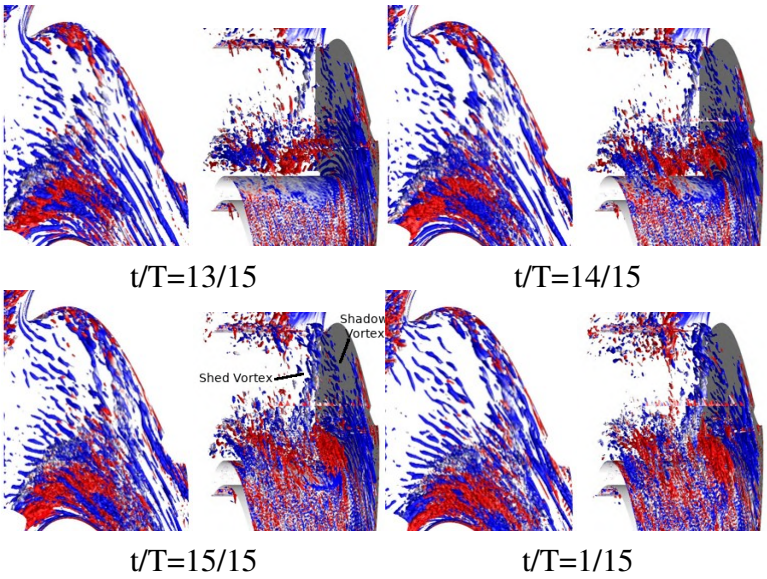

Figure 3.24: Iso-surfaces of $Q = 20$ flooded by $-5 < w_x < 5$ for 50% reaction stage (phase-averaged flow). POD reconstructions with 15 modes.

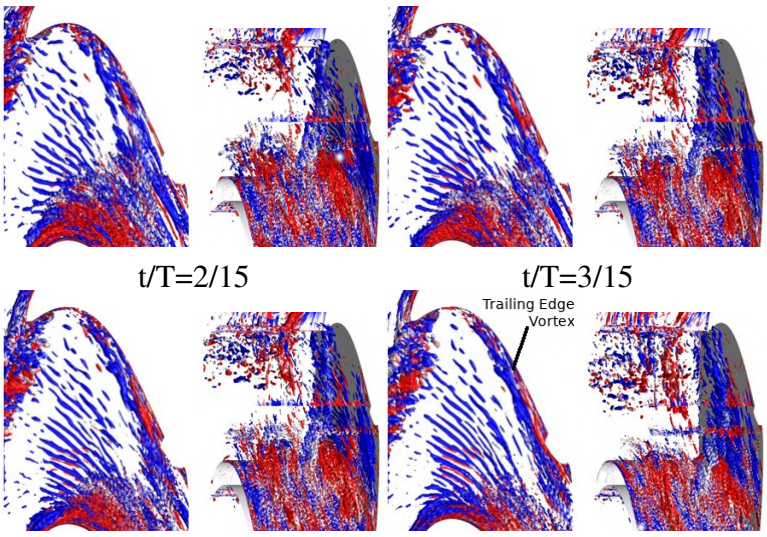

Figure 3.25: Iso-surfaces of $Q = 20$ flooded by $-5 < w_x < 5$ for 50% reaction stage (phase-averaged flow). POD reconstructions with 15 mode.

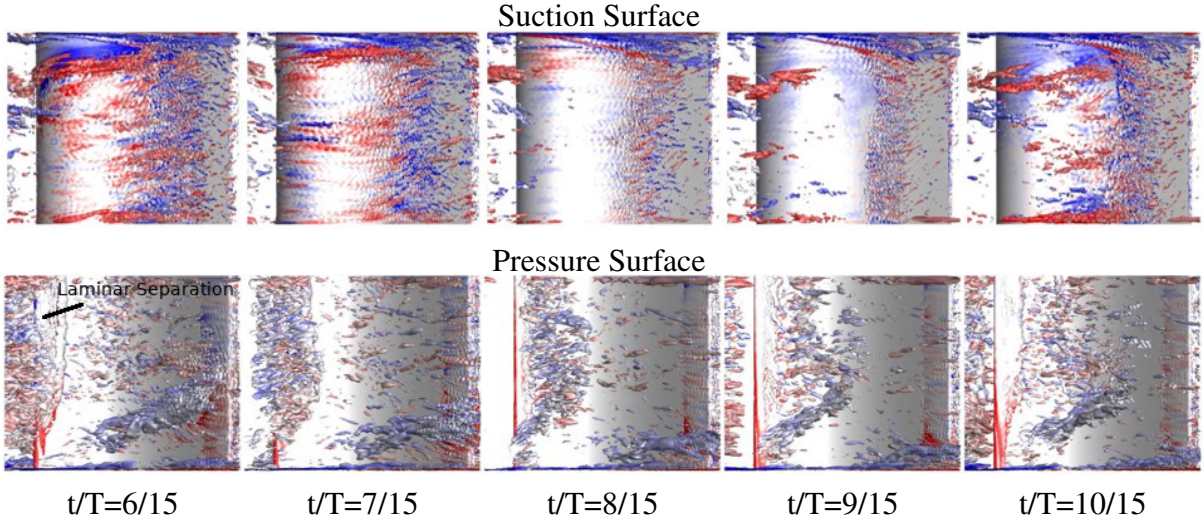

Figure 3.26: Iso-surfaces of $Q = 10$ flooded by $z - 20 < w_x < 20$ for 50% reaction stage (phase-averaged flow). POD reconstructions with 15 modes.

The bar wake generator cases were also analyzed with the POD. Eigenvalues and time coefficients for both cases are provided in Figs. 3.27 and 3.28. Similar to the 50% reaction stage, the modes appear in pairs and capture traveling waves. The modes retained for the reconstruction and their relative energy content are provided in Tab. 3.4. More energy is retained for the large cylinder case.

Iso-surfaces of Q for the small and large bar wake generator flow field reconstructions are provided in Figs. 3.29 and 3.30 respectively. For the chosen contour level, the wakes are not visible for the smaller cylinder due to the low amount of kinetic energy contained in the wake. The PV is however clearly visible. For the larger cylinder, the exclusion of the high-frequency low-energy modes from the reconstruction makes the wake appear more narrow. Over the course of one wake passing period, the PV is intermittently suppressed. Additionally, evidence of a weak longitudinal trailing edge structure is present.

This structure was further investigated based on the flow visualizations in Fig. 3.31. From these images, it can be concluded that the longitudinal structure is too close to the wall to be of the same origin as for the 50% reaction stage. It is possible that the longitudinal structure is the same as the bar wake generator induced vortex proposed by Ciorciari et al [37].

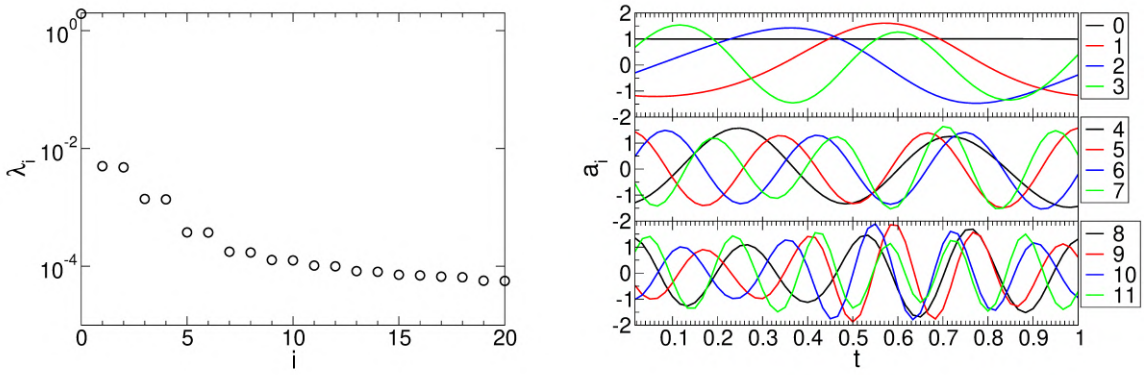

Figure 3.27: POD eigenvalues and time-coefficients for bar wake generator with $D = 0.04$.

	$D = 0.04$		$D = 0.12$	
Modes retained	% total energy	% kinetic energy (0 mode omitted)	% total energy	% kinetic energy (0 mode omitted)
5	99.39%	79.22%	99.83%	82.98%
10	99.61%	86.96%	99.89%	88.99%
15	99.71%	90.06%	99.91%	91.84%

Table 3.4: Modes retained for reconstruction and their respective cumulative energy content for bar wake generators.

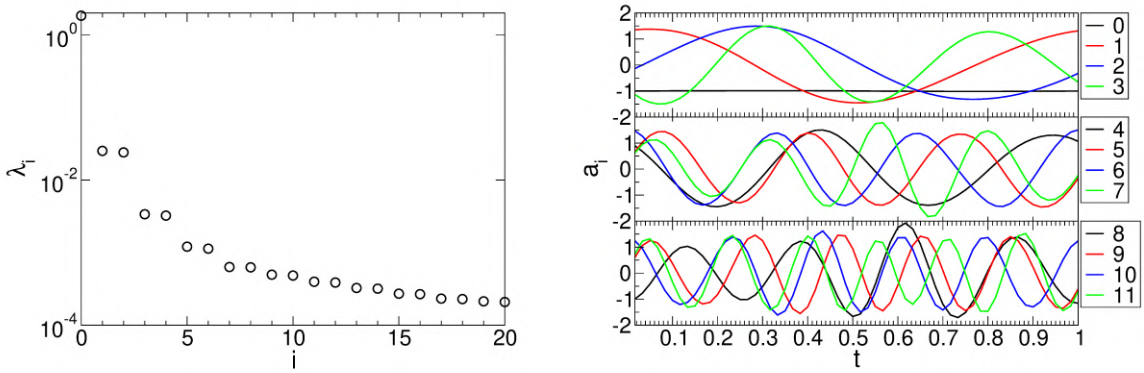

Figure 3.28: POD eigenvalues and time-coefficients for bar wake generator with $D = 0.12$.

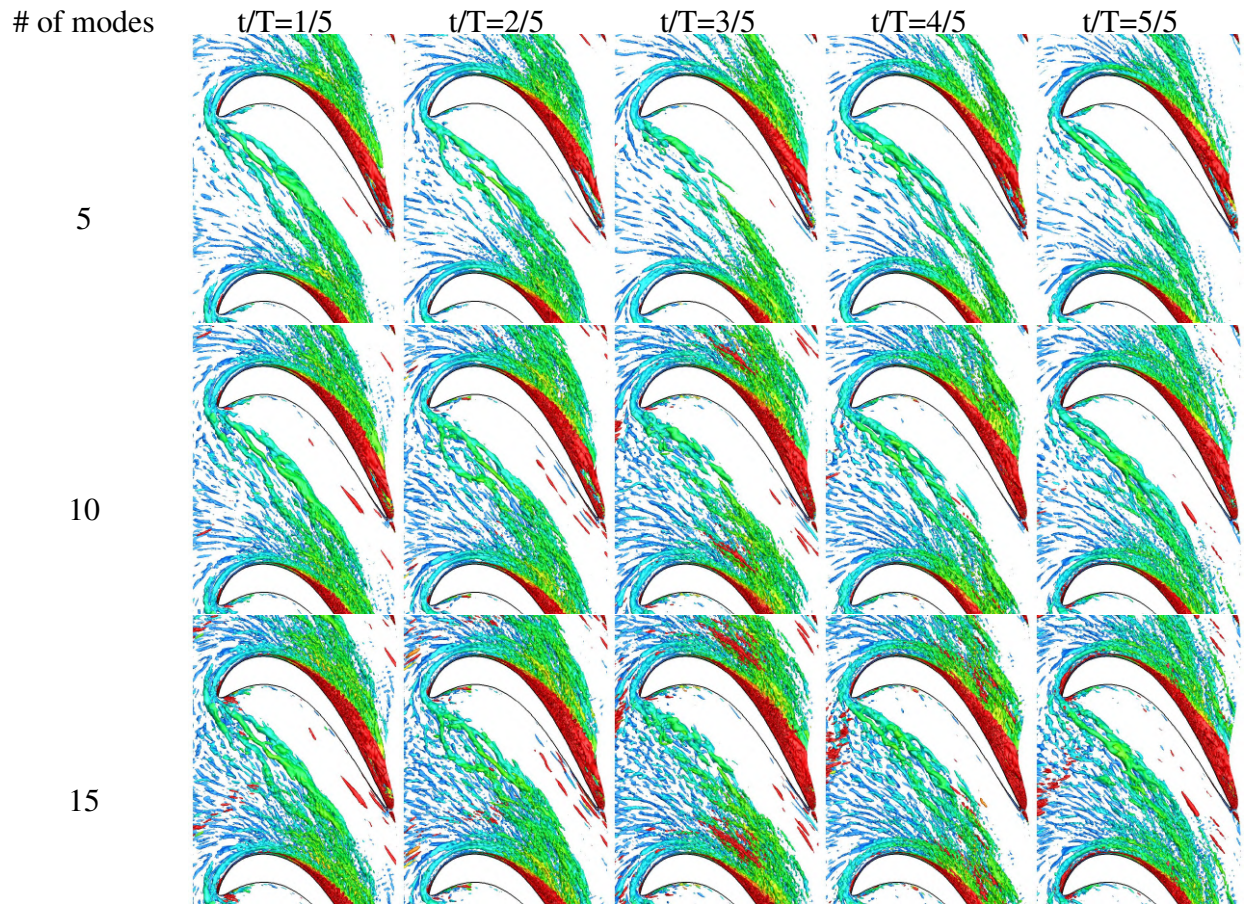

Figure 3.29: Reconstructions of phase-averaged flow for small bar wake generator. Iso-surfaces of $Q = 25$ flooded by wall distance ($z > 0.02$ is red).

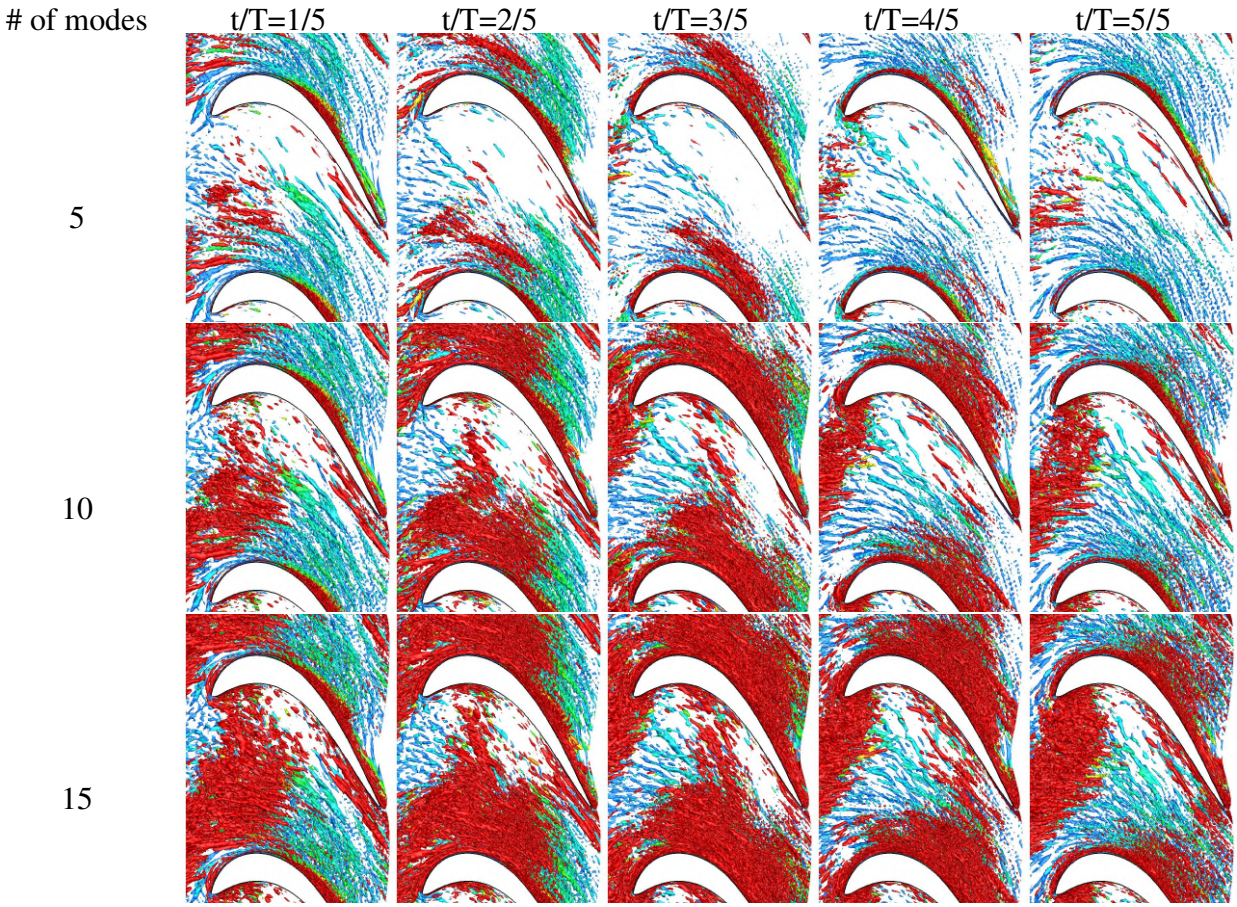

Figure 3.30: Reconstructions of phase-averaged flow for large bar wake generator. Iso-surfaces of $Q = 25$ flooded by wall distance ($z > 0.02$ is red).

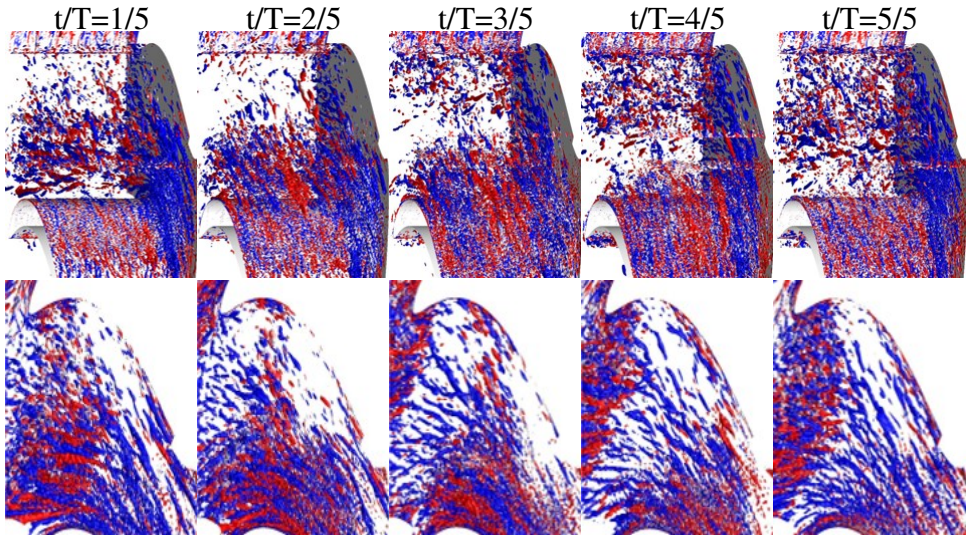

Figure 3.31: Iso-surfaces of $Q = 25$ flooded by wall distance ($z > 0.02$ is red) for large bar wake generator (phase-averaged flow). POD reconstructions from 15 modes.

4 Results for Re=100,000

4.1 Approach Flow Analysis

The turbulent approach endwall boundary layer was computed first and the integral boundary layer properties near the outflow were matched to corresponding AFRL wind tunnel measurements [8]. Instantaneous iso-surfaces of the Q-criterion flooded by the streamwise velocity for the approach flow endwall boundary layer are provided in Fig. 4.1. The iso-surfaces reveal that the boundary layer becomes fully turbulent downstream of the inflow boundary and then grows in the streamwise direction.

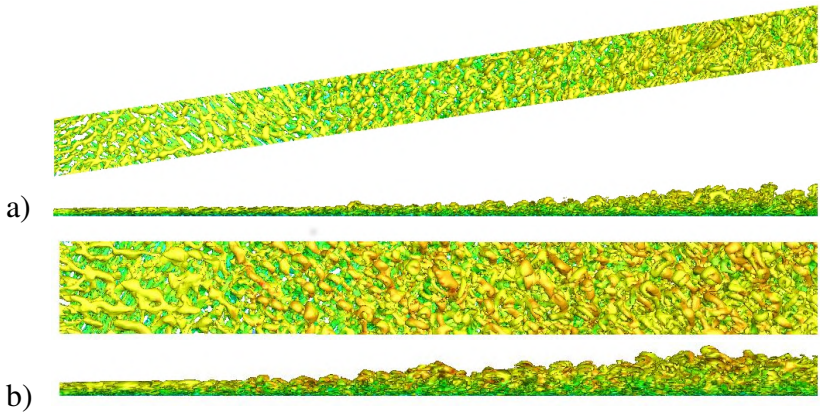

Figure 4.1: Iso-surfaces of $Q = 0.5$ flooded by streamwise velocity for a) full stage and b) linear cascade with bar wake generators.

The displacement thickness, δ^*, momentum thickness, ϑ, and shape factor, H, are plotted in Fig. 4.2a. Dashed lines represent linear extrapolations of the simulation data. For the 50% reaction stage simulation, experimental measurements at AFRL [8] $1.5C_{ax}$ upstream of the leading edge are approximately matched (gray dots in Fig. 4.2a). The bar wake generator simulation was set up such that the displacement and momentum thickness at the rotor blade leading edge ($x = 0$) were similar to those of the 50% stage simulation. The shape factor for the present simulation approaches 1.4, indicating that the BL is fully turbulent.

In Fig. 4.2b, boundary layer profiles in wall units at $x = -2.5$ (50% reaction stage) and -1.7 (bar wake generator) are plotted against the relationships for the viscous sublayer and the logarithmic layer (law of the wall). The log layer slope is matched. The intercept with the relationship for the viscous sub-layer is slightly too high which generally indicates that the grid resolution is marginal.

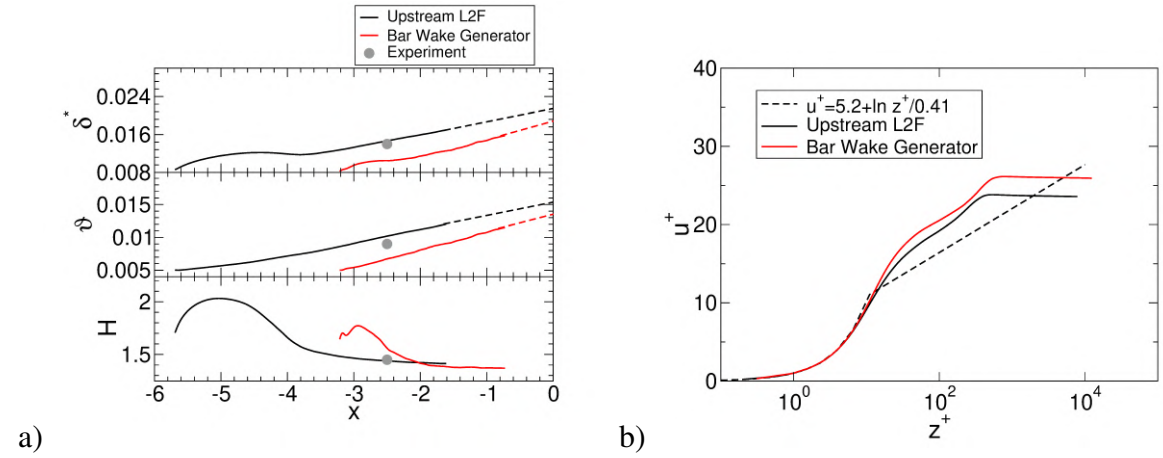

a) b)

Figure 4.2: a) Approach endwall boundary layer displacement and momentum thickness as well as shape factor and b) velocity profiles in wall units.

4.2 Wake Characterization

The time-averaged wake flows for the upstream stator vane and bar wake generator are compared first (Fig. 2.1 & 2.2). For both cases, the nominal freestream axial velocity is 0.819. Iso-contours of the axial velocity and axial vorticity,

$$\omega_x = \frac{\partial w}{\partial y} - \frac{\partial v}{\partial z}, \tag{4.1}$$

for two planes upstream of the rotor leading edge are provided in Fig. 4.3. The wake shed by the upstream L2F has strong three-dimensional (3-D) components near the endwall that originate from the stator vane passage vortex (PV) and shed vortex (SV) (Fig. 4.3a). As a result, the wake u-velocity distribution is strongly 3-D. For the case with upstream bar wake generator (Fig. 4.3b), the wake is almost 2-D and growing in width in the streamwise direction. Different from the case with upstream L2F, pronounced well-defined endwall structures are missing.

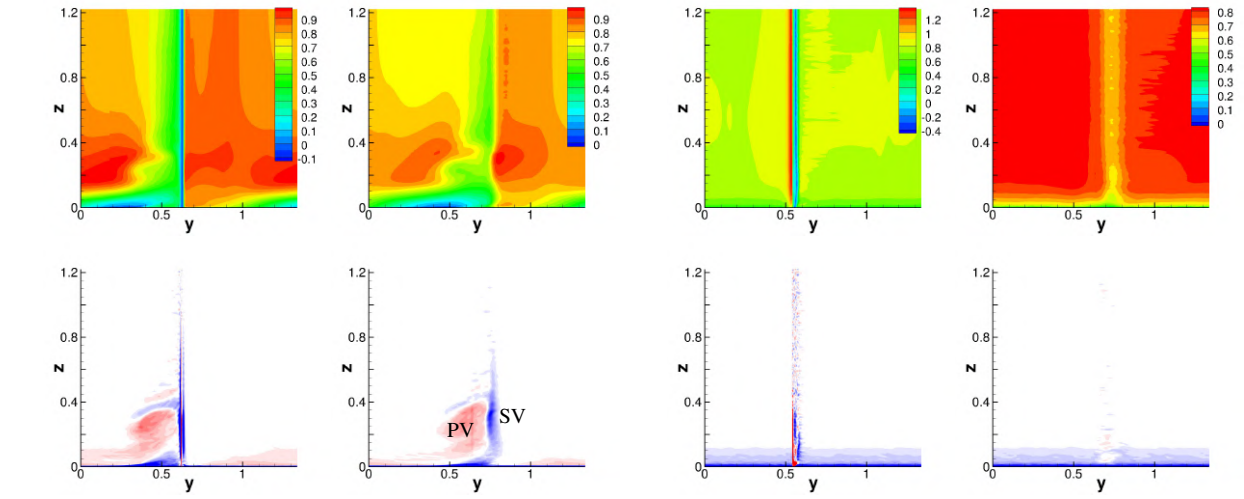

Figure 4.3: Iso-contours of axial velocity (u, top images) and axial vorticity ($-5 < \omega_x < 5$, bottom images) for constant axial planes. a) 50% reaction stage and b) bar wake generator.

In Fig. 4.4 the streamwise velocity, $u_{60} = u\cos(60deg) + v\sin(60deg)$, at $x = -0.15$, integrated from $z = 0.12$ to $z = 1.97$, is plotted versus the pitchwise coordinate. The L2F wake is slightly narrower and the wake velocity deficit is larger compared to the bar wake generator case. Pitchwise averaged profiles of $u_{-35} = u\cos(-35deg) + v\sin(-35deg)$ for $x = -1.45$ and u_{60} for $x = -0.15$ are provided in Fig. 4.5. The profile for the bar wake generator resembles a boundary layer profile. For the L2F, the average profile displays a noticeable near-wall distortion as a result of the strong endwall structures.

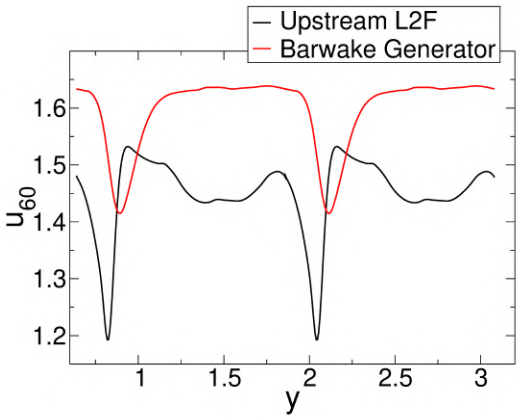

Figure 4.4: Wake velocity at $x = -0.15$. Spanwise averages over $0.12 \leq z \leq 1.97$ versus pitchwise coordinate.

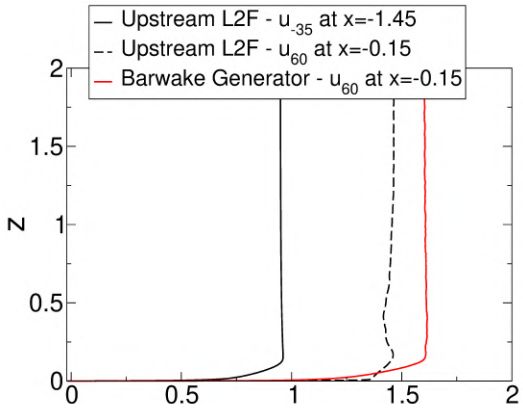

Figure 4.5: Velocity profiles at $x = -1.45$ and $x = -0.15$. Pitchwise averages versus spanwise coordinate.

The integral wake momentum deficit,

$$\vartheta = \frac{1}{(z_2 - z_1)S} \int_{z_1}^{z_2} \int_S \frac{u_{60}}{U_{60}} \left(1 - \frac{u_{60}}{U_{60}}\right) dA\,, \tag{4.2}$$

was computed by integration over the spanwise interval $z_1 < z < z_2$ and the blade pitch, S. The symbol U_{60} refers to the wake freestream velocity. Integration over the range $0.12 < z < 1.97$ provides a quasi 2-D wake momentum deficit. The 3-D wake momentum deficit was computed by integration over the entire span ($z_1 = 0$ to $z_2 = H$). The 2-D wake momentum deficit for the two cases is similar (Tab. 4.1). However, the 3-D momentum deficit for the 50% reaction stage is about twice as large as for the bar wake generator case.

	2-D $0.12 < z < 1.97$	3-D $0 < z < 2$
Upstream L2F	0.0502	0.0540
Bar Wake Generator	0.0488	0.0225

Table 4.1: Two- and three-dimensional wake momentum deficit for $x = -0.15$.

It took considerable effort to achieve such a close agreement of the profiles (Fig. 4.4) and 2-D wake momentum deficit (Fig. 4.1) at $x = -0.15$. Considering the large computational expense of the simulations and the nonlinear dependence of the wake flow on the free parameters (length of inflow domain, bar wake generator diameter, etc.), the match was considered close enough for a fair comparison of the wake effect on the flow through the rotor.

4.3 Rotor Mean Flow

Visualizations of the time-averaged flow through the rotor passage for both cases are displayed in Figs. 4.6 and 4.7. For the 50% reaction stage, the stator flow field is shown for reference and is characterized by the presence of a weak PV. For the rotor, the PV and corner separation are

suppressed. For the bar wake generator, a pronounced PV, corner separation (CS), and shed vortex (SV) (red structure in Figs. 4.6 and 4.7) are visible. The PV develops from the pressure side leg of the horseshoe vortex (HV) and is stronger and more coherent than the PV for the stator for the 50% reaction stage. This can be attributed to the thicker rotor endwall boundary layer compared to the stator. For the reaction stage rotor, evidence of endwall cross-flow vortices is present. This phenomenon was discussed by Gross et al. [63].

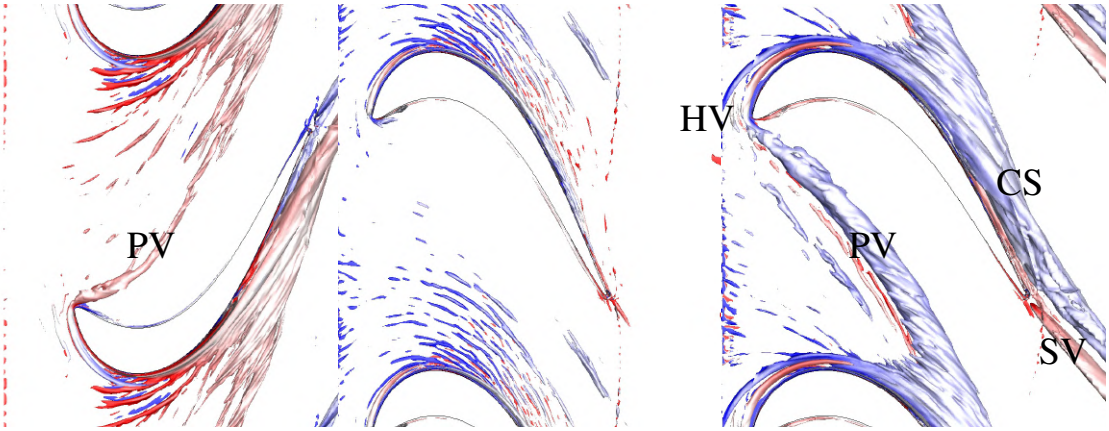

50% Reaction Stage Stator | 50% Reaction Stage Rotor | Bar Wake Generator Rotor

Figure 4.6: Iso-surfaces of $Q = 15$ flooded by $-25 < \omega_x < 25$ (time averages).

Figure 4.7 shows the rotor trailing-edge region from a different observer point. For the bar wake generator case, the PV and corner separation (blue structures in Fig. 4.7) are substantial and the SV (red structure in Fig. 4.7) is distinct.

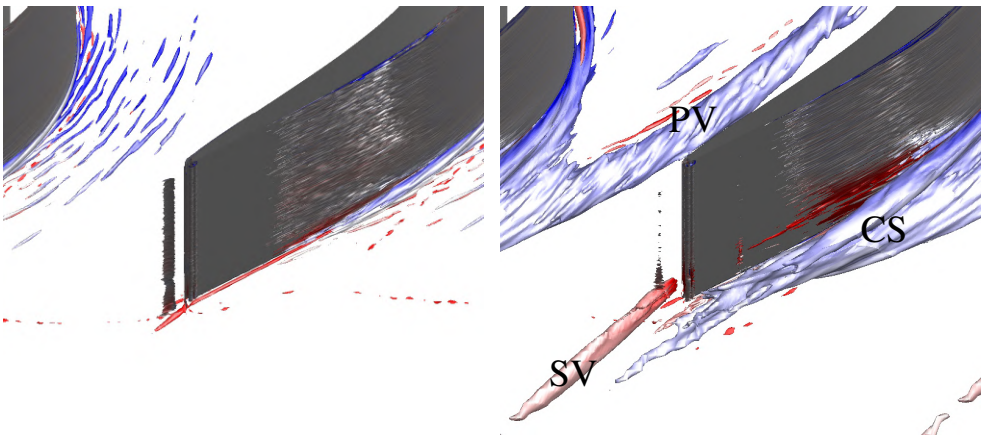

50% Reaction Stage - Rotor | Bar Wake Generator

Figure 4.7: Iso-surfaces of $Q = 25$ flooded by $-25 < \omega_x < 25$ (time averages). View towards trailing edge of rotor blades.

To further quantify the wake effect on the endwall structures, skin-friction lines and iso-contours of the axial skin-friction coefficient, $c_{f,x} = 2(\partial u/\partial z)_w/Re$ are plotted in Fig. 4.8. Although Fig.

4.6 suggests that the HV is not affected much by the passing wakes, Fig. 4.8 suggests that the HV is considerably stronger for the case with bar wake generator. The visualizations also provide further evidence that the PV is suppressed for the case with upstream L2F. For the bar generator case, the PV induces a negative axial wall shear stress and deflects the skin-friction lines upstream in accordance with the direction of rotation of the PV. For the 50% reaction stage, the near-wall axial velocity remains positive and the skin-friction lines are "straight".

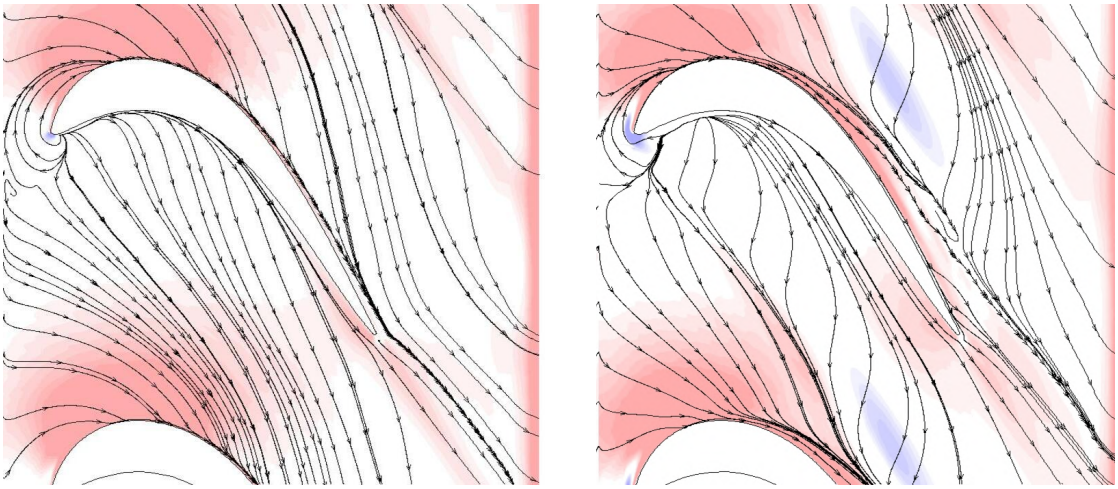

50% Reaction Stage - Rotor Bar Wake Generator

Figure 4.8: Skin-friction lines and iso-contours of axial skin-friction coefficient, $0.005 < c_{f,x} < 0.005$ (time averages).

In a similar manner, the wake effect on the suction and pressure-side mean flow topology was analyzed. In Figs. 4.9 and 4.10, skin-friction lines and iso-contours of the axial and spanwise velocity components for the first cell off the wall are plotted for the suction and pressure-side surface. For the 50% reaction stage, the suction surface 2-D laminar separation is almost entirely suppressed and the corner separation is diminished compared to the other case (smaller region of positive w-velocity near endwall). Regarding the pressure side, a small 2-D laminar separation can be observed near the leading edge. For the case with bar wake generator, the suction surface 2-D laminar separation is entirely suppressed in the mean but the corner separation is very pronounced. The pressure-side leading-edge separation is missing.

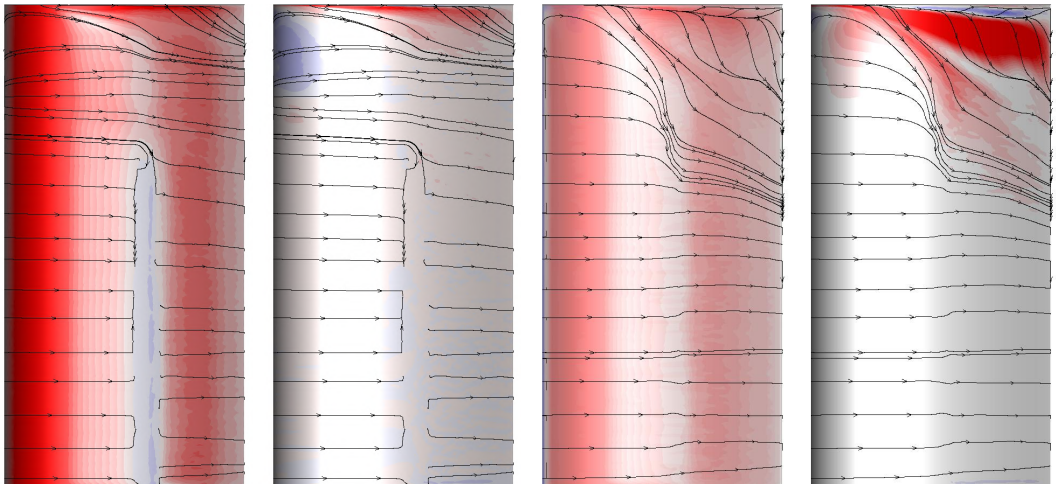

Figure 4.9: Suction-side skin-friction lines and velocity contours (first cell off the wall).

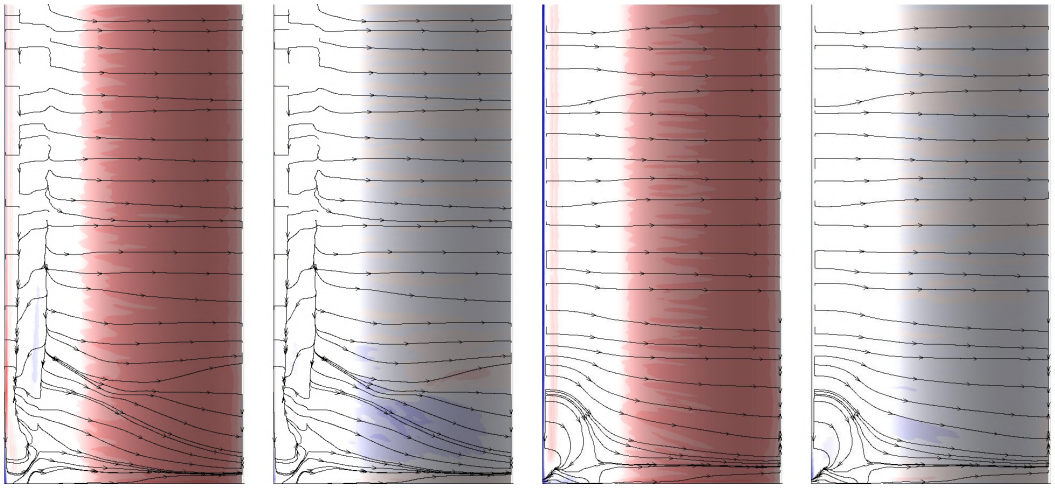

Figure 4.10: Pressure-side skin-friction lines and velocity contours (first cell off the wall).

4.4 Instantaneous Flow Fields

Instantaneous iso-surfaces of the Q-criterion flooded by the wall-normal distance ($z > 0.02$ is red) for both cases are exhibited in Figs. 4.11 & 4.12. The images are for one blade passing period and the downstream rotor blades are seen to move once across the passage. In agreement with the results for Re=50,000, the wakes are stretched and obtain a Λ-shape as they are convected through the rotor passage. For the 50% reaction stage, a PV is observed for the upstream stator vanes. A quiescent laminar region underneath the PV extends from the pressure side of the stator vanes into

the rotor passage. This region can be attributed to the secondary flow which transports freestream fluid towards the endwall. For the bar wake generator case, the quiescent region is missing. This can be explained by the absence of a secondary flow. Different from the 50% reaction stage simulation, a pronounced PV can be observed for the rotor blades. Also, the turbulent wake appears to linger in the vicinity of the suction surface for a larger fraction of the wake passing period.

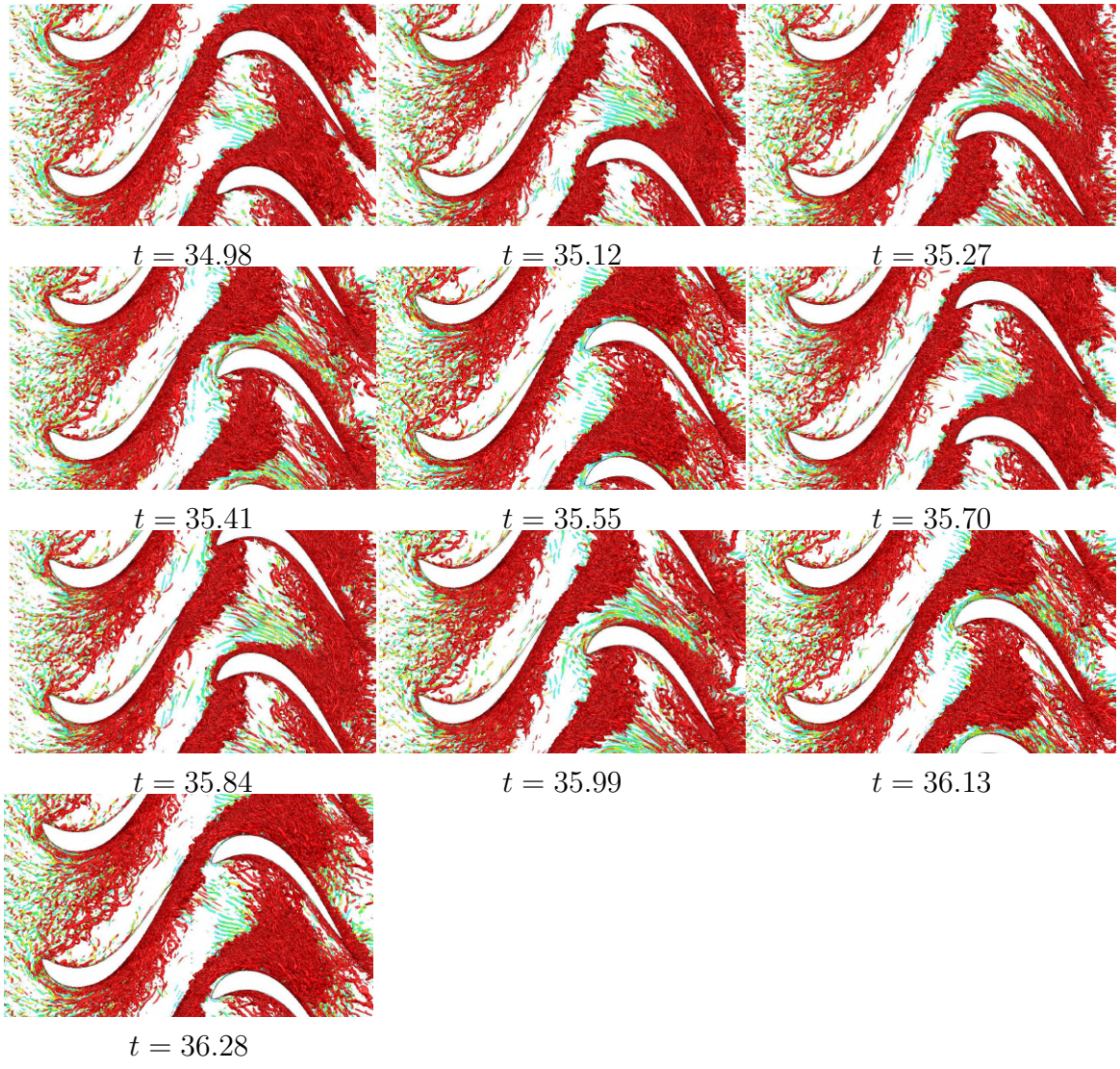

Figure 4.11: Iso-surfaces of $Q = 100$ flooded by $0 < z < 0.02$ for 50% reaction stage.

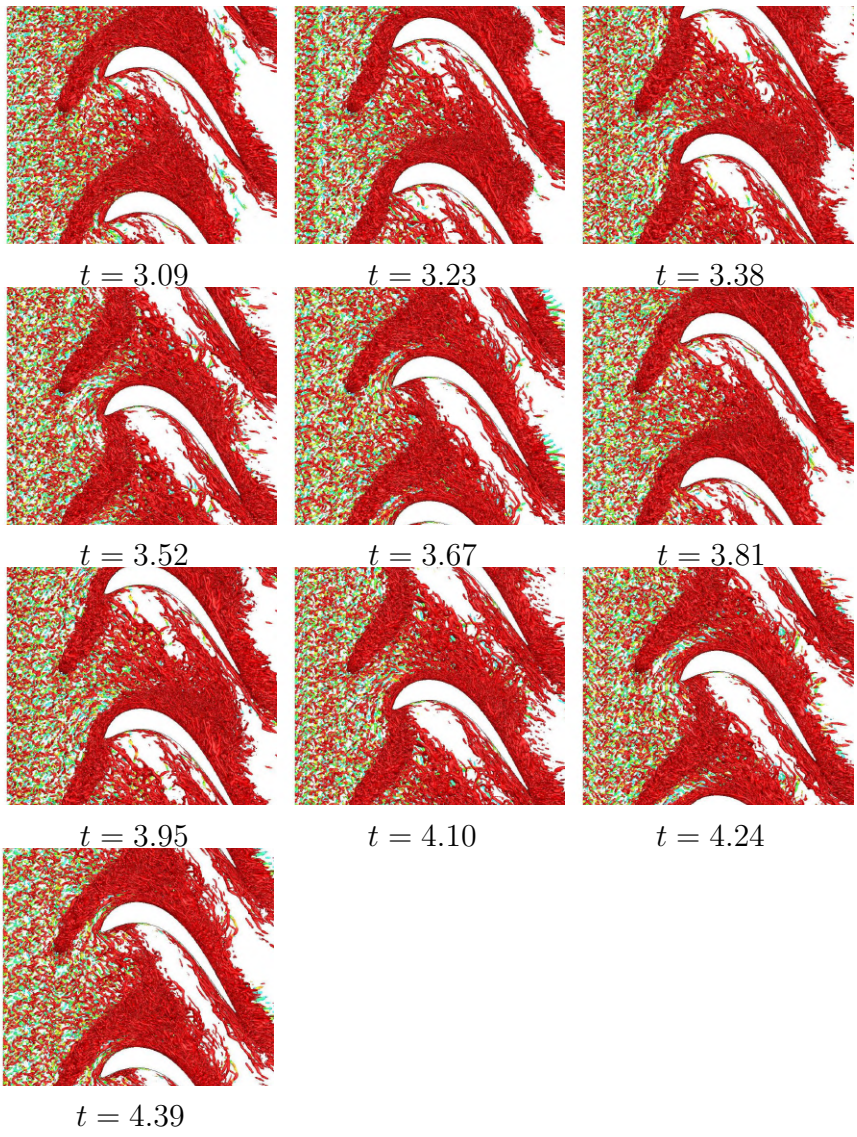

Figure 4.12: Iso-surfaces of $Q = 100$ flooded by $0 < z < 0.02$ for bar wake generator.

To visualize the wake effect on the suction-surface boundary layer, instantaneous Q-criterion iso-surfaces were generated and flooded by the axial vorticity (Figs. 4.13 & 4.14). For the 50% stage (Fig. 4.13), before the wake impacts the rotor blade (e.g., $t = 35.12$), the suction-side boundary layer separates laminar, rolls up into spanwise vortices, transitions, and reattaches turbulent. Around $t = 36.28$, the vortical 3-D wake components strike the suction-side boundary layer near the endwall and around $t = 35.27$, the 2-D wake component impacts the suction-side boundary layer. The wake turbulence by-pass transitions the separated boundary layer (i.e., the spanwise vortices are missing) and suppresses laminar separation. After the wake has passed, the suction side boundary layer relaminarizes and initially remains attached (i.e., "calmed region" according to Stieger and Hodson [28, 29]). Around $t = 36.28$ the laminar separation redevelops from the top and then spreads downward (i.e., $t = 34.98$). The turbulent corner separation near the endwall is strongly reduced by the passing wakes (compared to the bar wake generator case which will be discussed next), likely as

a result of the incoming 3-D wake components. In particular the stator PV has the opposite sense of rotation from the rotor secondary flow which may explain the suppression of the corner separation.

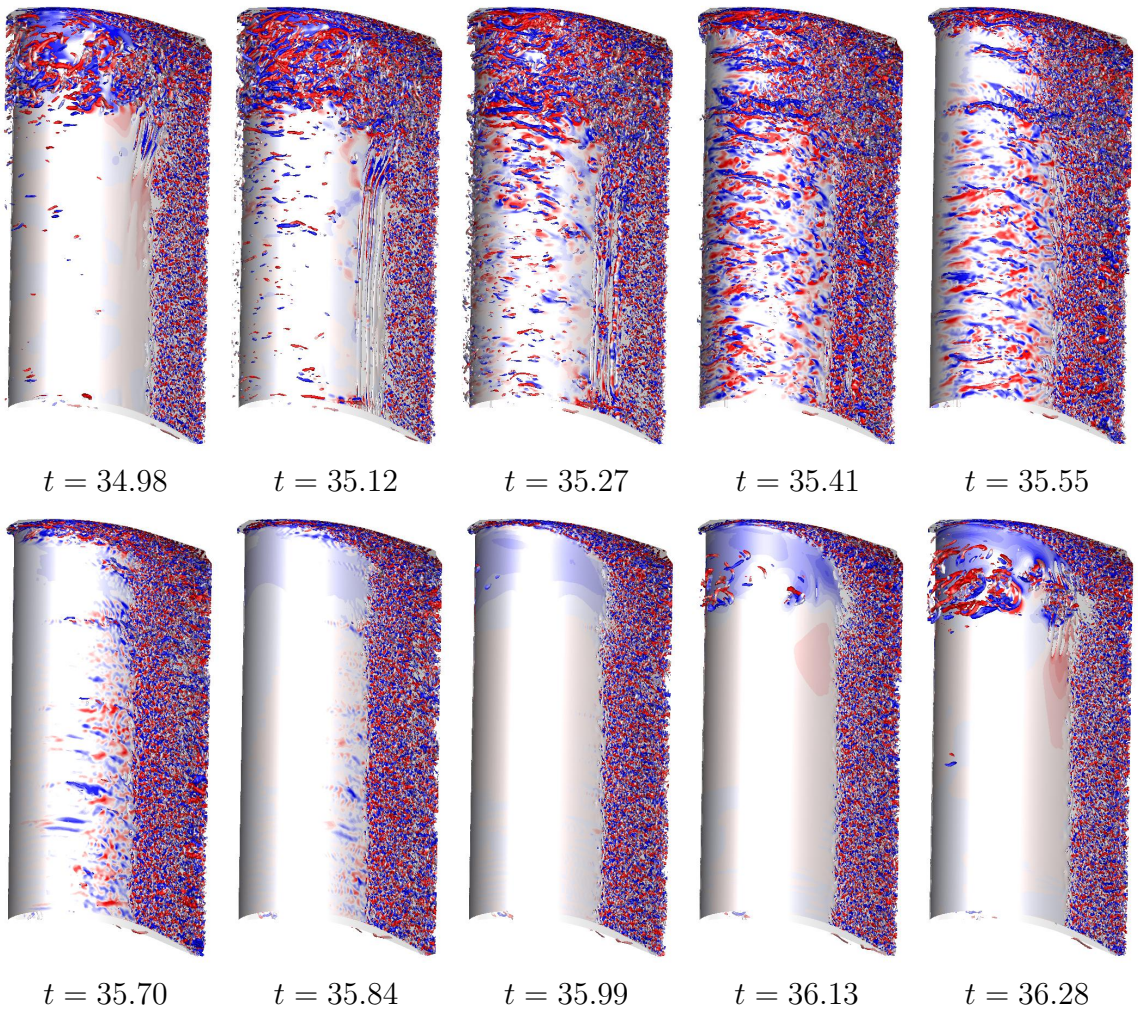

Figure 4.13: Iso-surfaces of $Q = 100$ flooded by $-15 < \omega_x < 15$ for 50% reaction stage.

For the bar wake generator (Fig. 4.14), the 3-D wake components are absent. For none of the time instances shown, 2-D vortex shedding by a laminar separation bubble is observed. The bubble shedding is suppressed by the incoming 2-D wakes, which strike the suction surface at about the same phase as for the 50% stage (i.e., $t = 35.27$) but appear to linger longer over the suction surface as already noted. In particular, the wake effect persists longer. For $t = 4.10$ and 4.24, remnants of the wake turbulence are still causing streaks (likely Klabanoff modes) in the suction side boundary layer. For $t = 4.39$, the flow over the suction surface is entirely laminar but already for $t = 3.09$ the early wake turbulence again impacts the suction side boundary layer. This can be traced back to the overall wider wake compared to the 50% reaction stage as also suggested by Fig. 3.11. Interestingly, the bar wake generator wakes have little effect on the suction side corner separation which has about the same size as when the wakes are missing (e.g., see Ref. [17]). The present results suggest that bar wake generators cannot accurately reproduce the wake effect of high-lift front-loaded LPT

airfoils. More specifically, bar wake generators over-predict the suppression of the 2-D laminar separation and under-predict the suppression of the PV and corner separation.

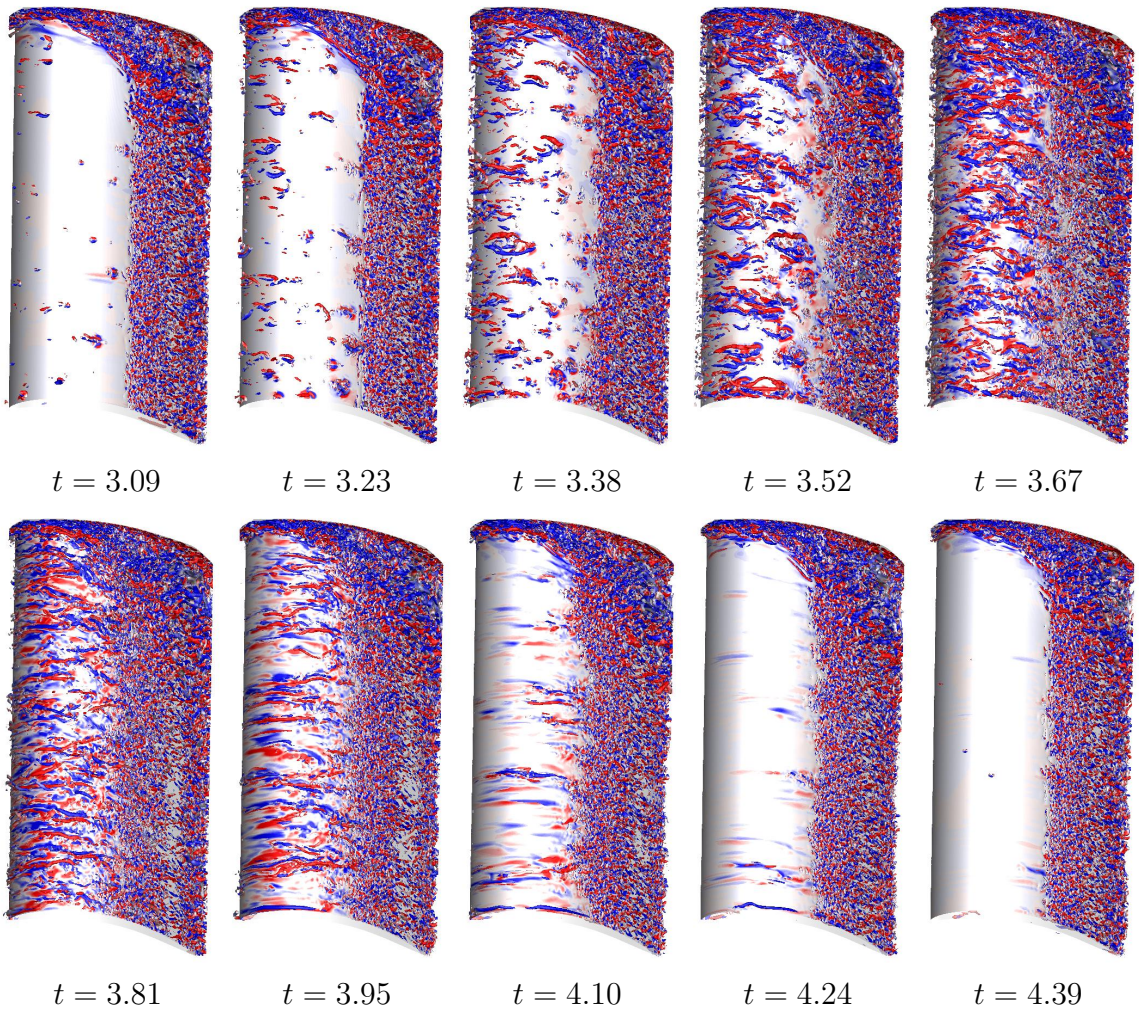

Figure 4.14: Iso-surfaces of $Q = 100$ flooded by $-15 < \omega_x < 15$ for bar wake generator.

4.5 Phase-Averaged Flow

To remove part of the turbulent fluctuations from the flow visualizations, rigorous phase-averaging was performed over ten wake passing periods for both cases. Iso-surfaces similar to those in Figs. 4.13 & 4.14 were generated and are presented in Figs. 4.15 and 4.16. In these images, the endwall flow structures are revealed in more detail. For the 50% reaction stage, as the wake convects through the passage, the passage vortex appears to move ahead of the wake and out of the passage. As for the $Re = 50,000$ simulations, a longitudinal near-wall structure is observed near the pressure side trailing edge. In contrast to the bar wake generator case, small-scale near-wall structures are visible throughout the passage which likely result from crossflow instability [63].

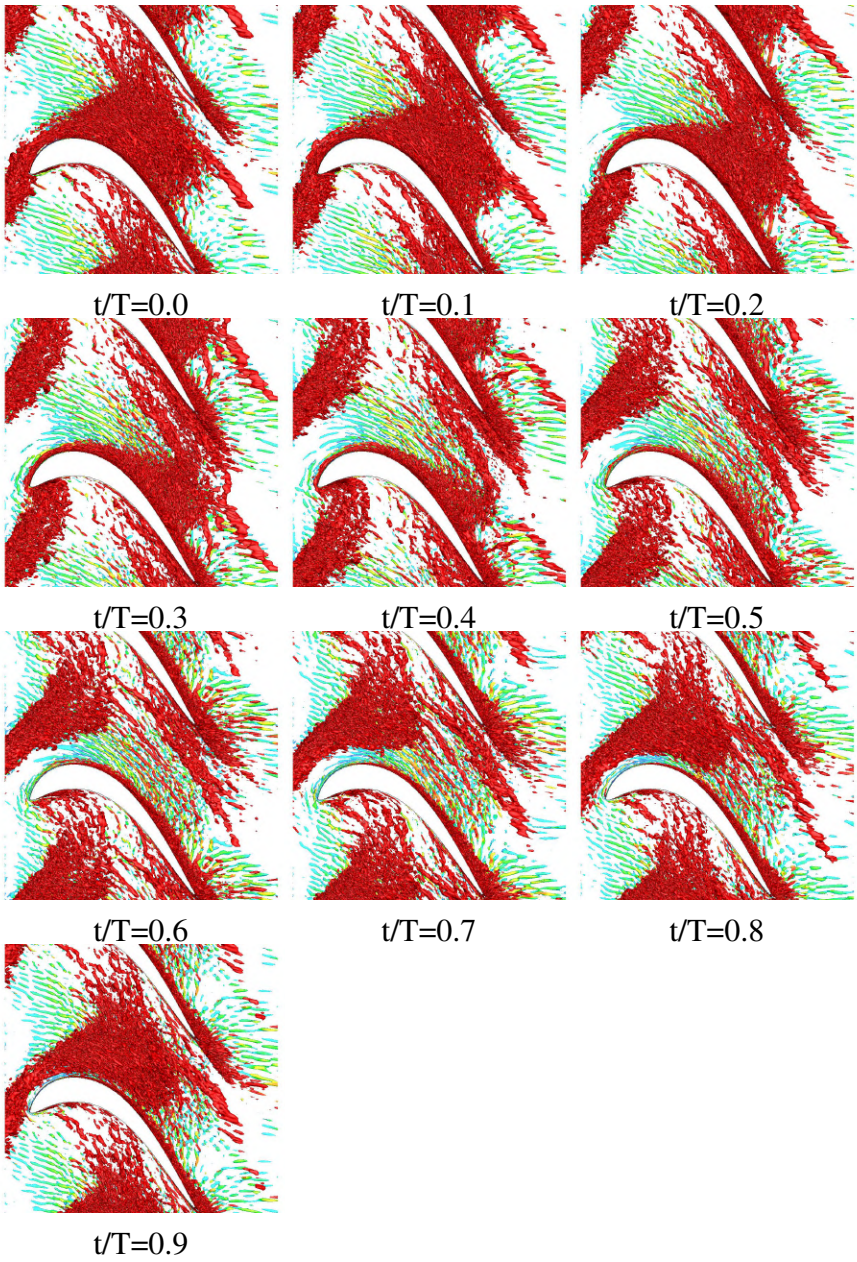

Figure 4.15: Iso-surfaces of $Q = 25$ flooded by wall distance ($z > 0.02$ is red) for 50% reaction stage (phase-averaged flow).

For the barwake generator case, the wake does not appear to cross the PV and does not reach the pressure side of the blade. The region between the PV and the pressure side remains laminar. This "quiescent region" does not feature small-scale near-wall structures. As observed previously, the bar wake generator wake appears to linger over the suction surface until the next wake moves through the passage and replaces it.

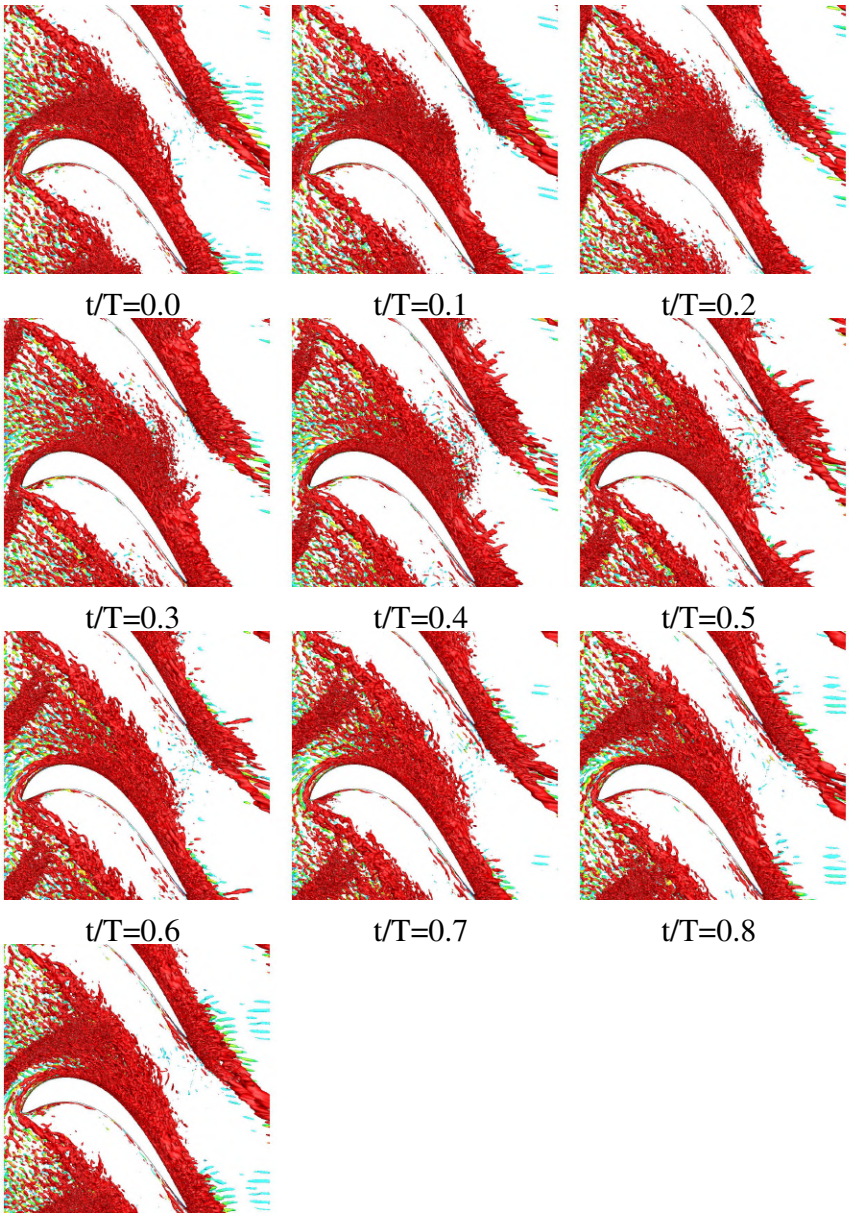

Figure 4.16: Iso-surfaces of $Q = 25$ flooded by wall distance ($z > 0.02$ is red) for 50% reaction stage (phase-averaged flow).

4.6 Proper Orthogonal Decomposition of Phase-Averaged Flow

The proper orthogonal decomposition (POD) [61, 62] was utilized as a filter to remove high-frequency "noise" and thus improve the quality of the phase-averaged data. Towards that end, the phase-averaged flow field was reconstructed from the leading POD modes. The POD was performed for blocks 1, 6, 7, and 8 and the eigenvalues, λ_i, and time coefficients for the 50% reaction stage are plotted in Fig. 4.17. For the time-coefficients, the abscissa was scaled by the period, $T = 1.44$. The eigenvalues are grouped in pairs. The wake passing period is captured by modes 3 and 4. The mode 1 and 2 period is one half of the wake passing period. This implies that the frequency of the dominant modes is two times the wake passing frequency.

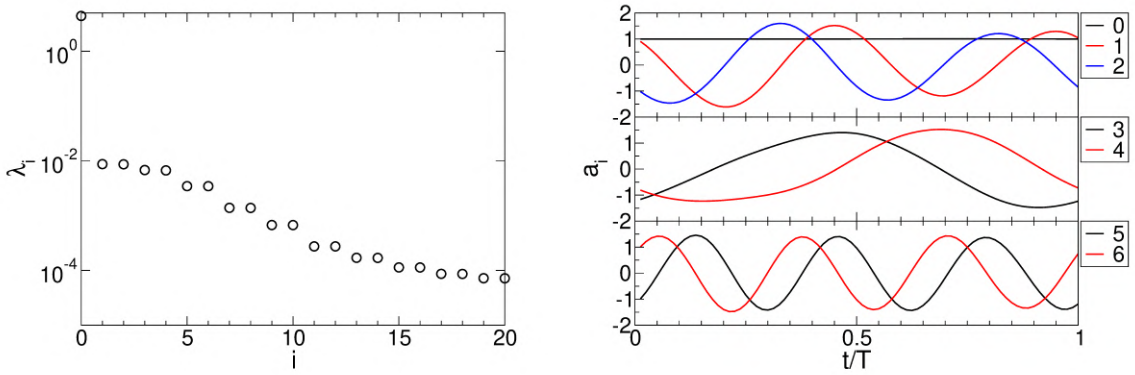

Figure 4.17: POD eigenvalues and time-coefficients for 50% reaction stage.

The flow fields were reconstructed from the leading 5, 10, and 15 modes (Fig. 4.18) and their relative energy is provided in Tab. 4.2. The reconstruction from the leading five modes does not show the passing wakes. For the reconstructions from the first 10 and 15 modes, the wake can be discerned upstream of the rotor. When 15 modes are included in the reconstructions, portions of the wake can be observed inside the passage.

Modes retained	% total energy	% kinetic energy (0 mode omitted)
5	99.77%	76.84%
10	99.94%	93.82%
15	99.96%	96.06%

Table 4.2: Modes retained for reconstruction and their respective cumulative energy content for 50% reaction stage.

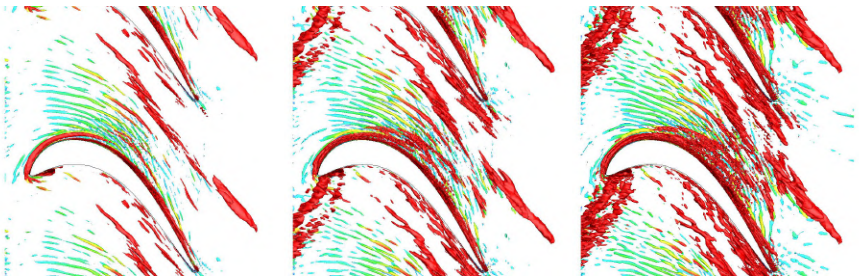

Figure 4.18: Reconstructions from 5, 10, and 15 modes of phase-averaged flow at $t/T = 2/5$ for 50% reaction stage. Iso-surfaces of $Q = 25$ flooded by wall distance ($z > 0.02$ is red).

Reconstructions from 15 modes for the full period are visualized in Fig. 4.19. For $t/T = 0.0$, a weak PV is visible (structure "1" in Fig. 4.19). As the wake enters the passage, the upstream part of the PV is loosing coherence (e.g., $t/T = 0.3$) and the PV moves slightly closer to the pressure surface (e.g., $t/T = 0.5$) and out of the passage (e.g., $t/T = 0.7$). As the structure leaves the passage (now relabeled as structure "2" for $t/T = 0.0$), a new PV forms.

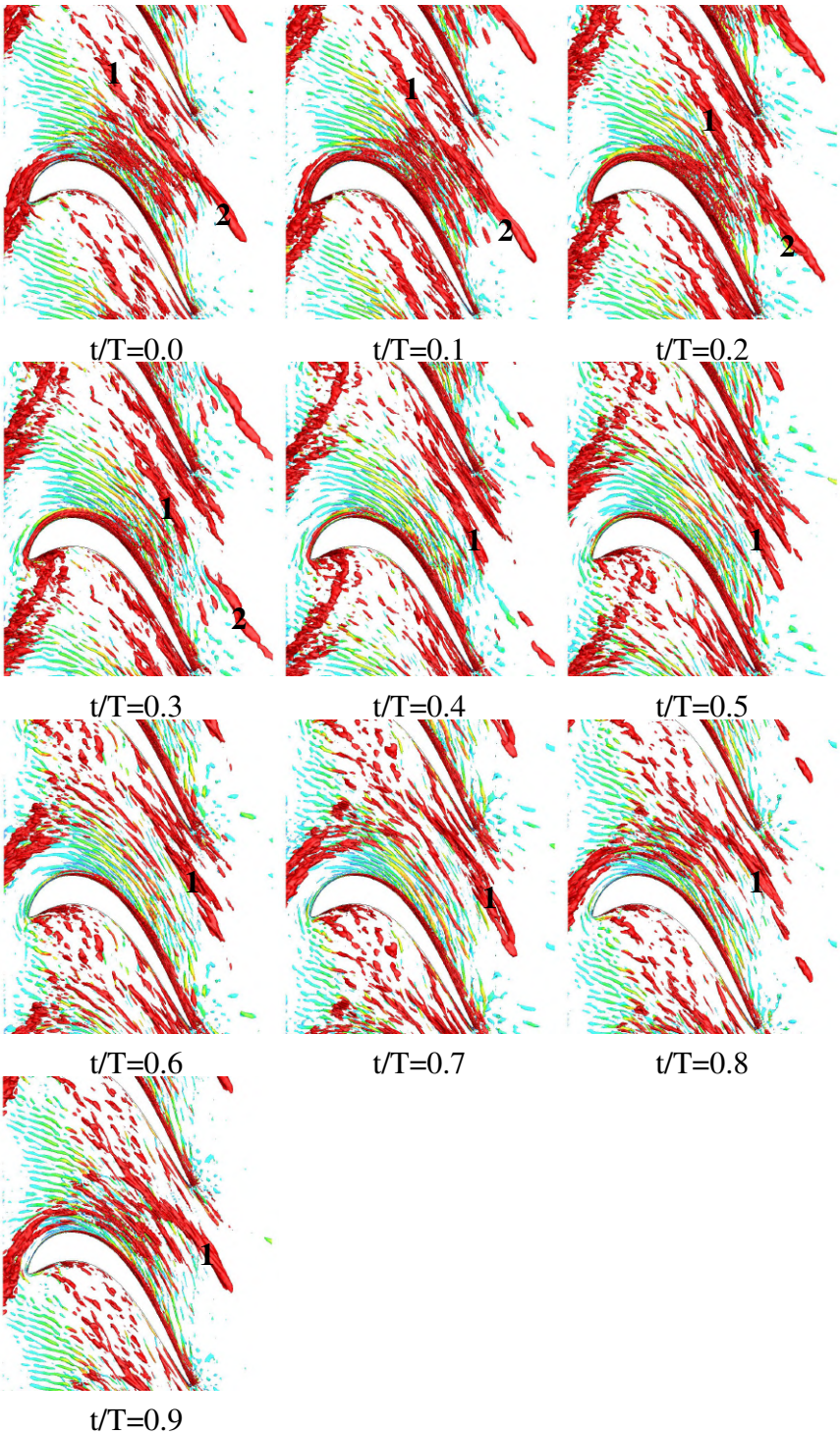

Figure 4.19: Iso-surfaces of $Q = 25$ flooded by wall distance ($z > 0.02$ is red) for 50% reaction stage (phase-averaged flow). POD reconstructions from 15 modes.

The eigenvalues, λ_i, and time coefficients for the barwake generator case are plotted in Fig. 4.20. The spectra for the 50% reaction stage and bar wake generator case are very similar. Different from the 50% reaction stage results, the period of the time-coefficients for modes 1 and 2 matches the wake passing period and the period of modes 3 and 4 is half of the wake passing period.

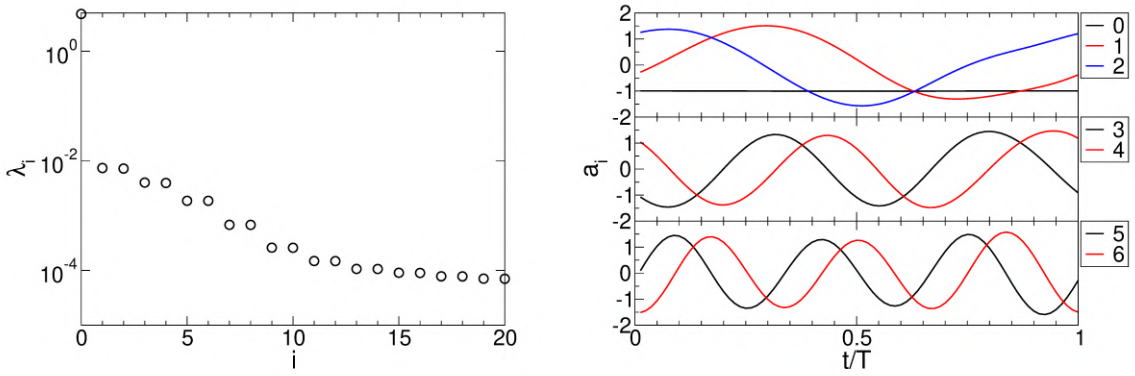

Figure 4.20: POD eigenvalues and time-coefficients for bar wake generator.

For the bar wake generator case, the instantaneous flow fields were also reconstructed from the leading 5, 10, and 15 modes. The relative energies are listed in Tab. 4.3 and flow visualizations for $t/T = 0.2$ are provided in Fig. 4.21. The reconstructions show very little evidence of the passing wakes. This is consistent with the earlier observation that the bar wake generator wake has close to no streamwise vorticity. When more modes are included in the reconstruction, more of the small-scale near-wall structures become visible (blue and green structures just above the suction surface leading edge).

Modes retained	% total energy	% kinetic energy (0 mode omitted)
5	99.87%	79.79%
10	99.95%	91.98%
15	99.96%	93.93%

Table 4.3: Modes retained for reconstruction and their respective cumulative energy content for bar wake generator.

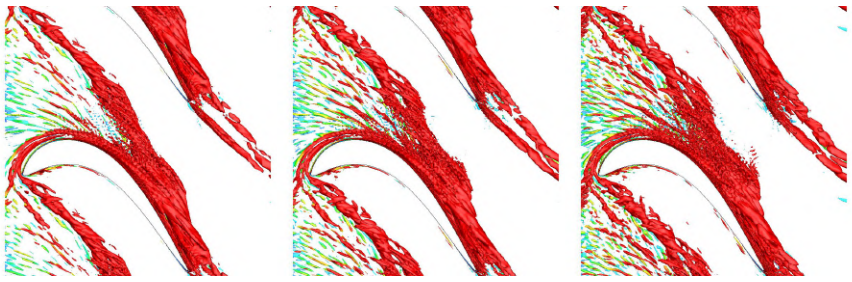

Figure 4.21: Reconstructions from 5, 10, and 15 modes of phase-averaged flow at $t/T = 2/5$ for bar wake generator. Iso-surfaces of $Q = 25$ flooded by wall distance ($z > 0.02$ is red).

In Fig. 4.22, the reconstructed (from 15 modes) flow fields in the rotor passage are visualized in more detail. The passing wakes have no noteworthy effect on the PV or the SV (both are marked for $t/T = 0.5$). In agreement with the Re=50,000 results, the visualizations also provide evidence of an additional weaker vortex just upstream of the PV (structure "3" for $t/T = 0.7$). This secondary vortex is caused by the lift-up of the endwall boundary layer by the PV. As already noted, different from the 50% reaction stage case, for the case with upstream bar wake generator, the suction side corner separation is not suppressed by the unsteady wakes. The vorticity associated with the corner separation extends into the wake (see structure "4" for $t/T = 0.9$ in Fig. 4.22). As the wake passes through the passage, this structure is intermittently suppressed (see void space marked "4" for $t/T = 0.3$ in Fig. 4.22).

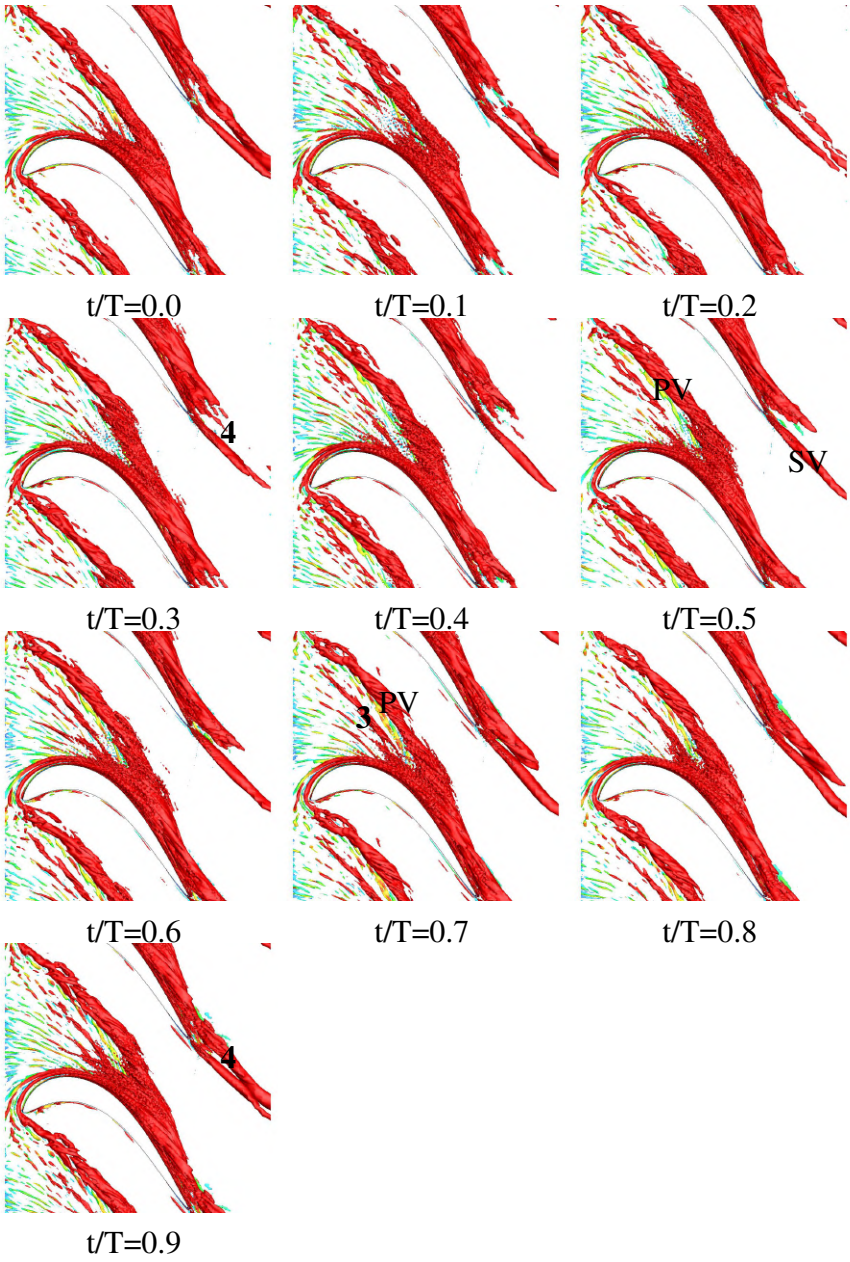

Figure 4.22: Iso-surfaces of $Q = 25$ flooded by wall distance ($z > 0.02$ is red) for barwake generator (phase-averaged flow). POD reconstructions from 15 modes.

5 Conclusions

Large eddy simulations of a 50% reaction stage and a cascade with two different diameter bar wake generators were carried out for Reynolds numbers based on inlet velocity and axial chord length of $50,000$ and $100,000$. For $Re = 50,000$, an approach flow and wake analysis revealed that the boundary layer grows much faster for the bar wake generators than for the 50% reaction stage. This was attributed to the relative motion of the endwall with respect to the core flow. Therefore, for the Re=100,000 simulations, the arrangement was changed and the bar wake generators (and upstream stator vanes) were fixed and the rotor blades were moving. For the 50% reaction stage, at Re=50,000 a large laminar separation from the suction surface of the stator vanes resulted in a wide wake with large momentum deficit. To match the wake width, the bar wake generator diameter had to be increased to a value that is much larger than what is typically used in experiments (i.e., bar wake generator diameter that matches trailing edge diameter). The large wake width also motivated the Re=100,000 simulations. For both Reynolds numbers, the proper orthogonal decomposition was employed as a filter to improve the quality of the phase-averages by removing the small-scale structures.

Visualizations of the filtered phase-averaged flow fields for Re=50,000 revealed that, even for the small cylinder bar wake generator, the wakes lead to a periodic suppression of the suction side laminar separation. The rotor PV is entirely suppressed for the 50% reaction stage and larger bar wake generator. Interestingly, for the 50% reaction stage, the passing wakes cause leading edge laminar separation from the pressure side of the blades. Furthermore, a new longitudinal structure near the trailing edge of the blades was discovered and traced back to near-wall wake vorticity.

For $Re = 100,000$, the laminar separation from the suction surface is much less severe and the stator wake width was matched by a smaller (compared to the $Re = 50,000$ results) diameter cylinder bar wake generator. The stator wake features strong three-dimensional (3-D) vortical components near the endwall while the wakes for the bar wake generator are nearly 2-D. For both cases, the 2-D wake component leads to by-pass transition of the suction-side boundary layer and a suppression of the 2-D laminar separation. After the wake passage, the suction-side boundary layer takes time to relaminarize. For the upstream stator vanes, the 3-D wake component strikes the suction surface first and suppresses the corner separation and passage vortex. The 2-D wake component than impacts the entire span and suppresses the laminar separation. After the wake has passed, the 2-D laminar separation reestablishes itself near the endwall and then spreads out in the spanwise direction. On the other hand, the bar wake generator wakes fully suppress the suction-surface 2-D separation over the entire wake passing period but do not reduce the suction-surface corner separation. Also, the passage vortex remains intact. The full suppression of the laminar separation for the bar generator wakes can be explained by the larger width of the wakes (compared to the stator wakes) which leaves the suction-side boundary layer less time to relaminarize. Also in contrast to the stator vanes, for the bar wake generator the suction-surface corner separation is not affected much. Overall, the present results indicate that bar wake generators are useful for investigating the wake effect on the suction-side laminar separation. Wake generator however fail to

model the wake effect on the endwall flow structures and corner-separation for front-loaded high-lift blades.

6 Students Supported by Grant

- Zachary Robison, Ph.D. in May 2022
- Sergio Romero, Ph.D. in Summer 2020
- Stephen Simko, B.S. in May 2022

7 Publications Resulting from Grant

- Robison, Z., and Gross, A., "Comparative Numerical Investigation of Wake Effect on Low-Pressure Turbine Endwall Flow," under review, AIAA Journal
- Robison, Z., and Gross, A., "Large-Eddy Simulation of Low-Pressure Turbine Cascade with Unsteady Wakes," Aerospace, Vol. 8, No. 6, 2021, 184 https://doi.org/10.3390/aerospace8070184
- Robison, Z.D., and Gross, A., "Numerical Investigation of Effect of Stator and Bar Wake Generator on Low-Pressure Turbine Endwall Flow," AIAA-2022-0597, AIAA Scitech 2022 Forum, 3-7 January 2022, San Diego, CA https://doi.org/10.2514/6.2022-0597
- Robison, Z.D., Simko, S., and Gross, A., "Numerical Investigation of 50% Reaction Low-Pressure Turbine Stage," AIAA 2021-2764, AIAA AVIATION 2021 FORUM, August 2021 https://doi.org/10.2514/6.2021-2764
- Robison, Z.D., Gross, A., "Numerical Investigation of Low-Pressure Turbine Cascade with Unsteady Wakes," AIAA-2021-1668, AIAA SciTech 2021 Forum, 11-15 & 19-21 January 2021, Virtual Event https://doi.org/10.2514/6.2021-1668
- Romero Martinez, S.R., and Gross, A., "Numerical Investigation of Low-Pressure Turbine Stage with Unsteady Wakes," AIAA-2020-0836, AIAA Scitech 2020 Forum, 6-10 January 2020, Orlando, FL https://doi.org/10.2514/6.2020-0836

Bibliography

[1] M. McQuilling, *Design and Validation of a High Lift Low-Pressure Turbine Blade*. PhD thesis, Wright State University, 2007.

[2] T. Praisner, E. Grover, D. Knezevici, I. Popovic, S. Sjolander, J. Clark, and R. Sondergaard, "Toward the expansion of low-pressure-turbine airfoil design space," *Journal of Turbomachinery*, vol. 135, no. 6, p. 061007, 2013.

[3] C. R. Marks, R. Sondergaard, P. S. Bear, and M. Wolff, "Reynolds number effects on the secondary flow of profile contoured low pressure turbines," in *54th AIAA aerospace sciences meeting*, p. 0114, 2016.

[4] M. Eric Lyall, P. I. King, R. Sondergaard, J. P. Clark, and M. W. McQuilling, "An investigation of reynolds lapse rate for highly loaded low pressure turbine airfoils with forward and aft loading," *Journal of Turbomachinery*, vol. 134, no. 5, p. 051028, 2012.

[5] A. Weiss and L. Fottner, "The influence of load distribution on secondary flow in straight turbine cascades," *Journal of Turbomachinery*, vol. 117, no. 1, pp. 133–141, 1995.

[6] T. Zoric, I. Popovic, S. Sjolander, T. Praisner, and E. Grover, "Comparative investigation of three highly loaded lp turbine airfoils: Part i - measured profile and secondary losses at design incidence," in *Turbo Expo: Power for Land, Sea, and Air*, vol. 47950, pp. 621–630, 2007.

[7] M. Eric Lyall, P. I. King, J. P. Clark, and R. Sondergaard, "Endwall loss reduction of high lift low pressure turbine airfoils using profile contouring - part i: Airfoil design," *Journal of Turbomachinery*, vol. 136, no. 8, p. 081005, 2014.

[8] P. S. Bear, M. Wolff, A. Gross, C. Marks, and R. Sondergaard, "Secondary loss production mechanisms in a low pressure turbine cascade," in *52nd AIAA/SAE/ASEE Joint Propulsion Conference*, p. 4554, 2016.

[9] P. Bear, M. Wolff, A. Gross, C. R. Marks, and R. Sondergaard, "Experimental investigation of total pressure loss development in a highly loaded low-pressure turbine cascade," *Journal of Turbomachinery*, vol. 140, no. 3, p. 031003, 2018.

[10] W. J. Devenport and R. L. Simpson, "Time-depeiident and time-averaged turbulence structure near the nose of a wing-body junction," *Journal of Fluid Mechanics*, vol. 210, pp. 23–55, 1990.

[11] H.-P. Wang, S. J. Olson, R. J. Goldstein, and E. R. Eckert, "Flow visualization in a linear turbine cascade of high performance turbine blades," *Journal of Turbomachinery*, vol. 119, no. 1, pp. 1–8, 1997.

[12] Z. Robison, J.-P. Mosele, and A. Gross, "Numerical investigation of turbulent junction flow horseshoe vortex dynamics," *AIAA Journal*, vol. 59, no. 4, pp. 1238–1253, 2021.

[13] E. Veley, C. Marks, R. Anthony, R. Sondergaard, N. Fletcher, and M. Wolff, "Unsteady flow measurements in a low pressure turbine passage using surface mounted thin film sensors," in *53rd AIAA/SAE/ASEE Joint Propulsion Conference*, p. 4825, 2017.

[14] E. Veley, C. Marks, R. Anthony, R. Sondergaard, and M. Wolff, "Unsteady flow measurements in a front loaded low pressure turbine passage," in *2018 AIAA Aerospace Sciences Meeting*, p. 2124, 2018.

[15] N. Fletcher, C. Marks, R. Petrie, R. Sondergaard, and M. Wolff, "Experimental investigation of endwall flow control for front loaded turbine blades," in *2018 Joint Propulsion Conference*, p. 4436, 2018.

[16] A. Gross, C. R. Marks, and R. Sondergaard, "Numerical investigation of low-pressure turbine junction flow," *AIAA Journal*, vol. 55, no. 10, pp. 3617–3621, 2017.

[17] A. Gross, C. R. Marks, R. Sondergaard, P. S. Bear, and J. Mitch Wolff, "Experimental and numerical characterization of flow through highly loaded low-pressure turbine cascade," *Journal of Propulsion and Power*, vol. 34, no. 1, pp. 27–39, 2018.

[18] L. Langston, M. Nice, and R. Hooper, "Three-dimensional flow within a turbine cascade passage," *Journal of Engineering for Gas Turbines and Power*, vol. 99, no. 1, pp. 21–28, 1977.

[19] L. Langston, "Secondary flows in axial turbines - a review," *Annals of the New York Academy of Sciences*, vol. 934, no. 1, pp. 11–26, 2001.

[20] C. Sieverding, "Recent progress in the understanding of basic aspects of secondary flows in turbine blade passages," *Journal of Engineering for Gas Turbines and Power*, vol. 107, no. 2, pp. 248–257, 1985.

[21] R. Goldstein and R. Spores, "Turbulent transport on the endwall in the region between adjacent turbine blades," *Journal of Heat Transfer*, vol. 110, no. 4a, pp. 862–869, 1988.

[22] O. Sharma and T. Butler, "Predictions of endwall losses and secondary flows in axial flow turbine cascades," *Journal of Turbomachinery*, vol. 109, no. 2, pp. 229–236, 1987.

[23] S. Kang and C. Hirsch, "Three dimensional flow in a linear compressor cascade at design conditions," in *Turbo Expo: Power for Land, Sea, and Air*, vol. 78989, p. V001T01A047, American Society of Mechanical Engineers, 1991.

[24] H. Hodson and R. Dominy, "The off-design performance of a low-pressure turbine cascade," *Journal of Turbomachinery*, vol. 109, no. 2, pp. 201–209, 1987.

[25] J. Schmitz, E. Perez, S. Morris, T. Corke, J. Clark, P. Koch, and S. Puterbaugh, "Highly loaded low-pressure turbine: Design, numerical, and experimental analysis," *Journal of Propulsion and Power*, vol. 32, no. 1, pp. 142–152, 2016.

[26] V. Schulte and H. Hodson, "Unsteady wake-induced boundary layer transition in high lift lp turbines," *Journal of Turbomachinery*, vol. 120, no. 1, pp. 28–35, 1998.

[27] R. W. Kaszeta, T. W. Simon, and D. E. Ashpis, "Experimental investigation of transition to turbulence as affected by passing wakes," in *Turbo Expo: Power for Land, Sea, and Air*, vol. 78521, p. V003T01A069, American Society of Mechanical Engineers, 2001.

[28] R. Stieger and H. Hodson, "The transition mechanism of highly loaded low-pressure turbine blades," *Journal of Turbomachinery*, vol. 126, no. 4, pp. 536–543, 2004.

[29] R. Stieger and H. Hodson, "The unsteady development of a turbulent wake through a downstream low-pressure turbine blade passage," *Journal of Turbomachinery*, vol. 127, no. 2, pp. 388–394, 2005.

[30] C. Nessler, C. Marks, R. Sondergaard, and M. Wolff, "Piv investigation of periodic unsteady wakes over a highly loaded lpt blade," in *45th AIAA/ASME/SAE/ASEE Joint Propulsion Conference & Exhibit*, p. 5107, 2009.

[31] C. Nessler, C. Marks, R. Sondergaard, and M. Wolff, "Investigation of losses on a highly loaded low pressure turbine blade with unsteady wakes," in *47th AIAA Aerospace Sciences Meeting including The New Horizons Forum and Aerospace Exposition*, p. 302, 2009.

[32] C. Nessler, "Characterization of internal wake generator at low reynolds number with a linear cascade of low pressure turbine blades," Master's thesis, Wright State University, 2010.

[33] X. Wu and P. A. Durbin, "Evidence of longitudinal vortices evolved from distorted wakes in a turbine passage," *Journal of Fluid Mechanics*, vol. 446, pp. 199–228, 2001.

[34] V. Michelassi, J. Wissink, and W. Rodi, "Analysis of dns and les of flow in a low pressure turbine cascade with incoming wakes and comparison with experiments," *Flow, turbulence and combustion*, vol. 69, no. 3, pp. 295–329, 2002.

[35] V. Michelassi, J. Wissink, J. Frohlich, and W. Rodi, "Large-eddy simulation of flow around low-pressure turbine blade with incoming wakes," *AIAA journal*, vol. 41, no. 11, pp. 2143–2156, 2003.

[36] R. Volino, "Effect of unsteady wakes on boundary layer separation on a very high lift low pressure turbine airfoil," *Journal of Turbomachinery*, vol. 134, no. 1, p. 011011, 2012.

[37] R. Ciorciari, I. Kirik, and R. Niehuis, "Effects of unsteady wakes on the secondary flows in the linear t106 turbine cascade," *Journal of Turbomachinery*, vol. 136, no. 9, p. 091010, 2014.

[38] K. Gompertz, J. Pluim, and J. Bons, "Separation control authority of vortex generating jets in a low-pressure turbine with simulated wakes," in *47th AIAA Aerospace Sciences Meeting including The New Horizons Forum and Aerospace Exposition*, p. 377, 2009.

[39] J. Cui, V. Nagabhushana Rao, and P. Tucker, "Numerical investigation of contrasting flow physics in different zones of a high-lift low-pressure turbine blade," *Journal of Turbomachinery*, vol. 138, no. 1, p. 011003, 2016.

[40] V. N. Rao, P. Tucker, R. Jefferson-Loveday, and J. Coull, "Large eddy simulations in low-pressure turbines: Effect of wakes at elevated free-stream turbulence," *International journal of heat and fluid flow*, vol. 43, pp. 85–95, 2013.

[41] M. Sinkwitz, B. Winhart, D. Engelmann, F. Di Mare, and R. Mailach, "Experimental and numerical investigation of secondary flow structures in an annular low pressure turbine cascade under periodic wake impact - part 1: Experimental results," *Journal of Turbomachinery*, vol. 141, no. 2, 2019.

[42] J. Cui, V. N. Rao, and P. G. Tucker, "Numerical investigation of secondary flows in a high-lift low pressure turbine," *International Journal of Heat and Fluid Flow*, vol. 63, pp. 149–157, 2017.

[43] N. Fletcher, C. R. Marks, R. Sondergaard, and M. Wolff, "Characterization of periodic unsteadiness generator for secondary flow studies," in *AIAA Scitech 2019 Forum*, p. 0622, 2019.

[44] N. Fletcher, M. Wolff, and C. R. Marks, "Turbine secondary flow response to upstream periodic unsteadiness," in *AIAA Scitech 2020 Forum*, p. 0834, 2020.

[45] Z. D. Robison, A. Gross, N. Fletcher, C. Marks, and R. Sondergaard, "Numerical investigation of linear low-pressure turbine cascade with periodic unsteadiness generating device," in *AIAA AVIATION 2020 FORUM*, p. 2984, 2020.

[46] A. Gross and H. F. Fasel, "High-order accurate numerical method for complex flows," *AIAA journal*, vol. 46, no. 1, pp. 204–214, 2008.

[47] A. Gross and H. F. Fasel, "Multi-block poisson grid generator for cascade simulations," *Mathematics and Computers in Simulation*, vol. 79, no. 3, pp. 416–428, 2008.

[48] F. Nicoud and F. Ducros, "Subgrid-scale stress modelling based on the square of the velocity gradient tensor," *Flow, turbulence and Combustion*, vol. 62, no. 3, pp. 183–200, 1999.

[49] A. Gross, C. R. Marks, R. Sondergaard, P. S. Bear, and J. Mitch Wolff, "Experimental and numerical characterization of flow through highly loaded low-pressure turbine cascade," *Journal of Propulsion and Power*, vol. 34, no. 1, pp. 27–39, 2018.

[50] B. Raverdy, I. Mary, P. Sagaut, and N. Liamis, "Large-eddy simulation of the flow around a low pressure turbine blade," in *Direct and Large-Eddy Simulation IV*, pp. 381–388, Springer, 2001.

[51] A. Gross and H. Fasel, "Characteristic ghost cell boundary condition," *AIAA journal*, vol. 45, no. 1, pp. 302–306, 2007.

[52] S. R. Romero Martinez and A. Gross, "Numerical investigation of strategies aimed at reduction of low-pressure turbine endwall losses," in *AIAA Scitech 2019 Forum*, p. 1656, 2019.

[53] N. Jarrin, S. Benhamadouche, D. Laurence, and R. Prosser, "A synthetic-eddy-method for generating inflow conditions for large-eddy simulations," *International Journal of Heat and Fluid Flow*, vol. 27, no. 4, pp. 585–593, 2006.

[54] R. Poletto, T. Craft, and A. Revell, "A new divergence free synthetic eddy method for the reproduction of inlet flow conditions for les," *Flow, turbulence and combustion*, vol. 91, no. 3, pp. 519–539, 2013.

[55] M. R. Mankbadi, M. A. Vyas, J. R. DeBonis, and N. J. Georgiadis, "Evaluation of inflow turbulence methods in large-eddy simulations of a supersonic boundary layer," in *2018 Fluid Dynamics Conference*, p. 3404, 2018.

[56] M. Klein, A. Sadiki, and J. Janicka, "A digital filter based generation of inflow data for spatially developing direct numerical or large eddy simulations," *Journal of computational Physics*, vol. 186, no. 2, pp. 652–665, 2003.

[57] J. C. Hunt, A. A. Wray, and P. Moin, "Eddies, streams, and convergence zones in turbulent flows," *Studying Turbulence Using Numerical Simulation Databases, 2. Proceedings of the 1988 Summer Program*, 1988.

[58] L. Purtell, P. Klebanoff, and F. Buckley, "Turbulent boundary layer at low reynolds number," *The Physics of Fluids*, vol. 24, no. 5, pp. 802–811, 1981.

[59] S. R. Romero Martinez and A. Gross, "Numerical investigation of low-pressure turbine stage with unsteady wakes," in *AIAA Scitech 2020 Forum*, p. 0836, 2020.

[60] R. Howell, H. Hodson, V. Schulte, R. Stieger, H.-P. Schiffer, F. Haselbach, and N. Harvey, "Boundary layer development in the br710 and br715 lp turbines - the implementation of high-lift and ultra-high-lift concepts," *J. Turbomach.*, vol. 124, no. 3, pp. 385–392, 2002.

[61] J. L. Lumley, "The structure of inhomogeneous turbulent flows," *Atmospheric turbulence and radio wave propagation*, pp. 166–178, 1967.

[62] L. Sirovich, "Turbulence and the dynamics of coherent structures, parts i, ii and iii," *Quart. Appl. Math.*, pp. 561–590, 1987.

[63] A. Gross, C. R. Marks, and R. Sondergaard, "Local spatial linear stability analysis of low-pressure turbine endwall boundary layer," *AIAA Journal*, vol. 56, no. 6, pp. 2166–2177, 2018.

REPORT DOCUMENTATION PAGE

Form Approved
OMB No. 0704-0188

1. REPORT DATE *(DD-MM-YY)*	2. REPORT TYPE	3. DATES COVERED *(From - To)*
07-04-22	Final	02-01-19 – 07-31-22

4. TITLE AND SUBTITLE
(HBCU) Numerical Investigation of Wake Effect for High-Lift Low-Pressure Turbine Blades

5a. CONTRACT NUMBER

5b. GRANT NUMBER
FA9550-19-1-0080

5c. PROGRAM ELEMENT NUMBER

6. AUTHOR(S)
Andreas Gross

5d. PROJECT NUMBER

5e. TASK NUMBER

5f. WORK UNIT NUMBER

7. PERFORMING ORGANIZATION NAME(S) AND ADDRESS(ES)
Mechanical and Aerospace Engineering Department
New Mexico State University
PO Box 30001/MSC 3450
1040 S Horseshoe St
Las Cruces, NM 88003

8. PERFORMING ORGANIZATION REPORT NUMBER

9. SPONSORING/MONITORING AGENCY NAME(S) AND ADDRESS(ES)
Air Force Office of Scientific Research
875 N. Randolph St, Ste 325 Rm 3112
Arlington, VA 22203

10. SPONSORING/MONITORING AGENCY ACRONYM(S)
AFOSR

11. SPONSORING/MONITORING AGENCY REPORT NUMBER(S)

12. DISTRIBUTION/AVAILABILITY STATEMENT
DISTRIBUTION STATEMENT A. Approved for public release: distribution unlimited

13. SUPPLEMENTARY NOTES

14. ABSTRACT
In low-pressure turbine linear cascade experiments, upstream stator vanes are often modeled by moving bar wake generators. The wake effect of a stator and a bar wake generator on the flow through a rotor with front-loaded high-lift blades were investigated and compared. Implicit large-eddy simulations were performed of the flow through a full turbine cascade with L2F airfoils (for both the stator vanes and rotor blades) as well as of the flow through a linear cascade with L2F blades and moving bar wake generator. The chord-based Reynolds number for the simulations was 50,000 and 100,000. The L2F generates pronounced endwall structures that clearly differentiate the resulting wake flow from that obtained with the bar-wake generator. Instantaneous flow visualizations reveal a periodic suppression of the rotor blade suction-side separation for both cases. For the bar wake generator, the wakes are wider and the wake effect is spread out over a larger portion of the wake shedding period. With upstream stator vanes, the rotor blade passage vortex and suction-side corner separation are suppressed. This suggests that for front-loaded high-lift airfoils, bar wake generators can accurately model the effect of the two-dimensional wake component. The stator near-wall structures appear to be chiefly responsible for the suppression of the passage vortex and corner separation. This effect is not captured by the bar wake generator.

15. SUBJECT TERMS
Low-Pressure Turbine Passage; Large-eddy simulations; Wake Effect; Endwall Flow

16. SECURITY CLASSIFICATION OF:			17. LIMITATION OF ABSTRACT:	18. NUMBER OF PAGES	19a. NAME OF RESPONSIBLE PERSON (Monitor)
a. REPORT	b. ABSTRACT	c. THIS PAGE			Gregg Abate
Unclassified	Unclassified	Unclassified	Unclassified Unlimited	71	19b. TELEPHONE NUMBER (Include Area Code) (703) 835-4314